To the Graduate Council:

I am submitting herewith a dissertation written by Daniel Larry Maxwell entitled "A Molecular Dynamics Simulation of the Effect of Shear on Molecular Orientation". I have examined the final copy of this dissertation for form and content and recommend that it be accepted in partial fulfillment of the requirements for the degree of Doctor of Philosophy, with a major in Mechanical Engineering.

Basil N. Antar, Major Professor

We have read this dissertation
and recommend its acceptance:

Accepted for the Council:

Associate Vice Chancellor and
Dean of the Graduate School

A MOLECULAR DYNAMICS SIMULATION OF THE EFFECT OF SHEAR ON MOLECULAR ORIENTATION

A Dissertation
Presented for the
Doctor of Philosophy
Degree
The University of Tennessee, Knoxville

Daniel Larry Maxwell
December 2000

for My Family

ACKNOWLEDGMENTS

I am very grateful to my advisor, Dr. Basil Antar for his instruction and example. Without him this work would never have been accomplished. Dr. Al Pujol, representing the Tennessee Space Grant Consortium was invaluable in providing financial support for this project. I thank Dr. Frank Collins, Dr. Gary Flandro, Dr. Bruce Whitehead, and Dr. Al Pujol for their advice and assistance as members of my review committee. Dr. Mark Paley at NASA-Marshall Space Flight Center was very helpful in providing experimental results and in gaining access to the SGI Origin at NASA-MSFC. My thanks extend to all the staff and faculty at UTSI who have played an instrumental part in making my academic experience a successful one. Indeed, there have been many teachers throughout my life to whom I am indebted for helping me to achieve my goals. I express thanks to my friends and colleagues at UTSI for their support and insight, especially Clark Wiberg, Tom Holecek, Adel Omrani, and Sheri Hlady.

I extend my deepest gratitude to my loving wife Holly who helped me to make sure that I understood what I was saying and who was always there with a hug and a smile.

Finally, I acknowledge the assistance of my Father in Heaven who has blessed me with the talents and abilities to discover and understand his wondrous creations.

ABSTRACT

The focus of this work is the investigation of the effect of shear produced by buoyancy-induced convection on the orientation of rod-like molecules. The problem is a mathematical simulation of a physical problem dealing with the growth of a polymer film which is under examination for use in fiber optic communication. The Molecular Dynamics simulation method was employed to solve the problem. A computer program was developed to implement the simulation and the details of the simulation development are discussed. The results of the atomic simulations that were used to validate the code are presented first. The simulation results for molecules and mixtures of molecules and atoms are then presented. It was determined that the shear caused by the velocity field does have an effect on the orientation of the rod-like molecules. However, the magnitude of this effect was seen to be sensitive to the type of the molecule, the concentration of the solution, and the properties of the wall.

TABLE OF CONTENTS

CHAPTER		PAGE
1.	INTRODUCTION	1
	Motivation	1
	Hypothesis	4
	Approach	6
2.	PHYSICAL CONFIGURATION AND MATHEMATICAL MODEL	8
	Physical Configuration	8
	Assumptions	10
	Mathematical Model	12
	Non-Dimensionalization	17
3.	PREVIOUS WORK	20
	Molecular Dynamics	20
	Channel Flows	22
	Orientation Effects	27
	New Ground	27
4.	IMPLEMENTATION - SPHERICAL ATOMS	29
	Phase Space	29
	Particle Interaction	32
	Potential Truncation	38
	Neighbor List and Cells	41
	Integration	46
	Boundary Conditions	50
	Initial Conditions and Equilibration	57
	Thermodynamic Properties	60
	Channel Flow	64
5.	IMPLEMENTATION - MOLECULES	69
	Structure	69
	Force and Moment Calculation	71
	Rotation	73
	Channel Flow	79
6.	RESULTS AND DISCUSSION	82
	Validation	82
	Channel Flow	84
	Molecules	100

Monomer Solution 117

7. CONCLUSIONS AND FUTURE WORK 132

REFERENCES 134

VITA 142

LIST OF FIGURES

FIGURE PAGE

1. Schematic representation of the Diacetylene monomer (DAMNA) 2
2. Schematic of PDAMNA film growth 5
3. Representation of the physical configuration 9
4. Mathematical model 13
5. Schematic of the interaction between two atoms 15
6. Velocity dependence on wall density and strength 23
7. Density profile for a narrow pore 25
8. Velocity profile of a plane Poiseuille flow 26
9. Idealized pair potentials 34
10. The Lennard-Jones(12-6) potential 36
11. Comparison of Argon pair potentials 37
12. The Truncated Lennard-Jones (12-6) potential 39
13. Schematic representation of the Neighbor List 43
14. Division of the simulation volume into cells 45
15. Two-dimensional periodic boundary conditions 52
16. Various types of walls used in MD simulations 54
17. A schematic representation of a face-centered cubic crystal cell 56
18. Schematic representation of plane Poiseuille flow 65
19. Schematic representation of plane Couette flow 66
20. Schematic representation of the interaction between two molecules 72
21. Definition of θ 81
22. Density profile for the no flow case 85
23. Velocity profile for the no flow case 86

24. Analytic plane Couette velocity profile 88
25. Analytic plane Poiseuille velocity profile 89
26. Density profile for the 500 particle plane Couette flow 90
27. Velocity profile for the 500 particle plane Couette flow 91
28. Density profile for the 2000 particle plane Couette flow 92
29. Velocity profile for the 2000 particle plane Couette flow 93
30. Density profile for the 1000 particle
plane Couette flow with stationary bottom wall 94
31. Velocity profile for the 1000 particle
plane Couette flow with stationary bottom wall 95
32. High resolution density profile for the 2000 particle
plane Couette flow 96
33. High resolution velocity profile for the 2000 particle
plane Couette flow 97
34. Density profile for the 2000 particle plane Poiseuille flow 98
35. Velocity profile for the 2000 particle plane Poiseuille flow 99
36. Density profile for the 2000 molecule no flow case 102
37. Velocity profile for the 2000 molecule no flow case 103
38. Angular distribution for the 2000 molecule no flow case 104
39. Density profile for the 2000 molecule plane Couette flow 105
40. Velocity profile for the 2000 molecule plane Couette flow 106
41. Angular distribution for the 2000 molecule plane Couette flow 107
42. Density profile for the 2000 molecule plane Poiseuille flow 108
43. Velocity profile for the 2000 molecule plane Poiseuille flow 109
44. Angular distribution for the 2000 molecule plane Poiseuille flow 110

45. Velocity profile for the 2000 molecule
plane Couette flow with wall density 10 111
46. Angular distribution for the 2000 molecule
plane Couette flow with wall density 10 112
47. Velocity profile for the 2000 molecule
plane Couette flow with wall density 8 113
48. Angular distribution for the 2000 molecule
plane Couette flow with wall density 8 114
49. Velocity profile for the 2000 molecule
plane Couette flow with wall density 6 115
50. Angular distribution for the 2000 molecule
plane Couette flow with wall density 6 116
51. Density profile for the 1:1 monomer solution in plane Couette flow 118
52. Velocity profile for the 1:1 monomer solution in plane Couette flow 119
53. Angular distribution for the 1:1 monomer solution
in plane Couette flow 120
54. Density profile for the 1:4 monomer solution in plane Couette flow 121
55. Velocity profile for the 1:4 monomer solution in plane Couette flow 122
56. Angular distribution for the 1:4 monomer solution
in plane Couette flow 123
57. Density profile for the 4:1 monomer solution in plane Couette flow 124
58. Velocity profile for the 4:1 monomer solution in plane Couette flow 125
59. Angular distribution for the 4:1 monomer solution
in plane Couette flow 126
60. High resolution angular distribution for the 1:4 monomer solution
in plane Couette flow 127

61. Density profile for the 1:4 monomer solution in plane Poiseuille flow....129

62. Velocity profile for the 1:4 monomer solution in plane Poiseuille flow ... 130

63. Angular distribution for the 1:4 monomer solution
in plane Poiseuille flow.....131

CHAPTER 1: INTRODUCTION

MOTIVATION

Fiber optics have become an important part of modern society. Using light as a carrier allows much faster transport of information than electronic transmission. Signal switching is currently accomplished by converting the light signals to electronic signals, performing the necessary operations, and then converting back to light. This creates a bottleneck that limits the speed and efficiency of information transmission. If the switching were performed optically as well, this bottleneck would be eliminated and faster transmission rates would be possible.

One The pursuit of faster transmission rates thus leads through the elimination of this bottleneck by performing the switching optically.

Optical switching requires materials with very specific and unusual properties [1]. Rather than simply allowing the light to pass through at high efficiencies these materials must allow the carrier light waves to be acted upon by virtue of their non-linear optical properties. The non-linear optical (NLO) materials need to work for a variety of wavelengths without reducing the efficiency of transmission which makes fiber optics so desirable.

The search for materials with the desired NLO properties has led researchers to investigate various organic molecules. Poly-diacetylenes (PDAs) in particular possess a structure which favors the sought after behavior. A specific PDA, 2-methyl 4-nitroaniline (PDAMNA) is receiving significant attention by Mark Paley at NASA Marshall Space Flight Center (MSFC) [1,2]. A schematic of the PDAMNA structure is shown in Figure 1. PDAMNA exhibits an encouraging balance of the required properties. The obstacle now being confronted is the difficulty in producing the material.

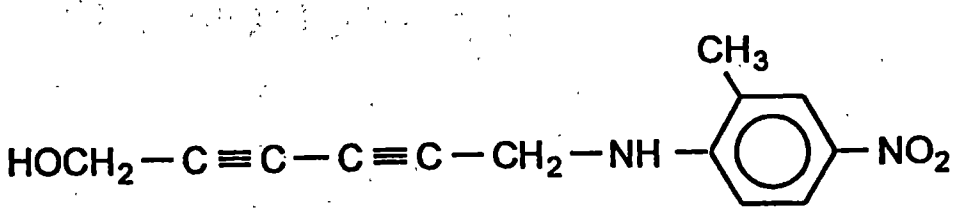

Figure 1. Schematic representation of the Diacetylene monomer (DAMNA). Source: Frazier, D. O., Penn, B. G., Smith, D. D., Witherow, W. K., Paley, M. S., and Abdeldayem, H. A., "Microgravity Processing and Photonic Application of Organic and Polymeric Materials", *Photonic Polymer Systems: Fundamentals, Methods and Applications*, Marcel-Dekker Inc., New York, New York (1997) 693-735.

The NLO materials are generally produced in the form of a film by a specific type of deposition process. PDAMNA films at MSFC are grown by a process of photo-deposition. The solution is irradiated by ultra-violet (UV) light through a quartz or glass window. The film then grows on this quartz or glass substrate. Various masking techniques can also be applied to generate the desired shapes in the film.

The properties of these NLO materials, and of PDAMNA in particular, are heavily dependent on the quality of the material. An important factor in the quality of the film is the inclusion of defects such as polymer aggregates, which are large accumulations of polymers with orientations incompatible with the basic film orientation. Terrestrial film growth has been hampered by the inclusion of too many defects. Low gravity film growth has produced some high quality films, but it is very expensive to grow all the films in microgravity. A better solution would be to find out exactly why gravity promotes defects and find a way to circumvent the problem in terrestrial laboratories.

Buoyancy-induced convection, a significant concern in protein crystal growth, is also a prime suspect as a driver of defects. Most fluids, and the PDAMNA solution is no exception, exhibit a decrease in density as the temperature rises. In the terrestrial environment, gravity then causes the less dense fluid, the warmer fluid, to rise while cooler fluid takes its place. Clearly if the source of heat is at the bottom of a fluid container the configuration is thermally unstable and circular motion develops in the fluid. This is known as a convection cell.

In order to inhibit the development of the convection cell, current PDAMNA film growth experiments involve the application of the UV irradiation from the top of the container as shown in Figure 2. The container used in the experiments is a tall slender rectangular prism, 1 cm$\times$ 1 cm$\times$ 4 cm. Heat is generated when a small

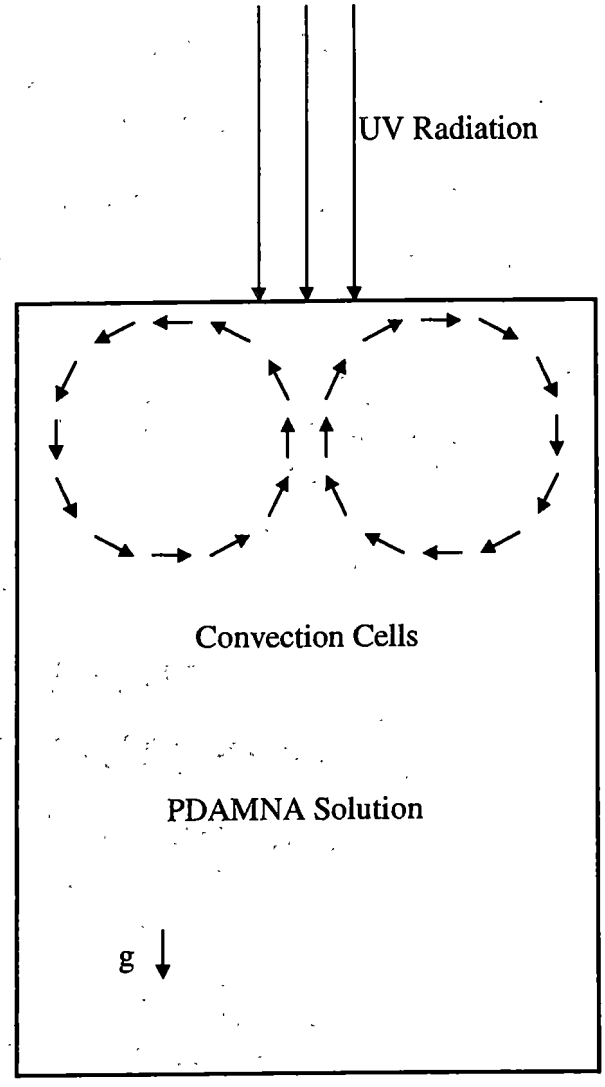

Figure 2. Schematic of PDAMNA film growth.

region of solution adjacent to the top wall absorbs the energy of the UV beam. Experimental observation and numerical simulation both reveal that convection cells, though smaller in magnitude, still arise. This is due to the fact that the warm fluid near the perimeter of the beam is cooled by contact with the container. This fluid descends to be replaced by warmer fluid. In the low gravity environment the buoyancy-induced convection, though still present, is dominated by surface tension forces and convection cells are suppressed.

HYPOTHESIS

Although it seems clear that convection caused by gravity-induced buoyancy is the cause of the difference in quality between NLO materials grown on Earth and those grown in orbit, the relation between the convection and the formation of defects is still uncertain. The next step in the analysis is to examine the situation at a smaller scale, a scale which allows consideration of the film as it grows molecule by molecule. At such a scale the presence of the convection cell is evidenced only by a given bulk velocity of the fluid near the wall.

It is the effect of this bulk velocity that is under investigation in the present work. Since the velocity of the fluid is zero at the wall, there must be a velocity gradient in the fluid near the wall. The hypothesis under consideration is that the shear resulting from this velocity gradient affects the orientation of the PDAMNA monomers on a molecular scale, thereby influencing the growth properties of the film. Accurately modeling the substrate, solution and PDAMNA monomers is beyond the scope of this work. What will be analyzed is the dependence of the chain molecule orientation on the fluid shear generated by the buoyancy-induced convection.

APPROACH

Since the molecular orientation of the PDAMNA molecules is the focus, the continuum equations of fluid dynamics will not be useful. Instead the technique of Molecular Dynamics (MD) simulation will be used. MD simulations involve the modeling of each atom or molecule and its motion within a very small portion of the system of interest. These motions arise from the interaction forces between the molecules. Certain configurational properties such as position and velocity are used to calculate various desired quantities utilizing Statistical Thermodynamics. The results are then extrapolated for use within the context of the entire system of interest. The field of MD simulation is well developed with a corresponding confidence in the results produced [3].

The investigation of the effect of fluid shear on the molecular orientation will proceed as follows. In Chapter 2 the physical system will be discussed in more detail. Various assumptions will be employed to simplify the system and a mathematical model will be developed which will be the basis for the MD simulation.

A discussion of previous work related to the mathematical model will take place in Chapter 3. These have served as guidelines and as checks during the development of the current work. Those elements necessary to extend the previous simulations in order to solve the mathematical model will be previewed.

Chapter 4 encompasses the development of the MD simulation for monatomic particles. It is not meant to be a comprehensive overview of MD techniques, however some of the choices that were made will be discussed. The development will be presented in much the same fashion as the code was constructed. The basics of the simulation will we explained and then more complex features will be added as they are required.

The rod-like particles will be discussed in Chapter 5. This includes the modifications to the monatomic development as well as additional considerations that were not encountered such as the rotation of the molecules. Finally, the measure of molecular orientation, which is at the core of this hypothesis, will be defined.

The results will be presented in Chapter 6. Results used to validate the basic simulation and the suitability of the channel flows will be presented. There the effect of the shear on the molecular orientation will be shown for various shear distributions, molecular concentrations, and wall and fluid densities. Chapter 7 contains the meaningful conclusions that may be drawn from these results and suggestions on future enhancements.

CHAPTER 2: PHYSICAL CONFIGURATION AND MATHEMATICAL MODEL

PHYSICAL CONFIGURATION

The physical configuration of interest is a very small region of fluid close to the substrate as seen in Figure 3. The motion of the fluid in this region is influenced by the entire volume of the fluid and may consist of a varying assortment of convection and boundary layer effects. The region of interest is composed of two parts, a fluid mass and a solid substrate. The fluid is a complex aggregate of PDAMNA monomers, small PDAMNA polymers, solution molecules, and solution impurities. These molecules interact through a variety of forces. Some may be electrically neutral, others may be strongly charged ions. The PDAMNA monomers themselves have a certain charge distribution along the length of the molecule. There may also be dipole, quadrupole, and higher order interactions to take into account.

The fluid is not necessarily homogeneous or isotropic. There might even be chemical reactions taking place within the fluid which change its makeup. There will definitely be some reduction in the concentration of the PDAMNA molecules as they adhere to the surface.

The solid substrate is an irregular crystal lattice which may possess impurities as well. The surface is likely to consist of a distribution of charges. There may also be PDAMNA molecules already adsorbed onto the surface. The fluid molecules may have an effect on the substrate itself such as inducing vibration or changing the temperature. Molecules may even dissociate from the substrate and be incorporated into the fluid.

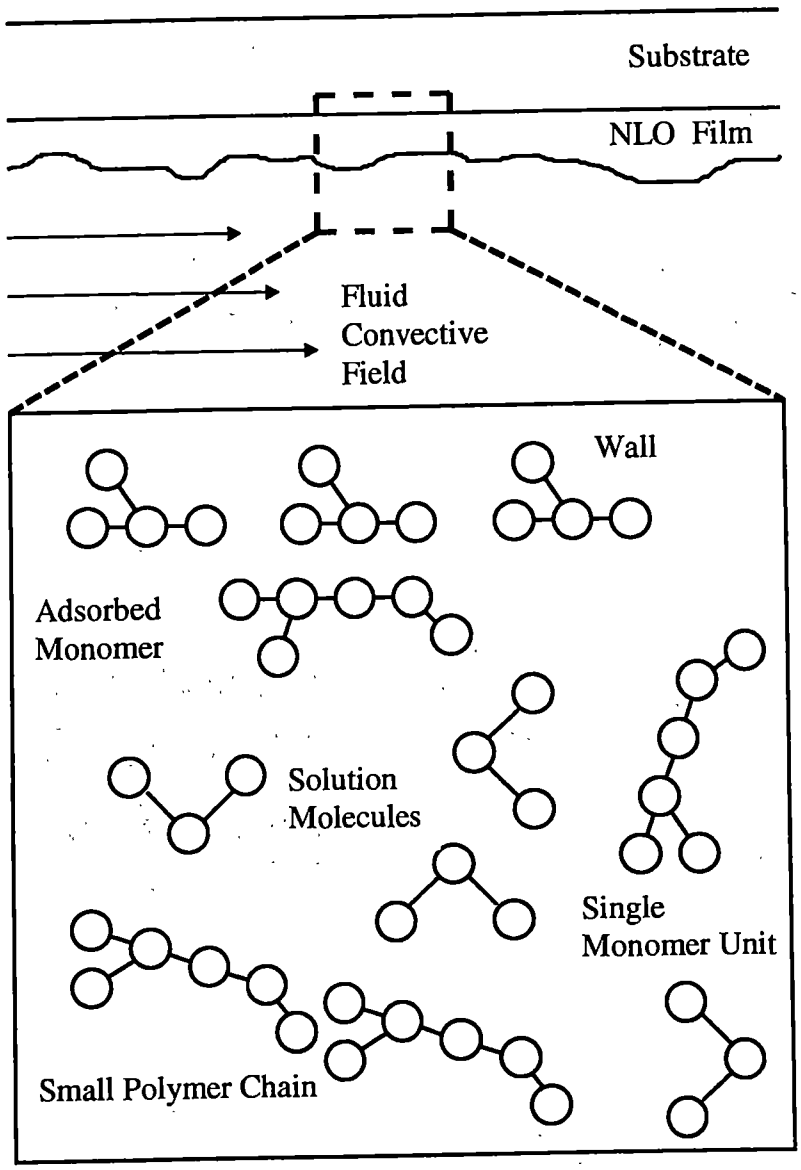

Figure 3. Representation of the physical configuration.

The computational resources required to fully model this system and all its details are not available, even for a very small region of fluid. The theory of the molecular processes behind some of the phenomena is still not at a point where it can be properly implemented in this type of simulation. However, not all of the complexities mentioned are essential to the question at hand. Some assumptions will have to be made in order to make the problem tractable. The key is to make simplifications that affect the desired results as little as possible.

ASSUMPTIONS

The following assumptions will be made in order to reduce the physical configuration to a manageable mathematical model. Some of the concepts will be discussed in more detail later on. These are the main limitations made to the code; more subtle assumptions may arise later on and will be treated where they appear.

- Quantum mechanical considerations are neglected. All particles are treated as bodies obeying the classical laws of translation, rotation and vibration.

- Molecular vibration will not be accounted for. Vibrational motion takes place on a time scale several orders of magnitude smaller than rotation and translation which are the motions of interest.

- As a side effect of the previous assumption, chemical reactions will not be considered and are not of interest regardless.

- The initial state of the fluid will be considered to be homogeneous if only one type of molecule is present and uniform if there are more than one.

- Atoms will be assumed to be spheres with a spherical potential.

- Molecules will be assumed to be a rigidly linked chain of atoms, hereafter referred to as sites to reduce ambiguity.

- All atoms and sites are considered to be point masses with a surrounding interaction potential.

- The PDAMNA molecules will be modeled as a simple linear chain of sites. The rod-like nature of the molecule is the salient feature in determining orientation effects. This assumption is a compromise based on computational resources.

- The interactions between all atoms and sites will be the Lennard-Jones (12-6) potential. The details of this choice are presented later. No electrostatic forces are included in this simulation, another casualty of limited resources.

- Where solution particles are to be included, they will be limited to simple atoms. The effect of the molecular concentration is the focus, not the molecule-solution interaction.

- The substrate in the simulation will be a regular crystal lattice with no peaks or valleys or monomers attached. Although the presence of a wall is integral to the simulation, the actual structure of the wall is of less importance.

- As will be discussed in a later chapter, boundary conditions come in pairs. Therefore the simulation will actually represent the flow in a narrow channel. It is assumed that the results in one half of the channel will closely approximate the flow near a wall where the other wall is comparatively very far away.

- The velocity caused by convection will be simulated by generating a flow in the channel. Again it is assumed that the results will correspond to velocity flows caused by buoyancy-induced convection.

- The wall particles will be constrained to move at a constant specified velocity. This is equivalent to assuming negligible wall vibration and results in an adiabatic wall condition.

- Any pressure gradients applied to the system will be assumed to act like body forces on each particle.

MATHEMATICAL MODEL

The resulting mathematical model, then, is a collection of N_f fluid particles, and N_w wall particles. This model is represented in Figure 4. The total number of particles is then $N_f + N_w = N_t$. The fluid particles each obey the following equation of translational motion:

$$\frac{d^2\mathbf{r}_i}{dt^2} = \frac{1}{m_i}\mathbf{F}_i$$

where $\mathbf{r}_i$ is the position vector of the center of mass of particle i, t is time, m_i is the mass of particle i and $\mathbf{F}_i$ is the resultant force vector acting on particle i. Unless otherwise specified, $i = 1, \ldots, N_f$. The wall particles obey the equations:

$$\begin{aligned} &\frac{d^2\mathbf{r}_j}{dt^2} = 0 \\ &\frac{dr_{j\,x}}{dt} = V_w \qquad j = N_f + 1, .., N_t \end{aligned} \tag{2–1}$$

where $r_{j\,x}$ is the x-component of $\mathbf{r}_j$ and V_w is the fixed velocity of the wall (possibly 0).

$\mathbf{F}_i$ is calculated by summing the components of the force $\mathbf{F}_{ij\alpha\beta}$ exerted by each site β of particle j on each site α of particle i:

$$\mathbf{F}_i = \sum_{\substack{j=1 \\ j\neq i}}^{N_t} \sum_{\alpha=1}^{S_i} \sum_{\beta=1}^{S_j} \mathbf{F}_{ij\alpha\beta} \tag{2–2}$$

where S_i represents the number of sites on particle i. Of course, when the interaction involves two atoms, this reduces to:

$$\mathbf{F}_i = \sum_{\substack{j=1 \\ j\neq i}}^{N_t} \mathbf{F}_{ij} \tag{2–3}$$

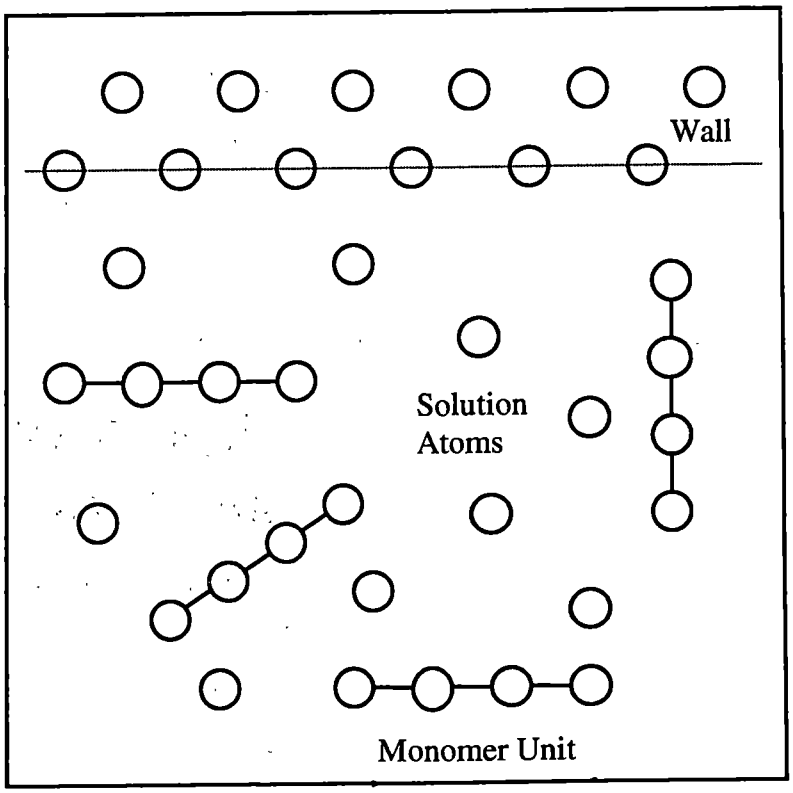

Figure 4. Mathematical model.

A schematic of the resultant interaction between atoms is presented in Figure 5. It should be noted that while the effect of the wall particles on the fluid particles is included, the reaction force on the wall particles is not. In practice the number of calculations will be halved by recognizing that the forces are conservative and so $\mathbf{F}_{ij} = -\mathbf{F}_{ji}$.

The exact form of the force $\mathbf{F}_{ij\alpha\beta}$ depends upon the interaction potential, U, in the following manner:

$$\mathbf{F}_{ij\alpha\beta} = -\frac{\partial U}{\partial r_{ij\alpha\beta}} \tag{2–4}$$

where $r_{ij\alpha\beta}$ is the magnitude of the distance vector $\mathbf{r}_{ij\alpha\beta}$ between site α on particle i and site β on particle j. The form of the Lennard-Jones (12-6) potential used in the simulation will be shown here although it will be discussed in detail in Chapter 4:

$$U = 4\epsilon \left[\left(\frac{\sigma}{r_{ij\alpha\beta}} \right)^{12} - \left(\frac{\sigma}{r_{ij\alpha\beta}} \right)^{6} \right] \tag{2–5}$$

where σ is the separation at which the potential is zero and ϵ is the minimum value of the potential.

For the rigid body molecules, a system of coordinates corresponding to the principal axes of inertia will be used and is denoted by ($'$). This frame of reference is also referred to as a system of body fixed coordinates. A common system in which the equations of rigid body motion are developed is the Euler angle formulation where the coordinates are ϕ, a rotation about the z-axis, θ, a rotation about the new x-axis, and ψ, a rotation about the new z-axis [4]. The equations of rotational motion are then:

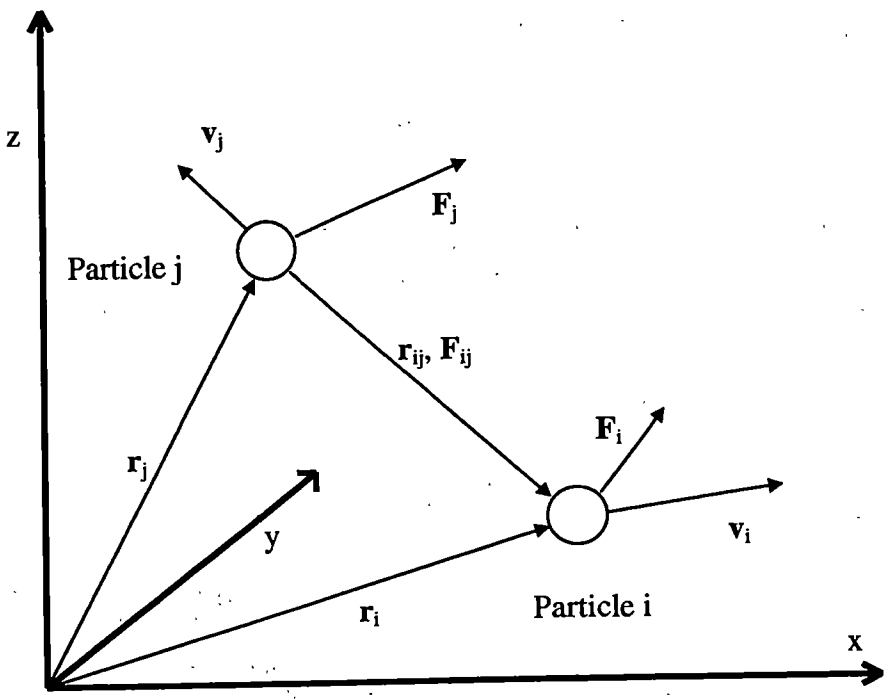

Figure 5. Schematic of the interaction between two atoms.

$$\begin{aligned}
\frac{d\omega'_x}{dt} &= \frac{\tau'}{I_{xx}} + \left(\frac{I_{yy} - I_{zz}}{I_{xx}}\right)\omega'_y\omega'_z \\
\frac{d\omega'_y}{dt} &= \frac{\tau'}{I_{yy}} + \left(\frac{I_{zz} - I_{xx}}{I_{yy}}\right)\omega'_z\omega'_x \\
\frac{d\omega'_z}{dt} &= \frac{\tau'}{I_{zz}} + \left(\frac{I_{xx} - I_{yy}}{I_{zz}}\right)\omega'_x\omega'_y
\end{aligned} \tag{2–6}$$

where the I are the components of the inertial stress tensor, ω_i is the angular velocity about the i axis, and τ_i is the torque about the i axis. The relation between the angular velocities and the angles is expressed as follows:

$$\begin{aligned}
\frac{d\phi}{dt} &= -\omega_x \frac{\sin\phi\cos\theta}{\sin\theta} + \omega_y \frac{\cos\phi\cos\theta}{\sin\theta} + \omega_z \\
\frac{d\theta}{dt} &= \omega_x \cos\phi + \omega_y \sin\phi \\
\frac{d\psi}{dt} &= \omega_x \frac{\sin\phi}{\sin\theta} - \omega_y \frac{\cos\phi}{\sin\theta}
\end{aligned} \tag{2–7}$$

Note that the angular velocities in this equation are expressed in space fixed coordinates. The conversion between the two coordinate reference frames is accomplished through the use of a rotation matrix $\mathbf{A}$ which is necessarily orthogonal, for example:

$$\mathbf{r}' = \mathbf{A} \cdot \mathbf{r} \tag{2–8}$$

where, using the abbreviations $c(x) = \cos x$ and $s(x) = \sin x$,

$$\mathbf{A} = \begin{bmatrix} c(\phi)c(\psi) - s(\phi)c(\theta)s(\psi) & s(\phi)c(\psi) + c(\phi)c(\theta)s(\psi) & s(\theta)s(\psi) \\ -c(\phi)s(\psi) - s(\phi)c(\theta)c(\psi) & -s(\phi)s(\psi) - s(\phi)c(\theta)c(\psi) & s(\theta)c(\psi) \\ s(\psi)s(\theta) & -c(\phi)s(\theta) & c(\theta) \end{bmatrix} \tag{2–9}$$

A relation similar to equation (2-8) would apply for the angular velocity vector and the vector representing the orientation of the molecule. These are the equations that are solved using the molecular dynamics program. The boundary

and initial conditions are more a matter of implementation than of equations and will be discussed in a later chapter.

NON-DIMENSIONALIZATION

MD simulations are conventionally performed using a system of units in which all the quantities are dimensionless. This will, for example, allow the results of a single simulation to be applied to a various class of particles with similar potentials, simply by varying the parameters used to restore dimensionality. Non-dimensionalization also makes the magnitudes of most variables commensurate with unity.

There are four basic values that are used to non-dimensionalize all the quantities: N_f, the number of fluid particles; m_r, the mass of a reference particle, if all the particles are the same $m_r = m_i$; ϵ, an energy scale; and σ, a length scale. The latter two are taken from the Lennard-Jones (12-6) potential for the representative particle. A time scale can be constructed from these parameters, $t_r = \sigma\sqrt{m/\epsilon}$

The variables in the equations above are then non-dimensionalized (represented by (*)) as follows:

$$
\begin{aligned}
m^* &= \frac{m}{m_r} \\
t^* &= \frac{t}{t_r} \\
\mathbf{r}^* &= \frac{\mathbf{r}}{\sigma} \\
\omega^* &= \omega t_r \\
\mathbf{F}^* &= \frac{\mathbf{F}\sigma}{\epsilon} \\
\tau^* &= \frac{\tau}{\epsilon} \\
I^* &= \frac{I}{m_r \sigma^2} \\
T^* &= \frac{Tk}{\epsilon} \\
E^* &= \frac{E}{N_f \epsilon} \\
U^* &= \frac{U}{\epsilon} \\
P^* &= \frac{P\sigma^3}{\epsilon}
\end{aligned}
\tag{2–10}
$$

where E is the total energy, U is the potential energy per particle, T is the temperature, P is the pressure, and k is the Boltzmann constant.

The equations are such that their non-dimensionalization changes very little. The non-dimensionalized equations are presented here for completeness. The new equations of translational motion for the fluid particles are:

$$
\frac{d^2\mathbf{r}_i^*}{dt^{*2}} = \frac{1}{m_i^*}\mathbf{F}_i^* \tag{2–11}
$$

$$
\mathbf{F}_i^* = \sum_{\substack{j=1 \\ j\neq i}}^{N_t} \sum_{\alpha=1}^{S_i} \sum_{\beta=1}^{S_j} \mathbf{F}_{ij\alpha\beta}^* \tag{2–12}
$$

$$
\mathbf{F}_{ij\alpha\beta}^* = -\frac{\partial U^*}{\partial r_{ij\alpha\beta}^*} \tag{2–13}
$$

$$U^* = 4\left[\left(\frac{1}{r^*_{ij\alpha\beta}}\right)^{12} - \left(\frac{1}{r^*_{ij\alpha\beta}}\right)^{6}\right] \tag{2–14}$$

The non-dimensionalized equations of rotation are then:

$$\begin{aligned}
\frac{d\omega_x^{*\prime}}{dt^*} &= \frac{\tau^{*\prime}}{I^*_{xx}} + \left(\frac{I^*_{yy} - I^*_{zz}}{I^*_{xx}}\right)\omega_y^{*\prime}\omega_z^{*\prime} \\
\frac{d\omega_y^{*\prime}}{dt^*} &= \frac{\tau^{*\prime}}{I^*_{yy}} + \left(\frac{I^*_{zz} - I^*_{xx}}{I^*_{yy}}\right)\omega_z^{*\prime}\omega_x^{*\prime} \\
\frac{d\omega_z^{*\prime}}{dt^*} &= \frac{\tau^{*\prime}}{I^*_{zz}} + \left(\frac{I^*_{xx} - I^*_{yy}}{I^*_{zz}}\right)\omega_x^{*\prime}\omega_y^{*\prime}
\end{aligned} \tag{2–15}$$

$$\begin{aligned}
\frac{d\phi}{dt^*} &= -\omega_x^* \frac{\sin\phi\cos\theta}{\sin\theta} + \omega_y^* \frac{\cos\phi\cos\theta}{\sin\theta} + \omega_z^* \\
\frac{d\theta}{dt^*} &= \omega_x^* \cos\phi + \omega_y^* \sin\phi \\
\frac{d\psi}{dt^*} &= \omega_x^* \frac{\sin\phi}{\sin\theta} - \omega_y^* \frac{\cos\phi}{\sin\theta}
\end{aligned} \tag{2–16}$$

$$\tau^{*\prime} = \mathbf{A} \cdot \tau^* \tag{2–17}$$

The rotation matrix $\mathbf{A}$ does not change with the non-dimensionalization. These forms of the equations of motion will be used through the remainder of this study, and special mention of the units will be made where dimensional quantities are given.

CHAPTER 3: PREVIOUS WORK

MOLECULAR DYNAMICS

At a fundamental level the process of Molecular Dynamics simulation is an attempt to solve the N-body problem with N as large as possible. Each individual atom or part of a molecule acts on every other with a force which is a function of the separation and, in very complex models, a function of the relative orientation. This problem admits no analytic solution and so MD simulation is an inherently numerical process.

It is possible to include only binary collisions, as is done in gas kinetic theory. However, as the name implies, gas kinetic theory is most useful for investigating gases where the density is low and this assumption does not create large errors [5]. MD simulations are typically employed to simulate the much higher densities found in liquids. At these densities, a particle may interact with anywhere from 10 to 50 other particles simultaneously rendering the assumption of binary collisions unusable. Even for the simplest of simulations, the number of computations is quite large so it is no surprise that the development of MD simulations is intimately connected with advances in computational power.

In the late 1950's Alder [6-23] began a long series of studies on Molecular Dynamics. The first few were very simple simulations. They involved a collection of 32 and 108 atom systems. The atoms were modeled as hard spheres, interacting only through perfectly elastic collisions. The simulations were also two dimensional with periodic boundary conditions. Even with such simplifications it took an hour of CPU time to compute 2000 collisions for a 100 particle system. Despite the computational limitations, Alder was able to provide key insights into the

fundamentals of MD simulations that are used in current multi-million particle computations.

One of the most important issues to examine was the question of scale. Is it realistic to expect that a simulation of even a million particles over the course of a microsecond will produce results applicable to collections of more than 10^{23} particles over a second or longer? Even the simple early simulations performed by Alder and collaborators suggested that the errors introduced by disparities in scale are smaller than statistical errors for simulations of 500 particles or more [6,7]. These results serve as experimental justifications. A more theoretical justification utilizing the concept of phase space is presented in the next chapter.

One of the first MD applications presented by Alder *et al* was the investigation of phase change [7]. They were able to establish phase diagrams for hard disks and spheres for as few as 100 and 500 particles respectively. To this point only simple thermodynamic quantities such as the temperature and density had been calculated. Later simulations involved more complicated quantities including pressure, entropy and Gibbs free energy [8,9,10]. These simulations also explored mixtures of hard spheres and extended the limits of high and low density.

This series of papers by Alder and various co-investigators led into the 1980s. The square-well potential was added to their investigations [11,15,22] and the calculated thermodynamics quantities became quite specialized [19,20]. The MD simulations were also used to partially validate various theories concerning equations of state for certain types of particles [10,23].

By the 1980s MD simulations had achieved a broad popularity among those researching fluid physics. Beginning in the latter half of the decade, textbooks were written which compared and contrasted the different methods that had been employed and presented all the necessary tools in a concise form [24-28]. The

fundamentals of the MD simulation method have become well established, but there are still differing views concerning the best way to perform some of the more advanced techniques.

CHANNEL FLOWS

In this simulation a channel flow will be established in order to generate shear within the fluid. It is also possible to simulate shear flow by applying a shear boundary condition [29-31]. This type of simulation allows more direct control over the shear. It does not, however, provide any information concerning the contribution of the wall to the effects of the shear.

Many MD simulations have been performed to investigate the behavior of fluid at the wall interface [32-37]. These walls were made of particles similar to the fluid particles. One of the primary concerns in these simulations was the question of the applicability of the no-slip boundary condition at molecular scales. Various results have been obtained, from the demonstration of no-slip within two molecular diameters [35] to consistent observation of slip within the same distance [32]. The one clear conclusion seems to be that fluid behavior at the wall is highly dependent on the wall and fluid densities, the wall configuration, and the relative strengths of interaction for the fluid and wall particles [37]. Figure 6 shows some of these effects.

Two main types of channel flow are studied in these simulations. A typical channel flow density profile is shown in Figure 7. In the plane Couette flow, as shown in Figure 6, constant shear is generated by moving the two channel walls at constant but unequal velocities. On the other hand, variable shear flow is generated by a pressure gradient, also known as plane Poiseuille flow. Figure 8 presents an example of a plane Poiseuille flow simulation. Both of these flows are

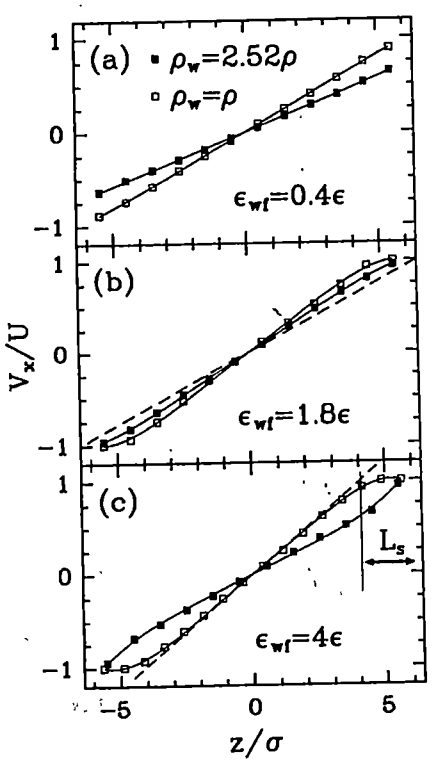

Figure 6. Velocity dependence on wall density and strength. U is the wall velocity, V_x is the x-component of velocity, L_s is a slip length, and the rest of the parameters were defined previously noting that the subscripts w and wf refer to wall properties. Dashed lines represent expected profiles from continuum analysis. Source: Thompson, P. A., and Robbins, M. O., "Shear flow near solids: Epitaxial order and flow boundary conditions", *Physical Review A* **41** (1990) 6830-6837.

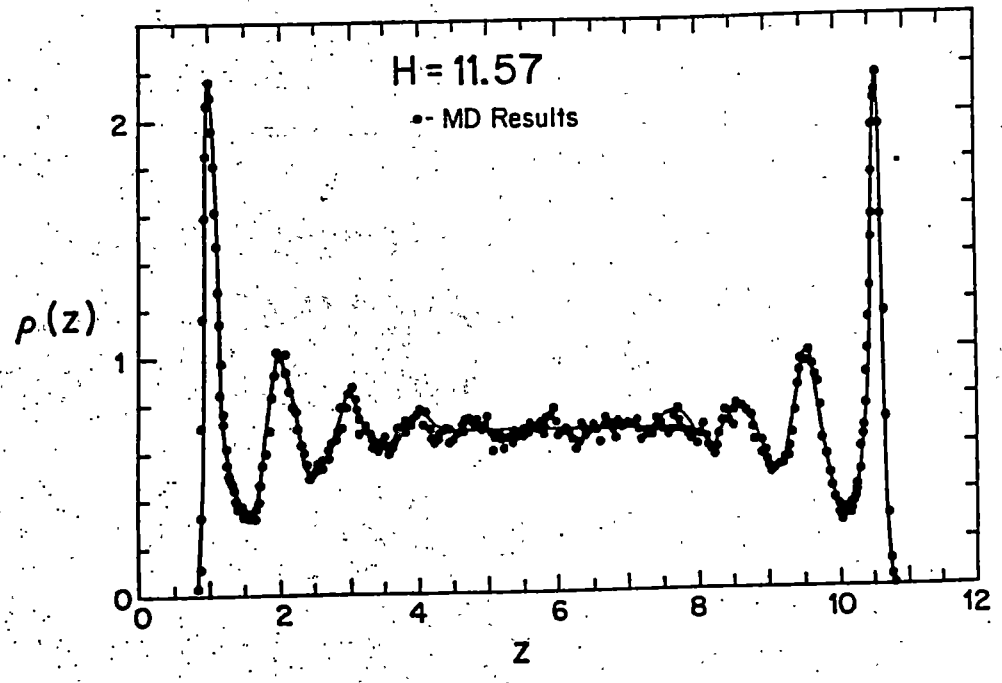

Figure 7. Density profile for a narrow pore. H is the pore separation. Source: Magda J. J., Tirrell, M., and Davis, H. T., "Molecular dynamics of narrow, liquid-filled pores", *Journal of Chemical Physics* **83** (1985) 1888-1901.

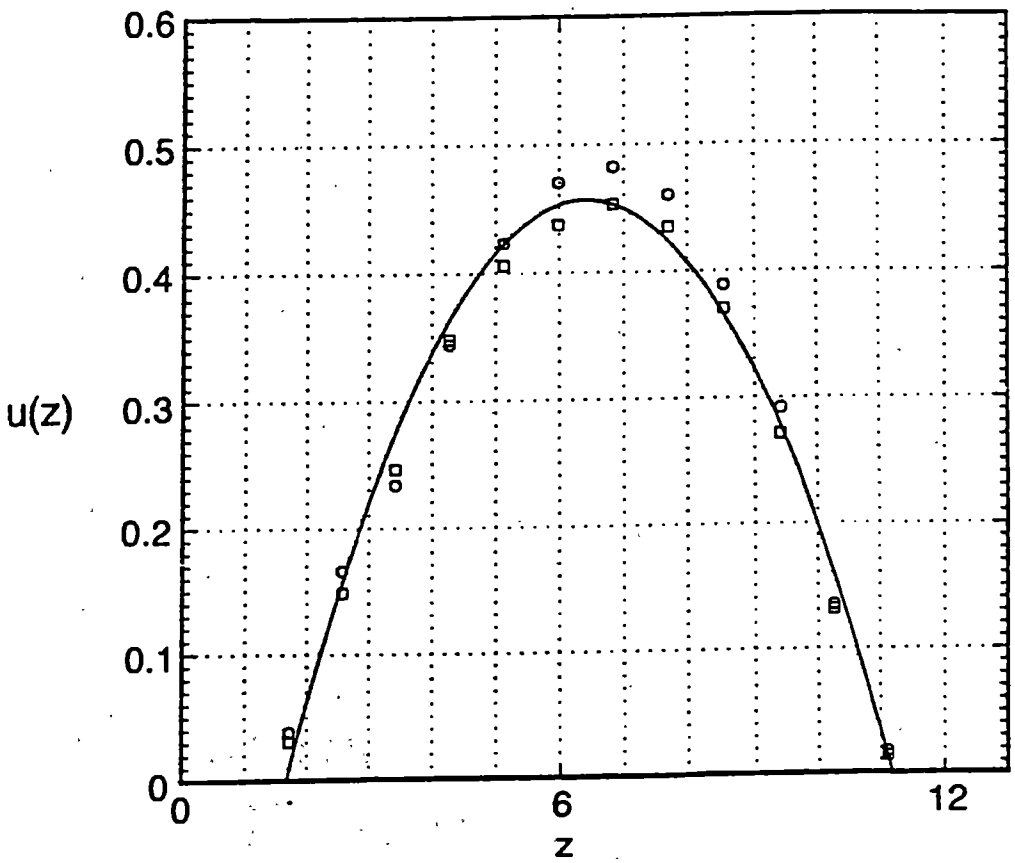

Figure 8. Velocity profile of a plane Poiseuille flow. $u(z)$ is the x-component of the velocity as a function of z. Source: Koplik, J., Banavar, J. R., and Willemsen, J. F., "Molecular Dynamics of Poiseuille Flow and Moving Contact Lines", *Physical Review Letters* **60** (1988) 1282-1285.

used in the current study and the details of their implementation will be presented in Chapter 4.

Various studies have also been carried out investigating the calculation of thermodynamic properties in narrow channel flows [38-41]. A commonly studied property is the viscosity. These simulations conclude that calculating a viscosity averaged over the entire channel provides results that are incompatible with continuum fluid dynamic theory. They suggest that viscosities and other properties should be calculated on a highly localized basis. Simulations of this kind, where fluid properties vary from position to position are known as non-equilibrium molecular dynamics simulations, NEMD. The shear currently under investigation is a non-equilibrium phenomenon. Other NEMD simulations employing a channel include the study of Taylor-Couette vortex formation [42] and Rayleigh-Bénard convection [43].

The driving force for the channel flow introduces excess energy into the flow, whether it be through the moving walls or the pressure gradient. Some method of extracting the energy must be employed to maintain the temperature of the system. For the channel flows, it is the temperature that is maintained rather than the energy. It is therefore a canonical thermodynamic ensemble (constant N,V,T) rather than the microcanonical ensemble used for the basic simulation (constant N,V,E).

Various methods have been employed to maintain constant temperature in a molecular dynamics simulation. Haile and Gupta [44] break the choices into four categories: a straightforward scaling of the velocities to yield the desired temperature; the introduction of a constraint parameter to adjust the accelerations and maintain the temperature; coupling the system to a heat bath where the combined systems form a microcanonical ensemble [45]; and employing phantom particles

which collide with particles in the system in a stochastically determined way to restore the system to the Maxwellian distribution at the appropriate temperature. The first two methods are presented in greater detail in Chapter 4. The other two methods will not be discussed further.

ORIENTATION EFFECTS

Many of the simulations described have used spherical monatomic particles to model the fluid. New realms of investigation are opened when molecules are employed. Travis and Evans simulated the effect of shear in a plane Poiseuille flow on the induced molecular rotation [46]. They found that the results agreed reasonably well with continuum theory except near the wall.

Rapaport performed studies on molecular orientation in a plane Poiseuille flow [47]. The molecules used consisted of both hard sphere and Lennard-Jones type particles linked together to form a rod. These simulations showed that the molecular orientation in such a flow varies across the channel. Near the wall, the particle orientation was quite pronounced in its bias towards a horizontal position parallel to the wall and in the direction of the flow. In the center of the channel there was little bias toward any particular orientation. Rapaport suggested that these results corresponded to the variation in the shear across the channel.

NEW GROUND

The current investigation seeks to enlarge upon the previous simulations in certain areas. First, plane Poiseuille flow, plane Couette flow, and no flow simulations will be performed in an effort to isolate the effect of the shear. By studying flows of variable, constant and zero shear respectively it is anticipated that it will

be possible to filter out spurious effects. Comparison of the three may also provided some insight concerning the anomalous effects that are sometimes observed near the walls.

The simulations discussed also used either homogeneous fluids, or fluid mixtures in which the difference between the fluid particle types is trivial. This study will include simulations in which the long-chain molecule is contained in a solution of spherical particles. This should provide an indication of the influence of monomer concentration on the orientational effects.

The long-chain molecules of different sizes and configurations will be modeled by varying both the number of sites and the distances between the sites. In a previous section it was noted that the density and configuration of the wall can also have a significant effect on the behavior of the nearby fluid. Varying wall densities will therefore be utilized as well to help isolate the effect of the no-slip condition on the shear distribution.

CHAPTER 4: IMPLEMENTATION - SPHERICAL ATOMS

This chapter will discuss the details of the current MD simulation and how the various ideas are implemented. The development of the program followed an orderly progression from a very simple simulation to the more complex simulation used for the results. This discussion will follow the same development. Homogeneous spherical particles, referred to as atoms, will be discussed first. Those elements common to all stages of the development process will be explored using atoms first and then augmented to include the rods.

The details of the simulation developed to test the hypothesis given in Chapter 1 will be presented. Various options exist for many of the steps in the simulation development, and the rationale for some of the choices made will be discussed. This is not a comprehensive discussion of MD simulations and the reader is referred to other sources for more details [24-28]

PHASE SPACE

As discussed in Chapter 2, one of the most significant assumptions being made is that the examination of a collection of thousands of particles for a nanosecond can reveal anything useful about a system of 10^{23} particles over a second or longer. This question is perhaps more easily resolved by enlisting the concept of phase space.

Consider a system of N_∞ spherical particles, where N_∞ is of the order 10^{23}. Each of these particles has a position specified by its three coordinates. Three additional values specify the three component velocities of each particle as well. These six values, or degrees of freedom, exist for each particle, yielding $6N_\infty$ in total. This value should be reduced by six when the position and velocity of the center of mass of the system are specified, but this is insignificant for this

discussion. Phase space is the name given to the $6N_\infty$ dimensional space in which the coordinates of each point are the positions and velocities of every particle in the system at a given point in time.

If the system of particles is allowed to advance with time according to a given set of laws, the subsequent points in phase space will trace out a trajectory on a hyper-surface. A given property of interest may then be calculated by taking an average over each point in time, known as a trajectory average. The trajectory calculated by tracing a system as it changes with time is the domain of Molecular Dynamics. If the system is ergodic than this trajectory will eventually pass through all the points in phase space available to the system. The simulations discussed in Chapter 6 will be assumed to be ergodic.

A second way of obtaining the phase space trajectory would be to randomly generate a series of samples of the $6N_\infty$ particle system. These samples are chosen from a given statistical ensemble and are constrained by certain parameters such as the energy and the volume available to the system. The required thermodynamic properties are then calculated using these statistical ensembles. This is the technique employed by the Monte Carlo simulation method (MC).

A popular way of validating results is to compare a MD simulation and a MC simulation. This is limited to results involving equilibrium averages, however. As discussed earlier, MD is also used to investigate non-equilibrium and time-dependent phenomena which are more dependent on its unique capabilities for their calculation.

The resolution of the question of time is now accessible. Statistical theory shows that if the length of the overall trajectory is very long compared with the portion that is sampled, then the accuracy of any averages computed depend only on the length of the sample and not on the length of the overall trajectory [27].

That is to say that assuming that the sample simulation run of one nanosecond is sufficiently long, it's computed averages predict equally well the averages computed over milliseconds or hours.

There is still the issue of the length of simulation required to ensure that the computed averages are of adequate accuracy. Various methods exist to determine whether sufficient accuracy has been achieved. A simple way is to take averages over the first half and the last half of the simulation separately. When these two averages agree to the desired precision, it is then reasonable to assume that a longer trajectory will not modify the results. Another method would be to run a similar simulation with different initial conditions and compare the resulting values.

This discussion has provided reasonable justification of the use of short simulation runs. The concept of phase space is again useful when considering the use of a small number of particles, 10^3 or 10^6 vs 10^{23}. Consider the surface of a sphere in three dimensions. It is defined by its radius, R, just as the hyper-surface discussed previously is defined by its energy. If one coordinate is held constant, the z-coordinate for example, the resulting surface is a circle with radius $(R^2-z^2)^{\frac{1}{2}}$. A simulation using $N = 1000$ particles can be viewed in a similar fashion. Its range in phase space is that hyper-surface described by holding the other $6(N_\infty - N)$ coordinates constant and is described by a correspondingly lower energy.

There are various ways to investigate the comparison between averages computed over this much smaller hyper-surface and the original hyper-surface. The method originally employed by Alder was to run multiple simulations with different values of N and compare the results. When an increase in N yields no further changes in the properties, it is then reasonable to conclude that the averages from

the smaller hyper-surface are representative of that of the whole. When the particles simulated closely model a physical substance, monatomic Argon is a common example, then physical experiments can be performed and the results compared.

Experience with MD simulations has bred confidence that the small time and size limitations of MD do not in general negate the applicability of the results to more familiar scales. These limitations should always be kept in mind, however, and not blindly assumed to be negligible. Whenever discrepancies arise or seemingly incongruent results are obtained, one of the first questions to be considered should be the possible influence of the small size and time scales.

PARTICLE INTERACTION

One of the defining characteristics of the simulation is the particle interaction. This is specified by the exact form of the potential that is used in calculating the force between two particles. The potential depends upon the magnitude of the separation between the two particles under consideration. As mentioned, the current development is being performed for atomic particles and so this separation is the separation between particle i and particle j, r_{ij}.

Some of the simpler potentials that have been used include:

1. Hard Sphere: $$U = \begin{cases} \infty, & r_{ij} \leq r_1; \\ 0, & r_{ij} > r_1. \end{cases}$$

2. Square Well: $$U = \begin{cases} \infty, & r_{ij} \leq r_1; \\ -U_c, & r_1 < r_{ij} \leq r_2; \\ 0, & r_{ij} > r_2. \end{cases}$$

3. Soft Sphere: $$U = cr_{ij}^{-k}$$

where r_1, r_2, U_c, c, and k are parameters that can be adjusted to better simulate the desired system. These potentials are shown in Figure 9. These models are all simple conceptually as well as computationally. They are also entirely repulsive,

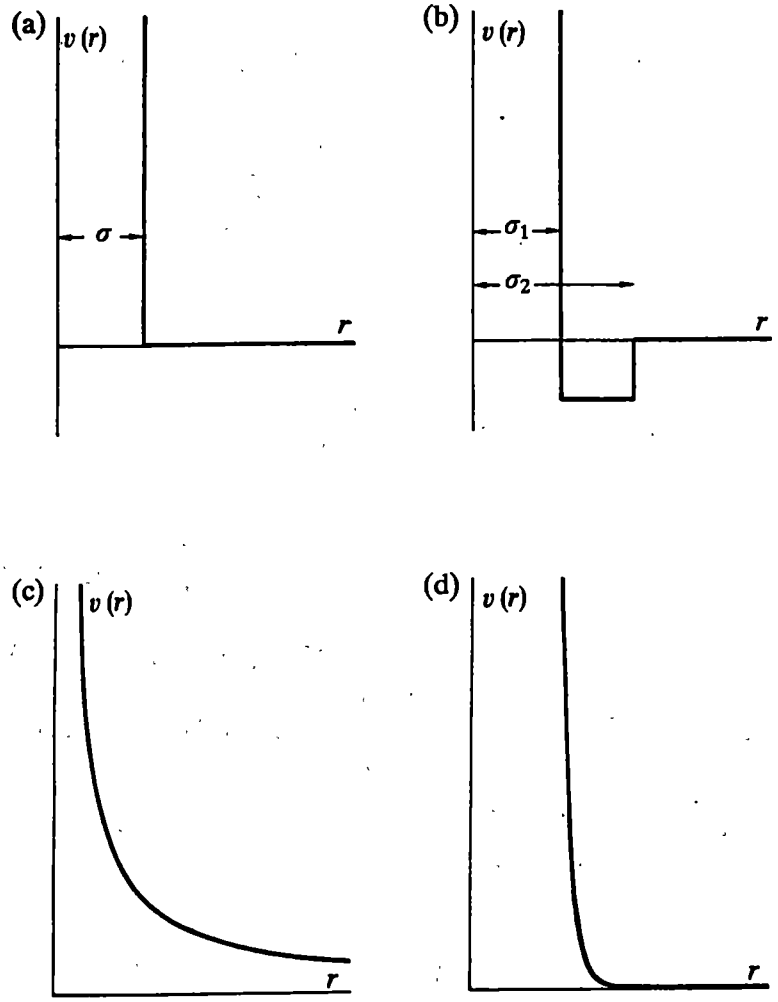

Figure 9. Idealized pair potentials. (a) The hard-sphere potential; (b) The square-well potential; (c) The soft-sphere potential with k=1; (d) The soft-sphere potential with k=12. Source: Allen, M. P., and Tildesley, D. J., *Computer Simulation of Liquids* Oxford University Press, New York, New York (1987).

that is to say, they cannot be used to model attractive forces between particles and are thus unsuitable for modeling many liquid characteristics.

A commonly used model with attractive capabilities is the Lennard-Jones potential,

$$U = c\epsilon\left[\left(\frac{\sigma}{r}\right)^m - \left(\frac{\sigma}{r}\right)^n\right] \tag{4–1}$$

The constants c, m, and n are defined by the particular type of Lennard-Jones model in use. On the other hand, ϵ and σ are parameters that are adjusted depending on the particle being simulated.

The Lennard-Jones (12-6) potential, in which $c = 4$, $m = 12$ and $n = 6$, is the most popular of the Lennard-Jones family and is the potential used in the current study. In this case, the potential is given by:

$$U = 4\epsilon\left[\left(\frac{\sigma}{r}\right)^{12} - \left(\frac{\sigma}{r}\right)^{6}\right] \tag{4–2}$$

In Chapter 2 this potential was non-dimensionalized yielding the following form:

$$U^* = 4\left[\left(\frac{1}{r_{ij}^*}\right)^{12} - \left(\frac{1}{r_{ij}^*}\right)^{6}\right] \tag{4–3}$$

As seen in Figure 10, this potential exhibits an attractive well, preceded by a very strong repulsive region that grows in strength with decreasing separation. The parameter ϵ is a measure of the depth of the attractive well and σ is the separation at which the potential is zero. This potential approximates fairly well the common electrically neutral atoms such as Argon while requiring little added computational complexity. More accurate relations are available but the increase

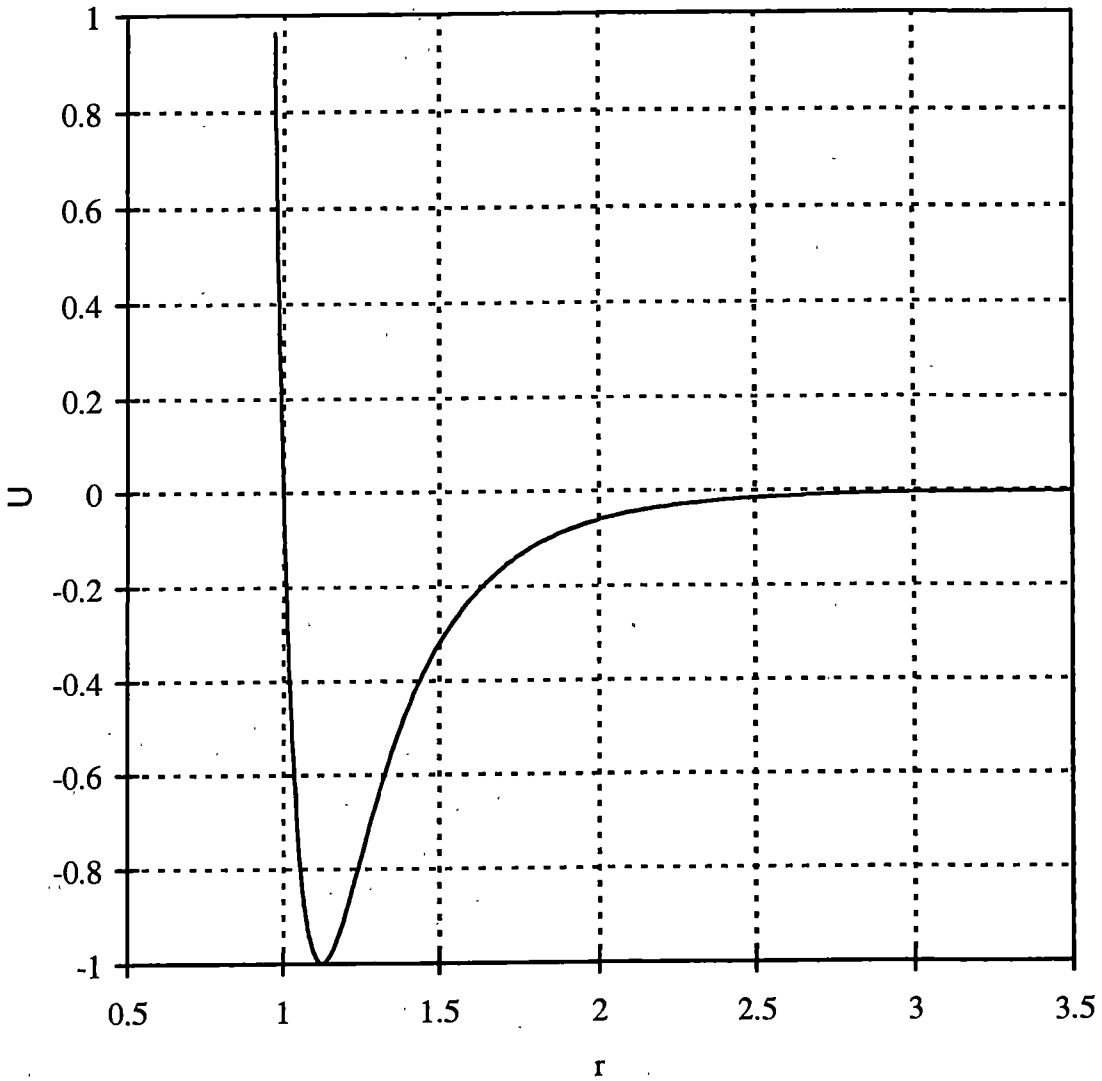

Figure 10. The Lennard-Jones(12-6) potential.

in calculation requirements limits their use. They require evaluation of exponentials, logarithms, or other time consuming elements. A comparison between the Lennard-Jones potential and a more sophisticated potential is presented in Figure 11. Unfortunately the Lennard-Jones potential is less accurate for the attractive well. This is especially problematic in the calculation of properties for fluids.

The problem is the conflict between the desired accuracy and the available computational resources. The time spent in calculating the force between the particles is crucial since the expression is evaluated many times per particle for every particle at every time step. For a system of 500 particles and 20 average interactions per particle, a billion evaluations are required for a modest run of 100,000 time steps. Clearly the slightest advantage in simplifying the force evaluation will result in a great savings.

One method of reducing this evaluation cost is to compute and store a numerical potential at a sufficiently fine level of discretization. Interpolation can then be used to obtain the magnitude of the potential for values of the radius lying between the stored values. Using this method, potentials can be made as complex as necessary without increasing the computation time for the force evaluation. Unfortunately, the time required to access the stored values from the array and perform the interpolation is greater than the time required to compute the simpler potentials including the Lennard-Jones (12-6) [26]. Thus, there is still the question of compromise between the shorter evaluation time of the simple potentials and the accuracy of those that are more complex. Since the molecules in the current study are simplified to a considerable extent the additional computational requirements of a more complex potential are not justified.

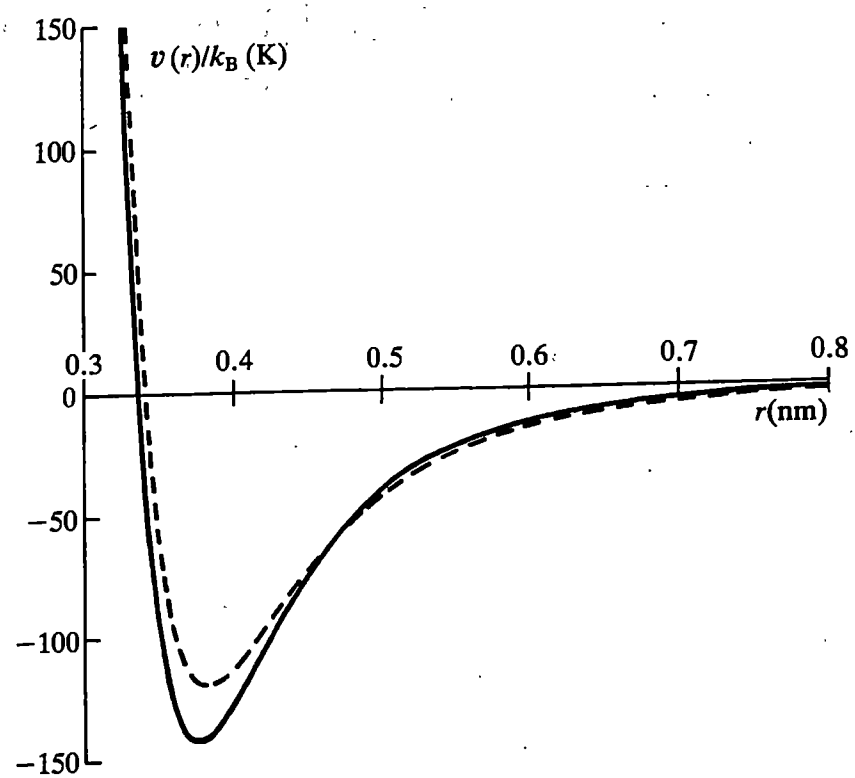

Figure 11. Comparison of Argon pair potentials. The solid line is the BBMS potential and the dashed line is the Lennard-Jones (12-6) potential. Source: Allen, M. P., and Tildesley, D. J., *Computer Simulation of Liquids* Oxford University Press, New York, New York (1987).

For particles with an electric charge, the situation becomes even more complex. The forces between particles decrease with r^{*-2}, much more slowly than the Lennard-Jones (12-6), resulting in their identification as long-range forces. As a further complication it is also known that the interaction of three or more particles acting simultaneously necessitates a contribution in addition to the pair-wise interactions. Calculation of more than the simple pair-wise interaction is beyond the reach of available computational resources.

POTENTIAL TRUNCATION

A widely used method of reducing the force calculation requirements is to truncate the potential. In the form given in equation (4-3), U^* is finite for all values of $r \neq 0$. This requires the computation of the force between all particles, an operation of order N^2 calculations per time step. For separations greater than 2.5 to 3 in the non-dimensionalized units, however, the contribution to the potential is very small. This leads to the concept of potential truncation. The truncated Lennard-Jones potential is shown in Figure 12 and is computed using the following equation:

$$U^* = \begin{cases} 4\left[\left(\frac{1}{r_{ij}^*}\right)^{12} - \left(\frac{1}{r_{ij}^*}\right)^{6}\right], & r_{ij}^* \leq r_c \\ 0, & r_{ij}^* > r_c \end{cases} \qquad (4\text{–}4)$$

where the truncation radius, r_c will be taken to be 2.5. Use of the truncation radius greatly reduces the number of force computations required. It should be noted that the utilization of the truncated potential means that the force derived from it experiences a discontinuous step at $r_{ij}^* = r_c$. Use of the truncated potential may also require corrections to be applied for certain thermodynamic properties such as the total potential energy and the virial function.

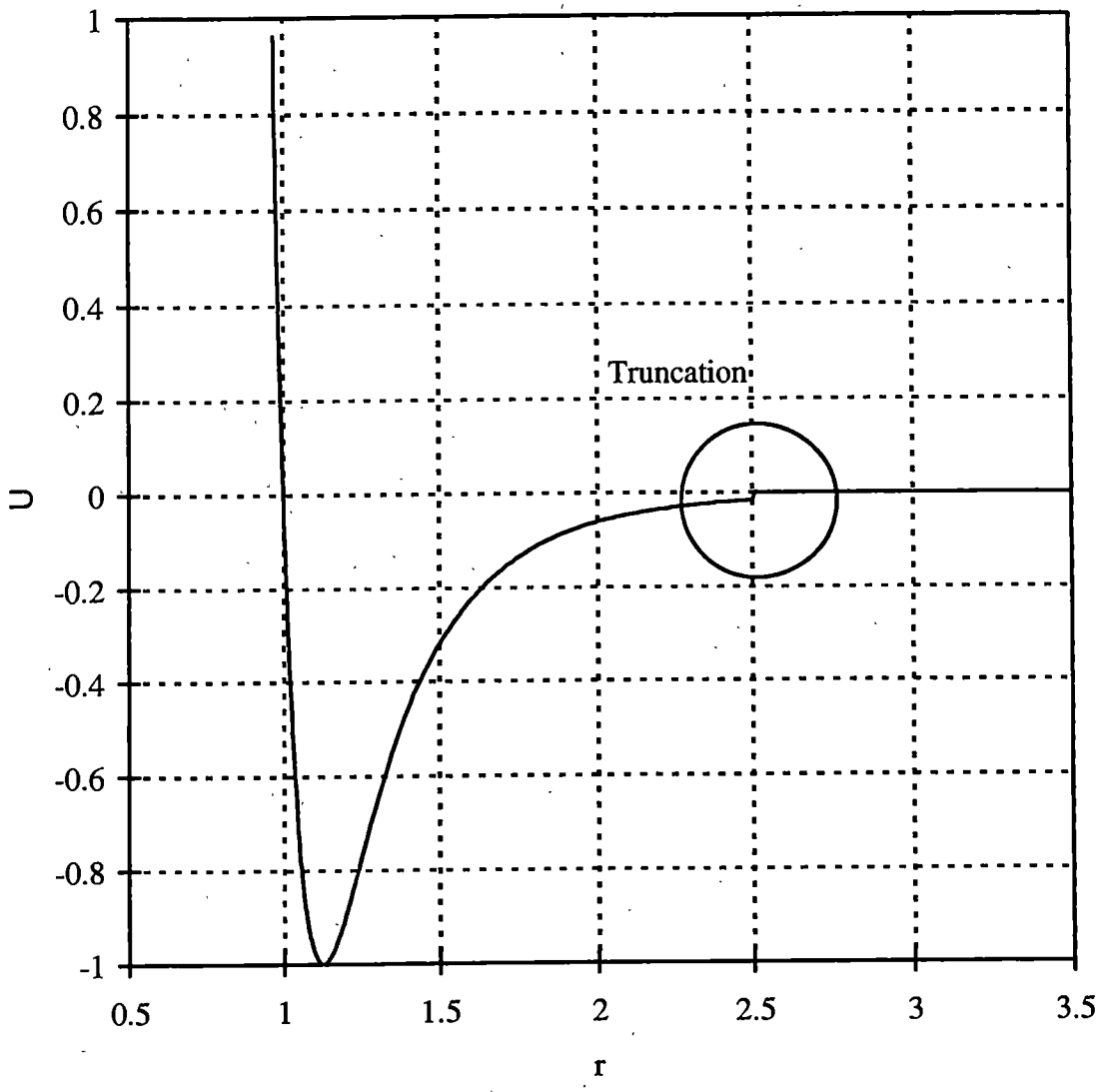

Figure 12. The Truncated Lennard-Jones (12-6) potential.

In general it is the potential function that is presented when characterizing a given simulation. However, when the code is implemented, it is the expression for the force that is required. For atomic particles, the force is calculated using:

$$F_{ij}^{*} = -\frac{\partial U}{\partial r_{ij}^{*}} \tag{4–5}$$

For the truncated Lennard-Jones this becomes:

$$F_{ij}^{*} = \begin{cases} -48\left[\left(\frac{1}{r_{ij}^{*}}\right)^{13} - \frac{1}{2}\left(\frac{1}{r_{ij}^{*}}\right)^{7}\right], & r_{ij}^{*} \leq r_c \\ 0, & r_{ij}^{*} > r_c \end{cases} \tag{4–6}$$

Unfortunately, this equation possesses something which the potential equation did not, namely, odd powers of the r_{ij}^{*}. Mathematically this is not a problem but computationally it is significant. The particle position vector is stored in Cartesian coordinate form, r_{ix}, r_{iy}, r_{iz}. The equation for the the magnitude of the separation is then:

$$r_{ij}^{*2} = (r_{ix}^{*} - r_{jx}^{*})^2 + (r_{iy}^{*} - r_{jy}^{*})^2 + (r_{iz}^{*} - r_{jz}^{*})^2 \tag{4–7}$$

In order to calculate r_{ij}^{*} alone, the square root function must be used. Taking square roots is numerically expensive, especially as a part of the force calculation. Wherever possible, it is best to use r_{ij}^{*2} and avoid the square root altogether.

This can be accomplished by taking into consideration the fact that the force $\mathbf{F}_{ij}^{*}$ is required in vector form. The force vector is coincident with the separation vector so the force components can be expressed as:

$$F_{ijx}^{*} = \frac{r_{ijx}^{*}}{r_{ij}^{*}} F_{ij}^{*} \tag{4–8}$$

with similar expressions for the other coordinate directions. With this in mind, the final form for the force calculation expression is:

$$F_{ij}^{*} = \begin{cases} \frac{-48}{r_{ij}^{*2}} \left[\left(\frac{1}{r_{ij}^{*}} \right)^{12} - \frac{1}{2} \left(\frac{1}{r_{ij}^{*}} \right)^{6} \right], & r_{ij}^{*} \leq r_c \\ 0, & r_{ij}^{*} > r_c \end{cases} \tag{4-9}$$

where it is understood that the force components are given by multiplying by the component of the separation vector:

$$F_{ij\,x}^{*} = r_{ij\,x}^{*} F_{ij}^{*} \tag{4-10}$$

with similar relations applying for the y and z coordinate directions. Previously, only the magnitude of the separation has been required. Now the direction becomes important. It is conventional for a negative force to designate attraction. The form of the preceding equations therefore requires that the vector $\mathbf{r}_{ij}$ originate at particle j and terminate at particle i.

NEIGHBOR LISTS AND CELLS

The last section discussed some of the advantages of using truncated potentials. There is a further significant advantage to employing these potentials, they facilitate the use of neighbor lists. Although the evaluation of the force itself as done in equation (4-9) requires great optimization, it is not the only component of the force calculation algorithm. The program must also calculate the separation between all the particles as shown in equation (4-7). Until now it has been assumed that all pairs of particles have their separations calculated, an order N^2 operation.

At any given time only a small fraction of the total particles will lie within a sphere of radius r_c around a given particle i. Over the next several time steps, there

is also a small percentage of particles that may enter this sphere of interaction. If a shell of certain thickness Δr_c is added to the sphere, then the only particles with which particle i will interact during several time steps lie within the sphere of radius $r_c + \Delta r_c$. The only distance calculations that need be performed are between these particles and particle i. A schematic representation of the neighbor list is shown in Figure 13. When N is large compared to the number of these neighbor particles, a substantial savings results.

The list of neighbors for all the particles can be stored in a single list array. An accompanying link array specifies at which element in the list array the neighbor list for a given particle begins. Consider any particle j which is not on the neighbor list for particle i. Whenever sufficient time has passed for particle j to move inside the sphere of interaction for particle i the neighbor list must be updated The update is an order N^2 operation, but it need not be performed at each time step.

One method of deciding how many time steps should pass between updates is to use past experience and fix the update interval. For example, a common value of Δr_c is 0.3 for which 10 time steps is taken as an average update interval [28,27]. A more conservative method is to track the maximum velocity for all the particles in the system. This velocity is multiplied by the time step to give a maximum travel distance. These distances are summed for successive time steps and when this sum exceeds Δr_c, the list is updated.

The question of the magnitude of Δr_c is a matter of compromise. A large value of Δr_c permits longer intervals between updates, but the number of neighbors for each particle is larger resulting in more calculations per time step. A smaller value of Δr_c requires fewer calculations per time step but necessitates more frequent updating. A set of experiments were performed in the earlier stages of the simulation development to optimize r_c. A simple simulation was run to

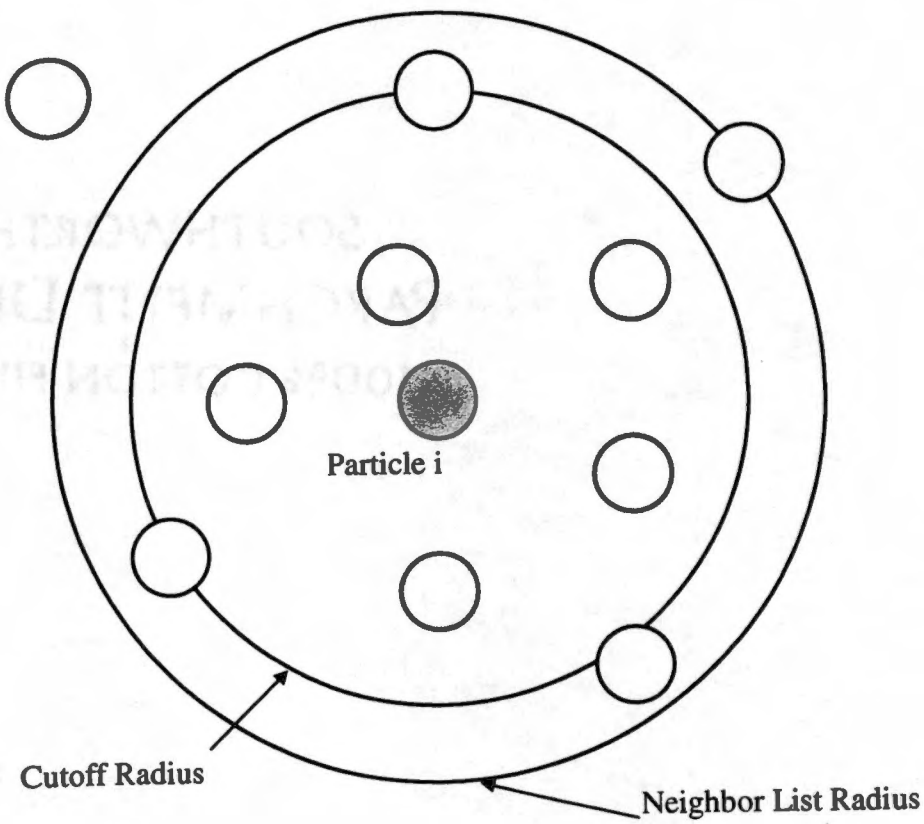

Figure 13. Schematic representation of the Neighbor List.

completion for various values of Δr_c ranging from 0.3 to 0.5. The simulation run with $\Delta r_c = 0.4$ resulted in the least overall run time although the variation was less than 4%.

A typical liquid simulation might have at least $N = 1000$ particles, with each one having approximately 40 neighbors. The neighbor list therefore would speed up the distance calculations by a factor of 25. In fact, using the values quoted above, the neighbor list update would require nearly 4 time longer than all of the distance calculations performed during the interval. As N gets larger, this disparity grows. The next question is whether or not there might be a way to optimize the neighbor list update. One affirmative answer to this question is through the use of cells.

The simulation volume can be broken up into an integral number of cells. When the time comes to update the neighbor list, each particle can be quickly assigned to a cell by examining its coordinates. If the cell width is larger than $\Delta r_c + r_c$ as shown in Figure 14, then any neighbors of a given particle i will lie within the cells immediately adjacent to the cell containing i. For a three-dimensional simulation only 26 cells would need to be examined for potential neighbors. If the simulation volume is large enough to contain more than 26 cells given the cell size constraint, then a savings is achieved. Taking into account the fact that, once r^*_{ij} is calculated then r^*_{ji} is also known, the number of adjacent cells can be reduced to 13. By comparison, simulations consisting of 4000 particles performed by the author contained over 100 cells. The use of cells thus resulted in a neighbor list update algorithm nearly 8 times faster.

A larger number of cells results in an increased savings. The number of cells is limited by the size of $r_c + \Delta r_c$. A compromise between this factor and the experiments mentioned earlier resulted in a choice of 0.3 for Δr_c. With this value

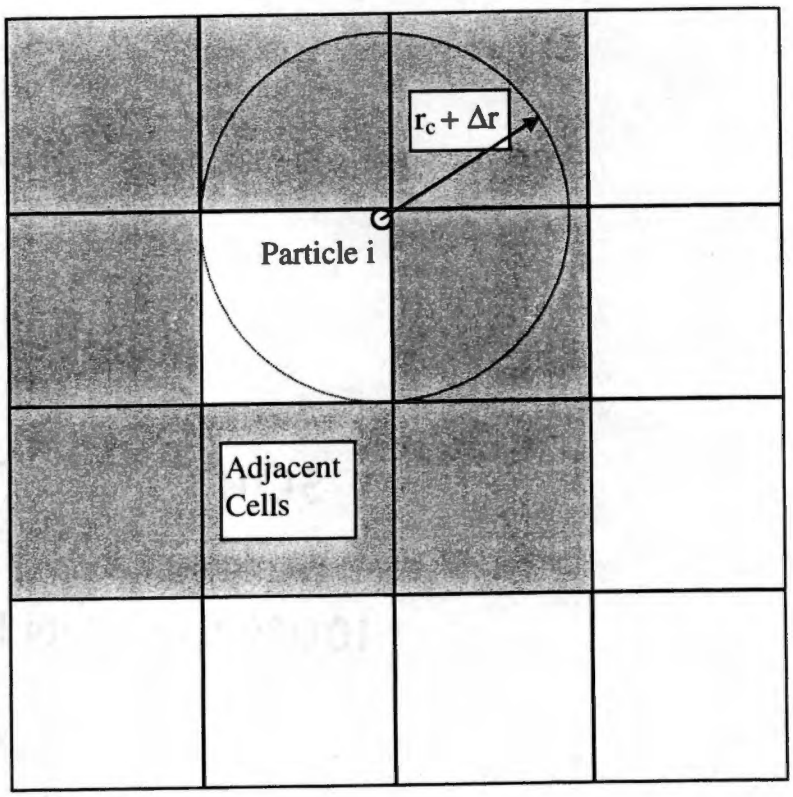

Figure 14. Division of the simulation volume into cells.

and using the conservative method discussed for calculating update intervals, the simulation averages 7 time steps between updates.

Although these methods may complicate the computer program somewhat, the savings they provide is definitely not trivial. A direct comparison utilizing the final versions of the simulation would be instructive, but impractical since these optimizations have been integral to the code since the early stages of development.

INTEGRATION

Once the forces have been calculated, the particles can be moved. This is done by moving a particle for the length of time specified by the time step based on the current velocity and acceleration. The exact form of this motion is given by the integration scheme chosen. Perhaps the simplest algorithm in common use is a basic finite difference algorithm, known as the Verlet algorithm [48]:

$$\begin{aligned} \mathbf{r}^*(t^* + \Delta t) &= 2\mathbf{r}^*(t^*) - \mathbf{r}^*(t^* - \Delta t) + \Delta t^2 \mathbf{a}^*(t^*) \\ \mathbf{v}^*(t^*) &= \frac{\mathbf{r}^*(t^* + \Delta t) - \mathbf{r}^*(t - \Delta t)}{2\Delta t} \end{aligned} \tag{4–11}$$

where $\mathbf{a}^*$ is the acceleration, $\frac{d^2\mathbf{r}^*}{dt^{*2}}$ given by equation (2-11).

As can be seen, the handling of the velocity is somewhat awkward, $\mathbf{v}^*(t^*)$ not becoming available until $\mathbf{r}^*(t^* + \Delta t^*)$ is calculated. There is also the numerically problematic addition of a small term, $\Delta t^2 \mathbf{a}^*(t^*)$ to the difference of the two much larger $\mathbf{r}^*$ terms. Since the velocity is a required component for many of the properties that will be calculated, it is perhaps advisable to improve upon this situation in the following manner:

$$\begin{aligned}
\mathbf{r}^*(t^* + \Delta t^*) &= \mathbf{r}^*(t^*) + \Delta t \mathbf{v}^*(t^* + \frac{1}{2}\Delta t^*) \\
\mathbf{v}^*(t^* + \Delta t^*) &= \mathbf{v}^*(t^* - \frac{1}{2}\Delta t^*) + \Delta t \mathbf{a}^*(t^*) \\
\mathbf{v}^*(t^*) &= \frac{1}{2}(\mathbf{v}^*(t^* + \frac{1}{2}\Delta t^*) + \mathbf{v}^*(t^* + \frac{1}{2}\Delta t^*))
\end{aligned} \tag{4–12}$$

This scheme is known as the leapfrog scheme due to the evaluations of the velocity at the half step. Whenever the velocities are required at the same time as the positions however, the third equation must be used. Although the precision has improved somewhat, the velocity evaluation could still be more elegant. A third version is the velocity-Verlet algorithm [26]:

$$\begin{aligned}
\mathbf{r}^*(t^* + \Delta t^*) &= \mathbf{r}^*(t^*) + \Delta t \mathbf{v}^*(t^*) + \frac{1}{2}\Delta t^{*2}\mathbf{a}^*(t^*) \\
\mathbf{v}^*(t^* + \Delta t^*) &= \mathbf{v}^*(t^*) + \frac{1}{2}\Delta t^*(\mathbf{a}^*(t^*) + \mathbf{a}^*(t^* + \Delta t^*))
\end{aligned} \tag{4–13}$$

These algorithms are all of the same theoretical order in accuracy. The difference between them is primarily a matter of the practicality of their numerical implementation. No attempt to use the previously obtained information, whether through old values or through higher derivatives, is made. If a higher order scheme is desired, then predictor-corrector (P-C) methods should be used. Various orders of P-C methods are available; the fifth order Gear method will be presented here [49].

First a prediction is made for each of the values based on the current values and higher derivatives:

$$
\begin{aligned}
\mathbf{r}^*(t^*+p^*) &= \mathbf{r}^*(t^*) + \Delta t^*\mathbf{v}^*(t^*) + \frac{\Delta t^{*2}}{2}\mathbf{a}^*(t^*) \\
&\quad + \frac{\Delta t^{*3}}{6}\mathbf{b}^*(t^*) + \frac{\Delta t^{*4}}{24}\mathbf{c}^*(t^*) + \frac{\Delta t^{*5}}{120}\mathbf{d}^*(t^*) \\
\mathbf{v}^*(t^*+p^*) &= \mathbf{v}^*(t^*) + \Delta t^*\mathbf{a}^*(t^*) + \frac{\Delta t^{*2}}{2}\mathbf{b}^*(t^*) + \frac{\Delta t^{*3}}{6}\mathbf{c}^*(t^*) + \frac{\Delta t^{*4}}{24}\mathbf{d}^*(t^*) \\
\mathbf{a}^*(t^*+p^*) &= \mathbf{a}^*(t^*) + \Delta t^*\mathbf{b}^*(t^*) + \frac{\Delta t^{*2}}{2}\mathbf{c}^*(t^*) + \frac{\Delta t^{*3}}{6}\mathbf{d}^*(t^*) \\
\mathbf{b}^*(t^*+p^*) &= \mathbf{b}^*(t^*) + \Delta t^*\mathbf{c}^*(t^*) + \frac{\Delta t^{*2}}{2}\mathbf{d}^*(t^*) \\
\mathbf{c}^*(t^*+p^*) &= \mathbf{c}^*(t^*) + \Delta t^*\mathbf{d}^*(t^*) \\
\mathbf{d}^*(t^*+p^*) &= \mathbf{d}^*(t^*)
\end{aligned}
\tag{4–14}
$$

where p^* is used as a time step placeholder to indicate that a further correction is needed before the time step is complete, and b^*, c^* and d^* are the third, fourth and fifth order derivatives respectively. The predicted positions are used to calculate the forces, $\mathbf{F}^*(t^*+\Delta t^*)$, which are transformed into the accelerations, $\mathbf{a}^*(t^*+\Delta t^*)$, using equation (2-11). This value of the acceleration is then assumed to be the correct value and is used to determine the correction factor:

$$
\Delta\mathbf{a}^* = \mathbf{a}^*(t^*+\Delta t^*) - \mathbf{a}^*(t^*+p^*) \tag{4–15}
$$

This correction factor is now used to correct the other values:

$$
\begin{aligned}
\mathbf{r}^*(t^*+\Delta t^*) &= \mathbf{r}(t^*+p^*) + k_0\Delta\mathbf{a}^* \\
\mathbf{v}^*(t^*+\Delta t^*) &= \mathbf{v}^*(t^*+p^*) + k_1\Delta\mathbf{a}^* \\
\mathbf{b}^*(t^*+\Delta t^*) &= \mathbf{b}^*(t^*+p^*) + k_3\Delta\mathbf{a}^* \\
\mathbf{c}^*(t^*+\Delta t^*) &= \mathbf{c}^*(t^*+p^*) + k_4\Delta\mathbf{a}^* \\
\mathbf{d}^*(t^*+\Delta t^*) &= \mathbf{d}^*(t^*+p^*) + k_5\Delta\mathbf{a}^*
\end{aligned}
\tag{4–16}
$$

The coefficients k_i are determined based on the order of the P-C scheme used. For the fifth order Gear P-C method for second order equations, the values of the k_i are:

$$k_0 = \frac{3}{16} \quad k_1 = \frac{251}{360} \quad k_3 = \frac{11}{18} \quad k_4 = \frac{1}{6} \quad k_5 = \frac{1}{60} \tag{4–17}$$

This corrector can be applied more than once in order to increase the accuracy of the result and permit a longer time step. Unfortunately, this requires a second evaluation of the forces and all of the computation that entails. A graphical examination of the typical L-J (12-6) potential in Figure 12 reveals that the potential varies quite rapidly with the separation distance, placing an inherent limit on the time step size as well. Since up to 80% of the run time is used to calculate the force, it is often more efficient to increase accuracy by reducing the time step than by performing another force calculation. Similar difficulties apply to using even higher order methods, such as Runge-Kutta, which require more than one force evaluation.

Even after rejecting multiple evaluation methods, there is still a choice of algorithm to be made. The decision is largely a matter of accuracy versus efficiency, although practicality will play a part as well. The previous discussion on phase space revealed that the trajectory traced as the MD simulation advances in time will yield property averages equivalent to a random distribution. This phase space trajectory is highly nonlinear. If two similar simulations are initiated which differ only in the position of one particle, it will not be long before none of the particle positions or velocities will match. Yet as long as they maintain constant energy, they will both remain on the same hyper-surface in phase space and will thus yield statistically equivalent results. Since the motion of the particles at each instant is only approximated, the system departs from the initial system quickly. There is

therefore no question of accuracy as far as the initial trajectory goes; any accuracy is impossible for more than a few time steps.

The more relevant issue is the invariance of the energy. The accuracy with which the initial trajectory is continued is not important as long as it stays on the initial hyper-surface. Higher order schemes in general maintain constant energy somewhat better than lower order schemes for the same time step [26]. All methods use some method of correcting the energy drift that occurs due to roundoff error. Many simulations use the leap-frog and velocity Verlet methods due to their simplicity and time reversibility [39,50]. Others use the P-C methods for their higher accuracy [41,51]. There is still not a general advantage to one family of algorithms over the other. The choice often comes down to the suitability of the algorithm for the particular application and personal preference.

In the case of the simulations performed for this work, a fifth order P-C method was chosen. This decision was made largely due to its slightly higher accuracy and the convenient form in which the velocity appears for use. Its application to NEMD and rigid body molecules is quite straightforward as well.

BOUNDARY CONDITIONS

With the particles in place and the integration method ready to begin, the next step is to consider the boundary conditions. In the large system of 10^{23} particles, a comparatively negligible fraction of the particles interact with or are influenced by the wall. The same does not hold with the smaller numbers of the MD simulation. For a cubic volume of 1000 particles, 488 or nearly 50% of the particles are in the layer immediately adjacent to the boundary. Compare this with 10^{17} particles or 0.0001% immediately adjacent to the boundary for the large

system. Clearly the implementation of the boundary conditions has a profound effect on the results.

A simple yet elegant solution is to employ what are known as periodic boundary conditions (PBCs). These conditions result from the assumption that what is happening within the simulation volume under investigation is statistically equal to what is occurring in the surrounding volumes. Indeed, this is the basic assumption behind MD simulations. PBCs take this a step further by requiring that all the surrounding volumes be exact copies of the volume under consideration. In other words, space is filled with an infinite number of exactly similar volumes.

In practical terms, the use of PBCs means that any time a particle leaves the simulation volume from one face, the particle (or a copy of it, it makes no difference) immediately re-enters through the opposing face. PBCs can be applied to any shape that tessellates the space, but cubic or rectangular volumes simplify the formulation. This discussion is primarily focused on 3-D systems, but similar principles hold for 2-D and 1-D systems. Figure 15 presents a 2-D example of PBCs.

The force computations are also affected by the use of PBCs through the neighbor list. If a given particle is close to the edge of the simulation boundary, a second particle the length of the simulation region away may be considered to be a neighbor because its periodic image may lie within the cutoff radius. This requires that the cells that are used to reduce the neighbor update calculations must be considered to be periodic as well.

In general, PBCs are employed using the following form:

$$r^*_{ij\,x} = \begin{cases} r^*_{ij\,x} + l_x, & r^*_{ij\,x} < -\frac{l_x}{2} \\ r^*_{ij\,x}, & |r^*_{ij\,x}| \leq \frac{l_x}{2} \\ r^*_{ij\,x} - l_x, & r^*_{ij\,x} > \frac{l_x}{2} \end{cases} \tag{4–18}$$

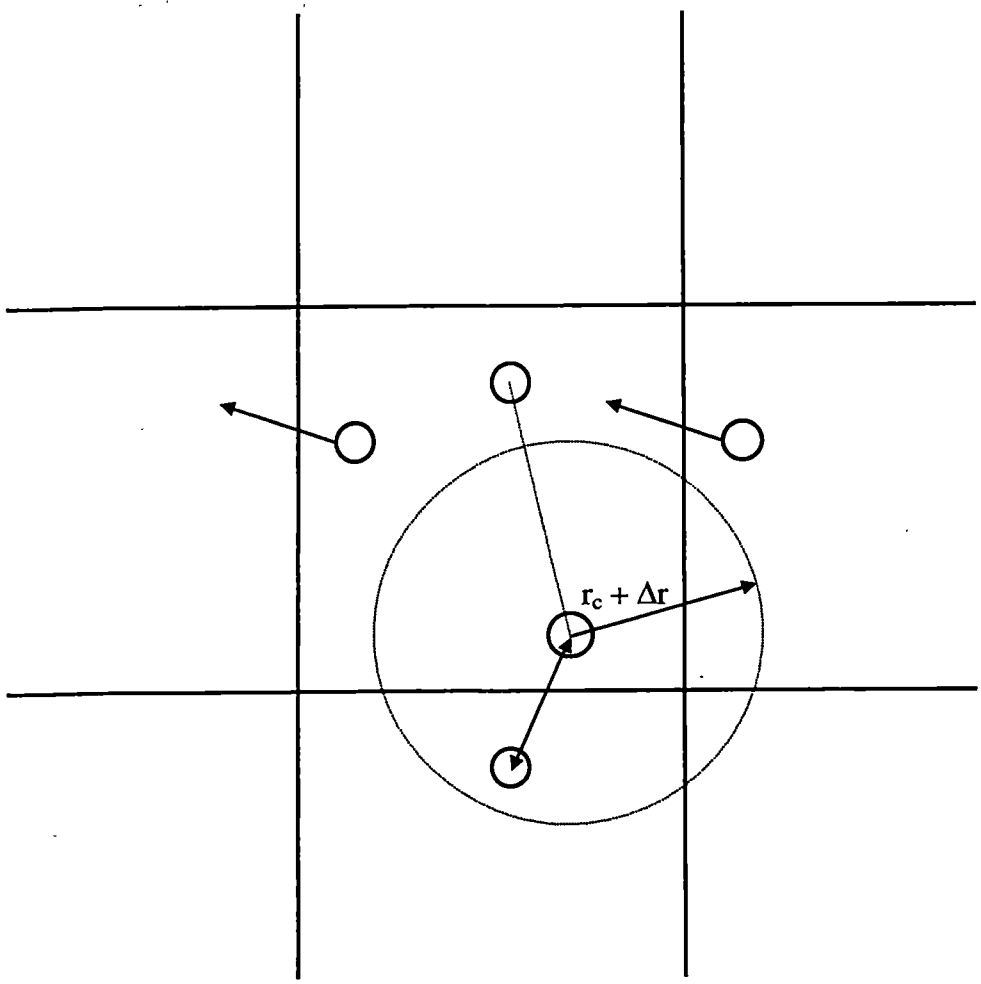

Figure 15. Two-dimensional periodic boundary conditions.

where l_x is the length of the simulation volume in the x direction and similar expression hold for the y and z directions.

The use of PBCs has various consequences. First, any phenomena with minimum length scales larger then the simulation volume will not be seen. This includes any kind of long wavelength disturbances. Second, any anomalous disturbances created within the volume will be reintroduced, allowing for the possibility of resonance. Nevertheless, these are minor obstacles and PBCs are widely used under conditions of constant volume, constant particle number simulations.

The other major class of boundary conditions used in these kinds of simulations are wall boundaries. In the PBCs, opposing sides of the volume are paired together inasmuch as particles leaving through one will enter through the other. In much the same way, wall boundary conditions are also found in pairs. The two types can be mixed together as long as opposing faces are of the same kind. A clear example of this is the channel flow that will be simulated. The top and bottom faces of the channel are walls while PBCs are utilized for the other faces.

Various types of walls are available and some of these are presented in Figure 16. A simple wall model would be to consider the wall as a single flat surface. Particles are then made to reflect specularly to model the flat surface. This is not very physically accurate since the simulation is being performed at a molecular scale and no wall is flat at that scale. A diffuse wall can be simulated by reflecting the particle in a random direction with a certain velocity magnitude. This type of wall is common in low density simulations.

A third type of simple wall can be modeled by considering the wall to be a potential sheet. The wall would act on all particles nearby with a given potential such as the Lennard-Jones. The separation distance used in the calculation would always be considered to be along the vector normal to the wall.

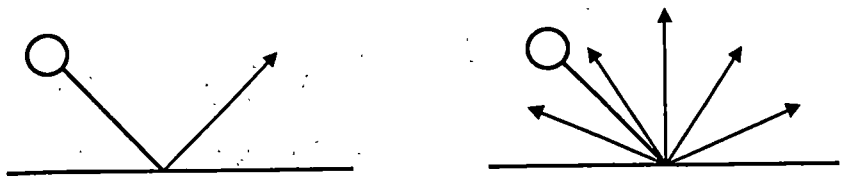

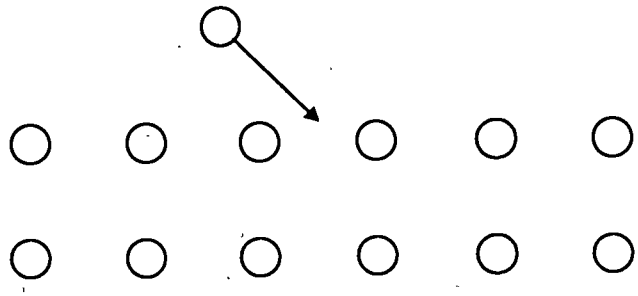

Figure 16. Various types of walls used in MD simulations.

When the interaction between the fluid and the wall requires more detailed investigation, as is the case in this study, the wall can also be modeled as a collection of particles. The type of walls used in this simulation consist of two layers of atoms arranged in a FCC crystal lattice which is demonstrated in Figure 17. These particles also act on the fluid particles with a Lennard-Jones potential.

The wall particles must be kept in place somehow, to maintain their solidity, otherwise the walls would "melt" into the fluid. This is most commonly done by attaching the wall particles to a fixed point in space by a spring [46]. The particles may vibrate about a fixed position, but on the average they would be considered stationary. A more complex model would be to attach all the wall particles together with springs and arrange for the entire structure to be fixed on average.

In the current simulation a somewhat simpler model is used. The wall particles simply do not respond to the forces that may act on them; they are held fixed. This is equivalent to the single spring model where the spring constant is infinite. This particular model does not allow the walls to participate in maintaining constant temperature, but that will be taken care of later. This model does reduce the computational requirements allowing additional resources to be directed toward effects that are more central to the main hypothesis. It also reduces the number of variables to be considered when examining the effects of the wall on the flow.

Since the boundaries are not periodic, it is important that no particles be allowed to escape. This may sound trivial, but in fact testing for molecules which escape through the wall can be a good indication of a problem. For example, the wall may not be dense enough. This is especially important when fluid molecules are added since the fluid and wall particles may be very dissimilar. Escaping particles can also be a good indication that the time step is too large. If the

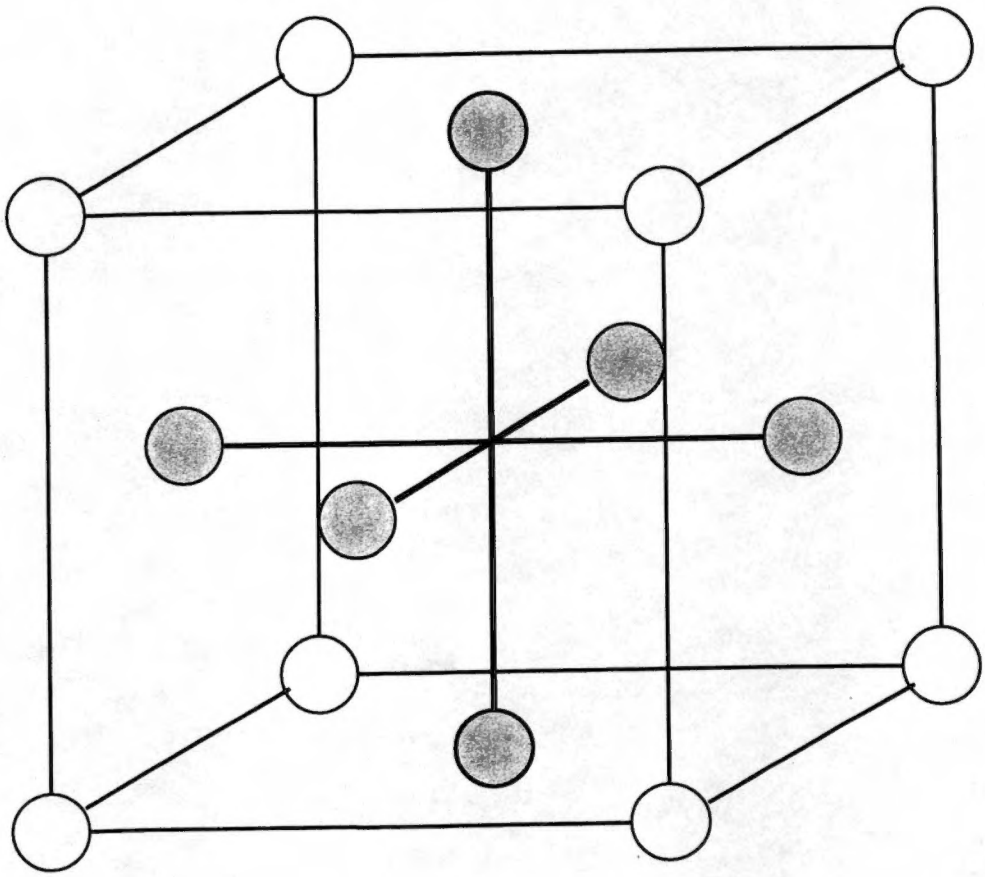

Figure 17. A schematic representation of a face-centered cubic crystal cell.

velocity is too high, a large time step can allow the particle to pass through the wall before the wall particles have an opportunity to repel it.

The wall is also considered to be periodic in its dimensions. It has to be for all the periodic images of the fluid box to remain the same. This means that the number of particles in each direction must have an integral value. Though it may seem like a small point, it should be noted that the wall and the fluid along with their respective densities cannot be established independently. This fact will become important when the effect of the wall density is considered. Integral changes, and relatively large ones, must be made, limiting the resolution of the analysis.

INITIAL CONDITIONS AND EQUILIBRATION

An MD simulation seeks to follow a system as it traces a hyper-surface in phase space. This places two requirements on the initial configuration: the system needs to begin its trajectory on the hyper-surface, and the system needs to be in a state of relative equilibrium. Requiring equilibrium serves to reduce the dependence of the final results on the arbitrary initial conditions. The first condition can be met by a suitable configuration of random positions and velocities with a Maxwellian distribution. It is difficult, however, to ensure that such a random configuration is in equilibrium.

The common way of circumventing the second problem is to take an arbitrary initial condition and let the simulation run anywhere from a few thousand to a million time steps. In this way the system will presumably establish equilibrium on its own. During this equilibration phase, the temperature and energy can be adjusted at will since the desired properties are not yet being calculated. Once the equilibration phase is complete and the system is in equilibrium with the desired

energy or temperature, then the production phase can begin. This is the portion of the simulation during which all the necessary values are calculated and stored.

The equilibration phase allows the use of fairly simple initial conditions. A very common method is to arrange all of the fluid particles in the FCC lattice structure. For monatomic particles, this alleviates any concerns that two particles may overlap. Numerically, overlap means that the points representing the particles are so close that the repulsive force is extremely large and the following time step would find them both outside of the simulation volume. The FCC lattice also provides for a uniform density distribution. The size of the FCC lattice unit which determines the separation of the particles depends upon the given density.

The FCC lattice unit contains four particles. Generally this is determined by summing the fractional pieces at the vertices and the faces. For simulation purposes however, these four particles will be considered to lie at the bottom front left vertex and in the middle of the three faces meeting at this vertex. The other particle sites are filled by particles in adjacent lattice units. For periodic boundary conditions, an integral number of lattice units must be used to allow for the periodic images. The number of particles in the simulation is then $4\ell mn$ where ℓ, m, n are the number of lattice units in the x, y, z directions. If the simulation volume is cubic then the number of particles is $4n^3$ which is why early simulations often had a number of particles such as $32, 108, 256, 500, 864$ and so on.

Since the separations are uniform there must be a mechanism for initiating the random motion in the system. In the case of the FCC lattice distribution, this is accomplished through the initial velocities that are specified for each particle. The direction of the velocity vector is assigned a random value. The magnitude of the velocity vector is determined based on the given temperature. The magnitudes may also be assigned randomly and then scaled to give a Maxwellian distribution at

the given temperature. It is somewhat easier to assign the same velocity magnitude to each particle, although this may require a slightly longer equilibration phase as the system moves toward a Maxwellian distribution on its own. The latter is the method used in the current study.

For the equal velocity magnitude method, the value of the magnitude, v_0, is given by:

$$v_0 = \left[3(1 - \frac{1}{N})T_0\right] \tag{4–19}$$

where T_0 is the given initial temperature.

The fifth order P-C method used requires initial values for all the higher derivatives as well. The value for the acceleration will be determined in the first force calculation step. The higher derivatives are set to zero initially. Although this simplification may result in reduced accuracy for the first few steps, by the end of the equilibration phase this effect will have disappeared.

The number of time steps required to reach equilibration is for the most part a matter of experience. There is not a clearly defined point during the run at which it can be stated that equilibrium has been reached. It is rather a matter of checking various characteristics of the system to determine if the system has been satisfactorily equilibrated. For example, each velocity component of the system should describe a Maxwellian distribution. This is most conveniently tracked using the Boltzmann H-function [27]. The H-function is at a minimum when the distribution is Maxwellian. Thermodynamic properties should fluctuate about a stable average value at equilibrium. When the FCC lattice is used initially, an order parameter can be evaluated to determine whether the crystal structure has

melted sufficiently. If the equilibration phase is broken into two portions then the values averaged over each portion should be very close.

None of the checks discussed are guarantees of equilibrium. In practice it is often the case that the investigator will run the equilibration phase for a fixed number of time steps [39,41]. The number chosen is based on personal experience or on the work of others in the field. Typical values range from 50,000 to half a million time steps. To alleviate concerns that a new simulation may introduce unknown phenomena delaying equilibrium, multiple simulations with identical parameters but different initial configurations can be performed. If the averaged values for the simulations compare favorably then it is reasonable to consider the system in equilibrium. This is the method used in the current study with 100,000 time steps denoting the end of the equilibration phases. When multiple simulations were performed, the results were statistically equivalent.

THERMODYNAMIC PROPERTIES

With the initial conditions specified, the simulation is ready to run. This section discusses some of the thermodynamic properties that can be calculated during the simulation run.

One of the most basic properties is the density. Although perhaps simple in concept, the bulk density can be difficult to calculate exactly. The density is calculated according to:

$$\rho^* = \frac{N_f}{V^*}$$

where ρ^* is the density and V^* is the volume. The volume requires more discussion. To be accurate the volume should characterize the amount of space available to the particles. A typical density distribution shows, however, that there are small

zones very near the wall where few if any fluid particles will be found. This region should theoretically be excluded from the volume. The size of this region is not well-defined and for a fixed channel width it will change depending on the initially specified density.

Different conventions are used to resolve this dilemma and evaluate a figure for the density. Often, the initial density used to determine the size of the FCC lattice units is assumed to persist throughout the simulation [35]. Another method is to use the distance between the centers of mass of the innermost wall layers in calculating the volume [47]. In this study the density is used primarily to compare between different runs and so its absolute value is not as critical. The density is calculated using the third method to provide a clear and consistent definition. If a more accurate density is required then the density profile can be used to obtain the region between the walls to which the system has access [41].

Another property already mentioned is the temperature. There are three different types of temperature that may be encountered. The first is a specified value such as T_0 that is fixed over the course of the simulation. The second is the instantaneous temperature, $T^*(t^*)$, computed from the instantaneous kinetic energy, $E_k^*(t^*)$ of the system of particles:

$$E_k^*(t^*) = \frac{1}{2}\sum_{i=1}^{N_f} v_i^{*2} \qquad T^*(t^*) = \frac{2}{3N_f} E_k^*(t^*) \tag{4–20}$$

The third type of temperature, the time average temperature $\langle T^* \rangle$ is computed using an average kinetic energy $\langle E_k^* \rangle$:

$$\langle E_k^* \rangle = \frac{1}{t_c}\sum_{\tau=0}^{t_c} E_k^*(\tau \Delta t^*) \qquad \langle T^* \rangle = \frac{2}{3N_f} \langle E_k^* \rangle \tag{4–21}$$

where t_c is the current time step. The brackets $\langle\ \rangle$ will apply to any property that has been time averaged in this manner. It should be noted that time averages are not very accurate unless t_c is large, i.e. $50,000$ or more.

Another property monitored in this simulation is the potential energy. During the force calculation at each time step, the potential energy is also calculated since many of the necessary evaluations have already been performed to find the force. The Lennard-Jones equation (4-4) is used and the contributions from each interaction pair are summed. The average potential energy is then given by:

$$\langle U^* \rangle = \frac{1}{t_c} \sum_{\tau=0}^{t_c} \sum_{i=1}^{N} \sum_{\substack{j=1 \\ j \neq i}}^{N} u^*(r_{ij}^*, \tau \Delta t^*) + U_{LR} \tag{4-22}$$

where U_{LR} is the long range correction factor required because of the potential truncation:

$$U_{LR} = \frac{-8\pi\rho^*}{3r_c^3} \tag{4-23}$$

Note that this correction is only as accurate as the density value. The average pressure, $\langle P^* \rangle$, is calculated using the virial equation of state following the development in Haile [27]. It is given by:

$$\langle P^* \rangle = \rho^* \langle T^* \rangle \left(1 + \frac{1}{3N_f \langle T^* \rangle} \left\langle \sum_{i=1}^{N_f} \sum_{\substack{j=1 \\ j \neq i}}^{N_t} r_{ij} F_{ij} \right\rangle + P_{LR} \right) \tag{4-24}$$

where the long range pressure correction is given by:

$$P_{LR} = \frac{-16\pi\rho^*}{3\langle T^* \rangle r_c^3} \tag{4-25}$$

The shear viscosity, η^*_{xy}, is calculated using the microscopic stress tensor for each particle, $\mathbf{J}^*_\mathbf{i}$, whose elements are given by:

$$J^*_{i\,\alpha\beta} = m^* \sum_{i=1}^{N_f} v_{i\,\alpha} v_{i\,\beta} + \frac{1}{2} \sum_{\substack{j=1 \\ j \neq i}}^{N_t} r_{ij\,\beta} F_{ij\,\alpha} \tag{4–26}$$

where α and β are indexes over the coordinate directions, x, y, z. The shear viscosity is then given by:

$$\eta^*_{xy} = \frac{1}{V^* \langle T^* \rangle} \int_0^{t_\infty} \langle J^*_{xy}(t^*) J^*_{xy}(0) \rangle dt \tag{4–27}$$

where the J^*_{xy} are averages over all the $J^*_{i\,xy}$. The integration is done numerically. Clearly the integration cannot be taken to infinity. In fact, the upper limit must be shorter than the length of the simulation in order to get a reasonable value for the time average inside the integral. Much longer simulations are required to obtain accurate viscosity values. Evaluation of the stress tensor components must also be performed during the force calculation and therefor adds significantly to the CPU time required.

Many other thermodynamic quantities can be obtained, but these are the only ones calculated for the current study. These expressions apply for simulations with constant energy (NVE ensemble). A small correction of order $\frac{1}{N_f}$ is required for the potential and kinetic energy as well as the temperature if the simulation is performed with constant temperature (NVT ensemble). The expressions for the pressure and shear viscosity are for equilibrium conditions and so they will not be computed for the channel flows.

CHANNEL FLOW

A final concern regarding the implementation of the monatomic particle simulation are the details of the channel flow. As mentioned in Chapter 2, there are two types of flows that will be considered: plane Poiseuille or pressure driven flow, and plane Couette or flow driven by wall motion.

The pressure gradient in the plane Poiseuille flow is approximated by applying a body force to each particle at each time step. This force is applied in the direction of the flow, parallel to the walls, after the interaction forces have been computed:

$$\mathbf{F}_i^* = \sum_{\substack{j=1 \\ j \neq i}}^{N_t} \sum_{\alpha=1}^{S_i} \sum_{\beta=1}^{S_j} \mathbf{F}_{ij\alpha\beta}^* + g\mathbf{i} \tag{4–28}$$

where g is the magnitude of the body force and $\mathbf{i}$ is the unit vector in the x-direction. The value of g used in the current simulation is 0.05. This value is one that is commonly used and provides a nice compromise between stability and quick flow development. A schematic representation of plane Poiseuille flow is given in Figure 18.

The plane Couette flow is generated by moving the wall particles by a designated amount. This amount is determined by the desired wall velocity, V_w. It is common to move the upper and lower walls with the same speed but in opposing directions. The movement of the wall particles is accomplished at the same time as the predictor step. For simplicity the wall velocity is taken to be 1.0, again a commonly used value. Figure 19 demonstrates the plane Couette flow.

The flow generation brings energy into the fluid. If the energy is not removed by some mechanism, then the temperature will steadily increase. Chapter 3 discussed some of the different methods that are used. The current study utilizes the method of constraint dynamics to preserve the temperature.

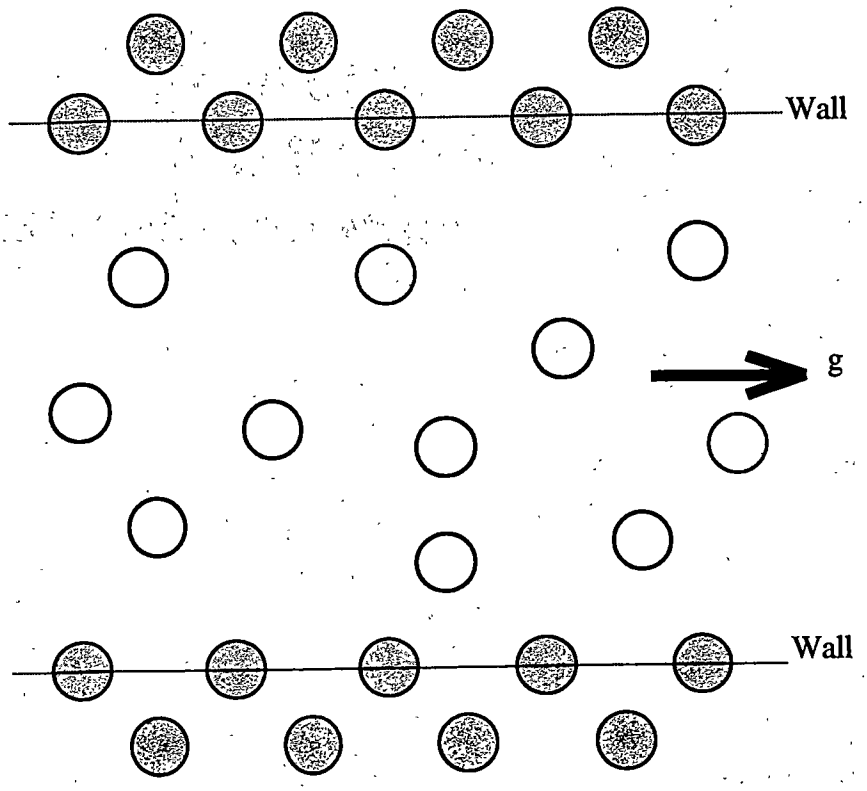

Figure 18. Schematic representation of plane Poiseuille flow.

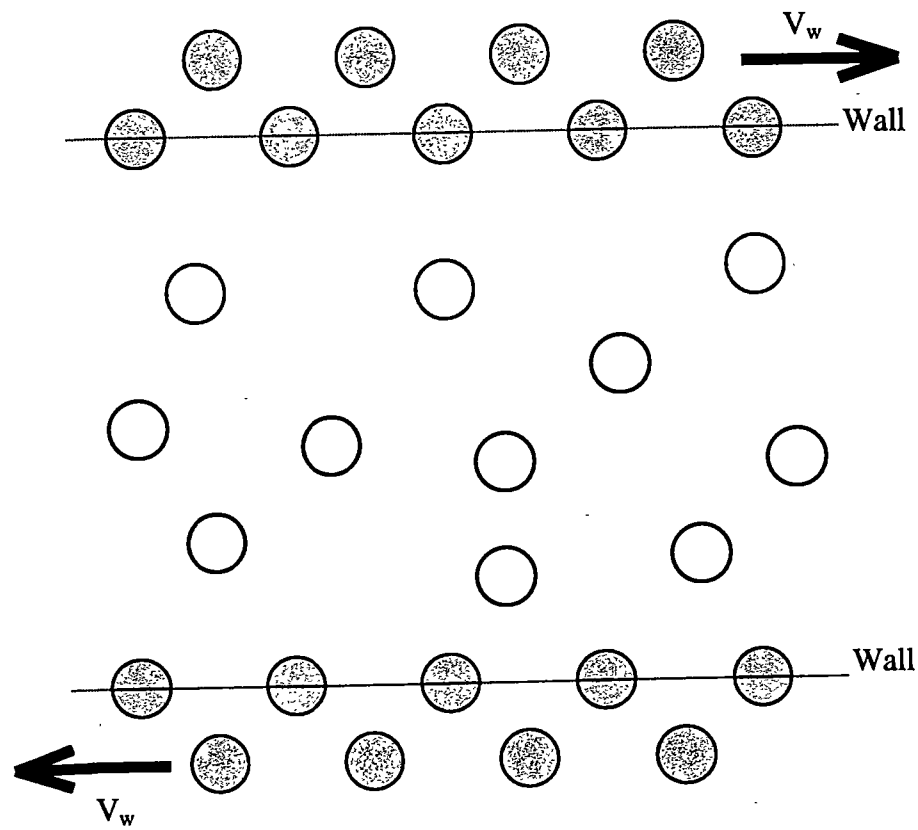

Figure 19. Schematic representation of plane Couette flow.

Maintaining a constant temperature, T_0, is equivalent to specifying a constant kinetic energy:

$$\frac{1}{2}\sum_{i=1}^{N_f} v_i^{*2} = \frac{3N_f}{2}T_0 \tag{4–29}$$

Differentiating with respect to time yields:

$$\sum_{i=1}^{N} \mathbf{a}_i^* \cdot \mathbf{v}_i^* = 0 \tag{4–30}$$

In order to employ the method of constraints a constraint parameter λ must be included in the equation for the $\mathbf{a}_i^*$:

$$\mathbf{a}_i^* = \frac{1}{m^*}\mathbf{F}_i^* + \lambda \mathbf{v}_i^* \tag{4–31}$$

Inserting this equation for $\mathbf{a}_i^*$ into (4-30) and solving for λ yields:

$$\lambda = -\frac{\sum_{i=1}^{N_f} \mathbf{v}_i^* \cdot \mathbf{F}_i^*}{m^* \sum_{i=1}^{N_f} \mathbf{v}_i^* \cdot \mathbf{v}_i^*} \tag{4–32}$$

The constraint parameter λ is calculated at each time step after the force calculation is complete. It is then used to modify the acceleration according to equation (4-31) above. The same value of λ is used to modify the motion of all the particles. Since λ is a coefficient of the velocity in the equation of motion it is comparable to a viscous damping term. That expresses well what this factor accomplishes. The velocities are reduced by an amount which counteracts the input of energy caused by driving the flow.

This method modifies the velocities of each particle in the fluid which means that it does not coincide with the more intuitive concept of the temperature control being performed at the wall. The choice was a simplification made to reduce the

complexity of the program and to remove another variable which may have clouded the phenomenon under investigation. The use of this method effectively changes the potential being used. Nevertheless, Haile and Gupta [44] show that this does not affect the configurational properties of the system.

The method of constraints is used to keep the temperature from changing, a numerical device known as a thermostat. Numerical error keeps this process from maintaining the temperature exactly, however. At the next step the thermostat will try and maintain the current temperature which is slightly different than the previous temperature due to the error. This propagation of error continues at each step. If these errors do not cancel exactly then over time the system average temperature will gradually change. It has been verified experimentally that the temperature does indeed rise even when the thermostat is in use. For this reason the constraint thermostat is often accompanied by the simpler scaling method every thousand time steps or more.

The scaling method simply scales the velocities of every particle to bring the temperature back to the specified temperature:

$$v^*_{i\,new} = v^*_{i\,old}\sqrt{\frac{T_0}{\langle T^* \rangle}} \tag{4–33}$$

where $\langle T^* \rangle$ is given by (4-21). With this final algorithm in place, simulation runs can be made for monatomic particles. These runs do not yet provide insight concerning molecular orientation. They do promote confidence in the simulation procedures by producing the expected density and velocity profiles for the two different flow types.

CHAPTER 5: IMPLEMENTATION - MOLECULES

The molecular dynamics simulation of atoms in a channel flow has been developed to this point. Although the simulation of the rod-like molecules will require modifications of each of the topics discussed, the principles are the same and the changes should be straightforward.

The concept of phase space still applies in the case of a molecular system. In general, three additional degrees of freedom for the orientation and three for the angular velocity are required. This brings the total to $12N_f$. For the rod-like molecules, the equations can be simplified so that there are only two additional degrees of freedom for both the orientation and the velocity. When this study began, the intent was to make the program general enough to include all types of molecules so these simplified forms are not used and the $12N_f$ degrees of freedom hold.

STRUCTURE

Although complicated molecules were allowed for, it later became apparent that they were beyond the scope of this study. The molecules used will therefore be considered to be linear. This means that all the atoms or sites pertaining to the molecule lie on a single axis. For two sites this is trivial, but for three or more sites this does select a specific configuration from those that are possible. In this study molecules of two, three, and four sites were investigated.

The second factor governing the size of the molecule is the separation between sites on the molecule. For the two-site molecule various separations were used including $0.5, 1.0$, and 1.5 in the non-dimensionalized units. The 0.5 spacing was used on the three and four site molecules in order to compare the results with previous molecular simulations.

When highly complex molecules are simulated much time is spent adjusting the potentials of each of the sites to model the molecule accurately. For example, some sites may have a deeper attractive well while others are charged and require electrostatic interactions. The intramolecular bonds between atoms must also be accounted for. The molecules in the current investigation consisted of sites which were all characterized by the same Lennard-Jones potential used for the atoms. The atoms within the molecule are rigidly fixed to each other eliminating the need to calculate intramolecular bonds. These decisions were made based on simplicity as well as to prevent any ionic interactions from masking the effect of the shear on the molecules.

The translational and rotational motions of the molecules are dealt with separately. The rotation will be considered later. The translational motions of the molecules are calculated in the same way as for the monatomic particles except that the coordinates of the center of mass are used. The same integration method is used with the coordinates $\mathbf{r}_i^*$ replaced by the coordinates of the center of mass, $\bar{\mathbf{r}}_i^*$. All the derivatives also apply to the center of mass. For plane Poiseuille flow, the body force $g\mathbf{i}$ is applied to the center of mass of each molecule.

The walls are made up of atoms which are fixed for plane Poiseuille flow and move at constant velocity for plane Couette flow. The walls can be made of more complicated molecules but there was no compelling reason to do so for this study. Using atoms for the walls also simplifies the task of changing the wall density since there is no concern over molecule orientation and overlap in the wall.

FORCE AND MOMENT CALCULATION

The interactions between each molecule are a combination of the interactions between all pairs of sites pertaining to the two molecules. If molecule i has S_i sites and molecule j has S_j sites, then the force on molecule i is given by:

$$\mathbf{F}_i^* = \sum_{\substack{j=1 \\ j \neq i}}^{N_t} \sum_{\alpha=1}^{S_i} \sum_{\beta=1}^{S_j} \mathbf{F}_{ij\alpha\beta}^* \tag{5-1}$$

where again $\mathbf{F}_{ij\alpha\beta}$ is given by the Lennard-Jones differential and the distance is $r_{ij\alpha\beta}^*$, the distance between the sites on the two molecules. This distance is simply a vector sum involving the distance between the centers of mass, $\bar{\mathbf{r}}_{ij}^*$, and the distance from the center of mass of the molecule to the site α, $\Delta\mathbf{r}_{i\alpha}^*$:

$$r_{ij\alpha\beta}^* = -\Delta\mathbf{r}_{j\beta}^* + \bar{\mathbf{r}}_{ij}^* + \Delta\mathbf{r}_{i\alpha}^* \tag{5-2}$$

A schematic representation of the molecular interaction is given in Figure 20. The site vectors $\Delta\mathbf{r}_{i\alpha}^*$ depend on the orientation of the molecule. The next section on rotation provides more details concerning their calculation. The site to site distance $r_{ij\alpha\beta}^*$ is used in equation (4-9):

$$F_{ij\alpha\beta}^* = \begin{cases} \frac{-48}{r_{ij\alpha\beta}^{*2}} \left[\left(\frac{1}{r_{ij\alpha\beta}^*} \right)^{12} - \frac{1}{2} \left(\frac{1}{r_{ij\alpha\beta}^*} \right)^{6} \right], & r_{ij\alpha\beta}^* \leq r_c \\ 0, & r_{ij\alpha\beta}^* > r_c \end{cases} \tag{4-9}$$

Mathematically the first summation runs through all the molecules $j \neq i$. As mentioned in Chapter 4, this is reduced substantially in the implementation through the use of neighbor lists and cells. It is common practice to use the distance between the centers of mass, $\bar{\mathbf{r}}_{ij}^*$ when determining whether molecule j should be considered a neighbor of molecule i. This reduces the number of distance calculations when updating the neighbor list. It also prevents partial interactions,

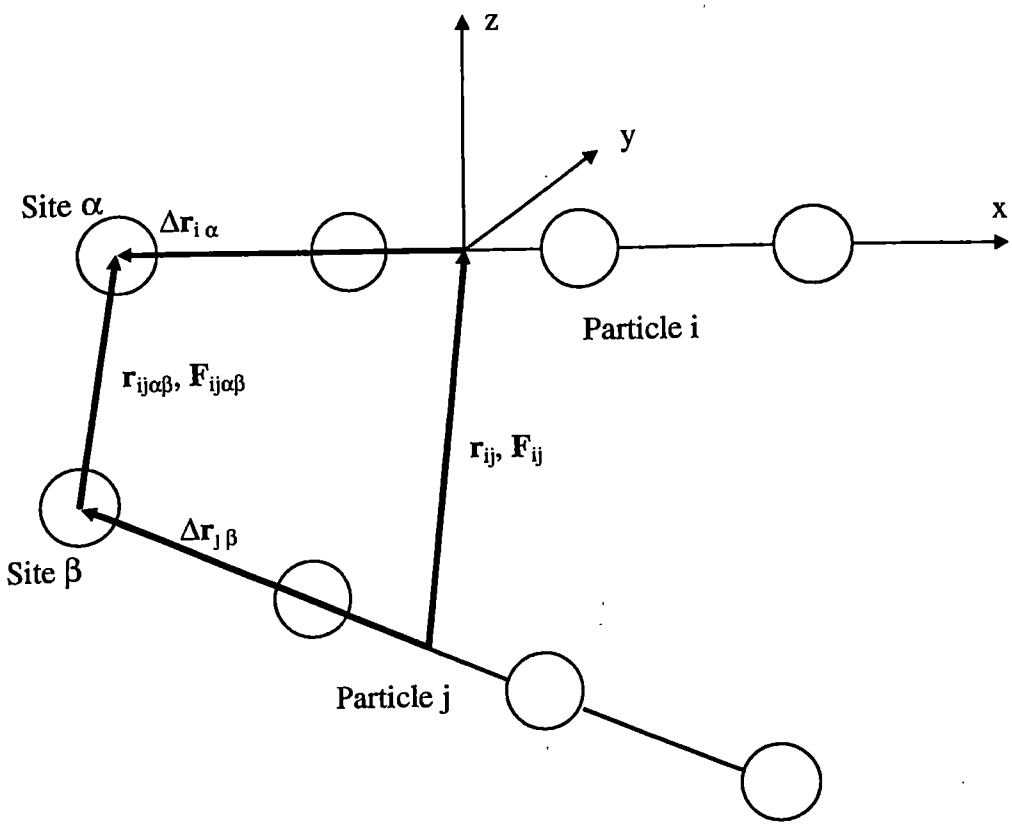

Figure 20. Schematic representation of the interaction between two molecules.

i.e., a situation in which some of the sites on molecule j would be included in the interaction while the rest would be truncated. If $\bar{\mathbf{r}}^*_{ij} < r_c$ then all the sites on molecule j are included in the interaction regardless of their relation to r_c.

The use of PBCs eliminates situations where a part of the molecule might lie outside the simulation volume. If a portion of a molecule does happen to extend past the periodic boundary, it will enter through the opposite side in the form of an image of the same molecule. Not only is N_f conserved, but the total number of sites is conserved as well.

In the force computation algorithm, the components of the force between each pair of sites are computed and summed. It is advantageous to calculate the torque components at this point as well since the forces are readily available. Utilizing the site vectors discussed previously, the torque on molecule i applied at site α due to site β on molecule j is given by:

$$\tau^*_{ij\alpha\beta\,x} = \Delta r^*_{i\alpha\,y} F^*_{ij\alpha\beta\,z} - \Delta r^*_{i\alpha\,z} F^*_{ij\alpha\beta\,y} \tag{5–3}$$

with $\tau^*_{ij\alpha\beta\,y}$ and $\tau^*_{ij\alpha\beta\,z}$ obtained by cyclic permutation of the indices x, y, z. The contributions to each component of the torque are summed and the total is used to determine rotation:

$$\tau^*_{i\,x} = \sum_{\substack{j=1 \\ j\neq i}}^{N_t} \sum_{\alpha=1}^{S_i} \sum_{\beta=1}^{S_j} \tau^*_{ij\alpha\beta\,x} \tag{5–4}$$

with other components again given by cyclic permutation.

ROTATION

The molecules are defined using a set of body fixed coordinates. For the linear molecules, all the sites are located at specified distances along the x-axis.

The vector from the center of mass to site α on molecule i is denoted as $\Delta \mathbf{r}^{*\prime}_{i\alpha}$ where the ($'$) signifies the body fixed reference frame. For a two site molecule with a site separation of 0.5 the vectors would be:

$$\Delta \mathbf{r}^{*\prime}_{i1} = (-0.25, 0, 0) \qquad \Delta \mathbf{r}^{*\prime}_{i2} = (0.25, 0, 0) \tag{5–5}$$

In order to translate these vectors into the frame of reference of the simulation volume, they are multiplied by the inverse of the rotation matrix $\mathbf{A}$:

$$\Delta \mathbf{r}^{*}_{i\alpha} = \mathbf{A}^T \cdot \Delta \mathbf{r}^{*\prime}_{i\alpha} \tag{5–6}$$

where the rotation matrix property $A^{-1} = A^T$ has been used. This matrix will be used in all vector rotations. The inverse operation returns the vector to body fixed coordinates:

$$\Delta \mathbf{r}^{*\prime}_{i\alpha} = \mathbf{A} \cdot \Delta \mathbf{r}^{*}_{i\alpha} \tag{5–7}$$

The equations of motion for the Euler angle formulation were presented in Chapter 2. The set of equations (2-16) is presented here so that an important feature can be emphasized:

$$\begin{aligned}
\frac{d\phi}{dt^*} &= -\omega_x^* \frac{\sin\phi\cos\theta}{\sin\theta} + \omega_y^* \frac{\cos\phi\cos\theta}{\sin\theta} + \omega_z^* \\
\frac{d\theta}{dt^*} &= \omega_x^* \cos\phi + \omega_y^* \sin\phi \\
\frac{d\psi}{dt^*} &= \omega_x^* \frac{\sin\phi}{\sin\theta} - \omega_y^* \frac{\cos\phi}{\sin\theta}
\end{aligned} \tag{2 – 16}$$

The term $\sin\theta$ which appears in the denominator of several terms is hazardous numerically. As θ approaches zero, these terms become much too large for the typical time step and the integrator will produce inaccurate values. It is possible

to deal with this a in couple of ways. One is to reduce the time step whenever θ approaches $0, \pi$. The other is to maintain two sets of Euler angles for each molecule, one set with $\theta \frac{\pi}{2}$ out of phase with respect to the other.

Perhaps a more elegant way to deal with the situation is to employ quaternions. The quaternion vector $\mathbf{q}$ is a set of four quantities: $\mathbf{q} = (q_0, q_1, q_2, q_3)$ which define the orientation of a rigid body. Each molecule will have its own quaternion vector which will change with time. The additional degree of freedom in the quaternion representation is used in satisfying the constraint:

$$q_0^2 + q_1^2 + q_2^2 + q_3^2 = 1 \tag{5–8}$$

The quaternion vector is related to the Euler angles by the following:

$$\begin{aligned} q_0 &= \cos\frac{1}{2}\theta \cos\frac{1}{2}(\phi + \psi) \\ q_1 &= \sin\frac{1}{2}\theta \cos\frac{1}{2}(\phi - \psi) \\ q_2 &= \sin\frac{1}{2}\theta \sin\frac{1}{2}(\phi - \psi) \\ q_3 &= \cos\frac{1}{2}\theta \sin\frac{1}{2}(\phi + \psi) \end{aligned} \tag{5–9}$$

Except perhaps during initialization, there will be no need to use the Euler angles themselves so the inverse conversion is not required. All the molecular orientation information will be stored in the quaternions. In the quaternion formulation, the matrix A can be expressed as:

$$A = 2 \begin{bmatrix} q_0^2 + q_1^2 - \frac{1}{2} & q_1 q_2 + q_0 q_3 & q_1 q_3 - q_0 q_2 \\ q_1 q_2 - q_0 q_3 & q_0^2 + q_2^2 - \frac{1}{2} & q_2 q_3 + q_0 q_1 \\ q_1 q_3 + q_0 q_2 & q_2 q_3 - q_0 q_1 & q_0^2 + q_3^2 - \frac{1}{2} \end{bmatrix} \tag{5–10}$$

The following matrix $\mathbf{W}$ will also be useful:

$$\mathbf{W} = \begin{bmatrix} q_0 & q_1 & q_2 & q_3 \\ -q_1 & q_0 & q_3 & -q_2 \\ -q_2 & -q_3 & q_0 & q_1 \\ -q_3 & q_2 & -q_1 & q_0 \end{bmatrix} \tag{5–11}$$

At any time the location of a site in space fixed coordinates can be determined using the body fixed vector, $\Delta \mathbf{r}_{i\alpha}^{*\prime}$ and the rotation matrix A as in equation (5-6). The matrix A is different for each molecule at each time step since it depends on the quaternions. Tracking the orientation of the molecule is therefore accomplished by integrating the equations of "motion" for the quaternions. This is performed using the following procedure.

The fifth order Gear predictor corrector method will be used for the quaternions just as it was for the position vectors. Since the two are directly analogous, the derivatives of the quaternions will be denoted by suffixing the letter used for the corresponding translational derivative:

$$\frac{d\mathbf{q}}{dt^*} = \frac{dq_0}{dt^*}, \frac{dq_1}{dt^*}, \frac{dq_2}{dt^*}, \frac{dq_3}{dt^*} = \mathbf{qv} \tag{5–12}$$

with similar relations holding for $\mathbf{qa}, \mathbf{qb}, \mathbf{qc}, \mathbf{qd}$. The quaternions and their derivatives are taken to be non-dimensional. The predictor step for the quaternions is then:

$$
\begin{aligned}
\mathbf{q}(t^*+p^*) &= \mathbf{q}(t^*) + \Delta t^* \mathbf{qv}(t^*) + \frac{\Delta t^{*2}}{2}\mathbf{qa}(t^*) \\
&\quad + \frac{\Delta t^{*3}}{6}\mathbf{qb}(t^*) + \frac{\Delta t^{*4}}{24}\mathbf{qc}(t^*) + \frac{\Delta t^{*5}}{120}\mathbf{qd}(t^*) \\
\mathbf{qv}(t^*+p^*) &= \mathbf{qv}(t^*) + \Delta t^* \mathbf{qa}(t^*) + \frac{\Delta t^{*2}}{2}\mathbf{qb}(t^*) + \frac{\Delta t^{*3}}{6}\mathbf{qc}(t^*) + \frac{\Delta t^{*4}}{24}\mathbf{qd}(t^*) \\
\mathbf{qa}(t^*+p^*) &= \mathbf{qa}(t^*) + \Delta t^* \mathbf{qb}(t^*) + \frac{\Delta t^{*2}}{2}\mathbf{qc}(t^*) + \frac{\Delta t^{*3}}{6}\mathbf{qd}(t^*) \\
\mathbf{qb}(t^*+p^*) &= \mathbf{qb}(t^*) + \Delta t^* \mathbf{qc}(t^*) + \frac{\Delta t^{*2}}{2}\mathbf{qd}(t^*) \\
\mathbf{qc}(t^*+p^*) &= \mathbf{qc}(t^*) + \Delta t^* \mathbf{qd}(t^*) \\
\mathbf{qd}(t^*+p^*) &= \mathbf{qd}(t^*)
\end{aligned}
\tag{5–13}
$$

Since the new quaternions are available at this stage it is efficient to make use of them to calculate **A**. This matrix is then used to calculate and store the space fixed coordinates of the sites using equation (5-6). The extra memory required to store these is more than compensated for by the fact that the matrix multiplications need to be performed only once per site rather than up to 50 times per site in the force calculation.

The next step is to go through the force and torque calculation. Once this is complete the torque on each molecule will be available in space fixed coordinates. These values are transformed to body fixed coordinates as in equation (5-7). Even though the Euler angles are not employed, the angular velocities and accelerations in the body fixed coordinates act as useful temporary place holders. They are calculated from the quaternions according to:

$$
\begin{pmatrix} 0 \\ \omega'_x \\ \omega'_y \\ \omega'_z \end{pmatrix} = 2\mathbf{W} \cdot \mathbf{qv} \tag{5–14}
$$

All the quantities needed to calculate the angular accelerations in equation (2-15) are now available:

$$\begin{aligned}
\frac{d\omega_x^{*\prime}}{dt^*} &= \frac{\tau^{*\prime}}{I_{xx}^*} + \left(\frac{I_{yy}^* - I_{zz}^*}{I_{xx}^*}\right)\omega_y^{*\prime}\omega_z^{*\prime} \\
\frac{d\omega_y^{*\prime}}{dt^*} &= \frac{\tau^{*\prime}}{I_{yy}^*} + \left(\frac{I_{zz}^* - I_{xx}^*}{I_{yy}^*}\right)\omega_z^{*\prime}\omega_x^{*\prime} \\
\frac{d\omega_z^{*\prime}}{dt^*} &= \frac{\tau^{*\prime}}{I_{zz}^*} + \left(\frac{I_{xx}^* - I_{yy}^*}{I_{zz}^*}\right)\omega_x^{*\prime}\omega_y^{*\prime}
\end{aligned} \qquad (2-15)$$

The angular accelerations are then used to obtain the second derivative of the quaternions:

$$\mathbf{qa} = \frac{1}{2}\mathbf{W}^T \begin{pmatrix} -2\sum_{i=0}^{4} q_i^2 \\ \alpha_x' \\ \alpha_y' \\ \alpha_z' \end{pmatrix} \qquad (5\text{–}15)$$

Finally, just as in the translational motion, the quaternion "acceleration" is used to correct the predictions that were made.

$$\Delta\mathbf{qa} = \mathbf{qa}(t^* + \Delta t^*) - \mathbf{qa}(t^* + p^*) \qquad (5\text{–}16)$$

This correction factor is now used to correct the other values:

$$\begin{aligned}
\mathbf{q}(t^* + \Delta t^*) &= \mathbf{q}(t^* + p^*) + k_0\Delta\mathbf{qa} \\
\mathbf{qv}(t^* + \Delta t^*) &= \mathbf{qv}(t^* + p^*) + k_1\Delta\mathbf{qa} \\
\mathbf{qb}(t^* + \Delta t^*) &= \mathbf{qb}(t^* + p^*) + k_3\Delta\mathbf{qa} \\
\mathbf{qc}(t^* + \Delta t^*) &= \mathbf{qc}(t^* + p^*) + k_4\Delta\mathbf{qa} \\
\mathbf{qd}(t^* + \Delta t^*) &= \mathbf{qd}(t^* + p^*) + k_5\Delta\mathbf{qa}
\end{aligned} \qquad (5\text{–}17)$$

In this way the quaternions are advanced in time and the molecular rotation is achieved. For the linear molecules, $\omega_x^{*\prime}$ and $\alpha_x^{*\prime}$ are both zero. This eliminates the

need to calculate the $\omega_x^{*\prime}$ row of equation (5-14) and the first equation in set (2-15), which works out nicely since I_{xx} is zero and would otherwise cause problems.

If the equilibration phase is sufficiently long, then the initial conditions for the quaternions are not critical. Simulation runs were performed for this study with various initial molecular orientations and angular velocities. It was found that the equilibration phase used for the translational motion is also long enough for the rotation. No statistically distinguishable differences were found between the simulations with different initial conditions. For simplicity, the molecules are initially oriented normal to the walls with zero initial angular velocity.

CHANNEL FLOW

The channel flows for molecular systems are driven in the same way as the atomic systems. The wall motion for the plane Couette flow is exactly the same as in the earlier case. For the plane Poiseuille flow, the body force is applied at the center of mass. As was the case with the atomic systems, the flow introduces energy. A similar mechanism will be used to maintain constant temperature.

Originally the thermostat given in equations (4-31) and (4-32) was used to maintain the molecular temperature. The extremely high flow rate combined with the time step prevented the interchange of sufficient energy between the rotational and translational mode. The rotational temperature increased until it overwhelmed the program.

It is undesirable to shorten the time step much more and for the lower flow rates the noise tends to overwhelm the trends that are sought after. A way to circumvent these problems is to remove energy from the rotational modes as well. The total kinetic energy of the molecular system is given by:

$$\frac{1}{2}\sum_{i=1}^{N_f} v_i^{*2} + \frac{1}{2}\sum_{k=x,y,z} I_{kk}\sum_{i=1}^{N_f}\omega_{i\,k}^{*\prime 2} = \frac{6N_f}{2}T_0 \tag{5–18}$$

A development similar to the one used in for the monatomic particles then yields:

$$\lambda = -\frac{\sum_{i=1}^{N_f}\mathbf{v}_i^*\cdot\mathbf{F}_i^* + \sum_{k=x,y,x}\sum_{i=1}^{N_f}\tau_{i\,k}^{*\prime}\omega_{i\,k}^{*\prime}}{m^*\sum_{i=1}^{N_f}\mathbf{v}_i^*\cdot\mathbf{v}_i^* + \sum_{k=x,y,z} I_{kk}\sum_{i=1}^{N_f}\omega_{i\,k}^{*\prime 2}} \tag{5–19}$$

The parameter λ is used as the coefficient of a rotational damping term, similar to the translational case:

$$\mathbf{qa}_{i\ isothermal} = \mathbf{qa}_i + \lambda_i\mathbf{qv}_i \tag{5–20}$$

This step is applied after the rotation, right before the final corrector step.

Now that the simulation incorporates molecules in a shear flow, the orientation properties can be defined. The parameter of interest is the angle between the axis of the molecule and the wall, θ, as shown in Figure 21. This should not be confused with the Euler angle θ which is not used. Since there is no expected variation in the y-direction, the angles will be projected onto the x-z plane passing through the center of mass of the molecule. Since the molecules are rod-like in nature, this angle can be determined by using any one of the sites:

$$\theta_i = \tan^{-1}\left(\frac{\Delta r_{i\alpha\,z}}{\Delta r_{i\alpha\,x}}\right) \tag{5–21}$$

The molecules are symmetric about the y'-z' plane so the angles will be adjusted to fall in the range $\{-90° \le \theta \le 90°\}$.

The development of the simulation procedure is now complete. The next chapter will discuss the results for the atomic and molecular channel flow.

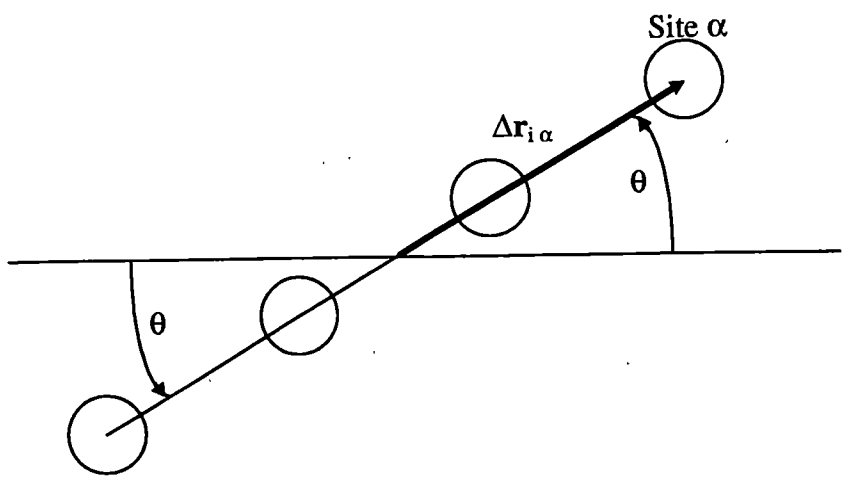

Figure 21. Definition of θ.

CHAPTER 6: RESULTS AND DISCUSSION

VALIDATION

A computer code was written following the mathematical development discussed in Chapters 4 and 5. The code was written in C and was executed on various machines over the course of the research. The validation simulations were executed on a 90 MHz Intel Pentium processor. The production simulations were executed on an SGI Origin. For both cases run times were on the order of 1 to 2 days.

Before the molecular orientation was investigated, simpler simulations were performed to validate the code. The validation simulations model atomic fluids in a channel with no flow generation. They are micro-canonical ensembles so the thermostat is also absent. These simulations do promote confidence in all other aspects of the program, including potentials, numerical integration and initial and boundary conditions. Once the basic program is working properly it is a straightforward process to add levels of complexity and test them individually.

Many errors manifest themselves in an obvious manner. Infinite velocities were encountered several times and led to corrections in the integration and boundary condition algorithms. Another simple check that was implemented was to flag a particle passing beyond the walls as a fatal error. This error led to corrections and adjustments in the wall boundary conditions as well as adjustments in the time step and the parameters governing the flow generation.

Other errors are more subtle. These include problems that might not technically be called errors such as failure to reach equilibrium. Protection from this kind of error is obtained mainly through comparison with previous work and theoretical and experimental results.

A simple simulation was performed with $N_f = 108$ particles, $\rho = 0.7$, and $E_t^* = -1.03$ for 50,000 time steps. The results were compared with Haile [27] for the same values:

Simulation	$\langle T^* \rangle$	$\langle P^* \rangle$	$\langle U^* \rangle$
Haile	2.14	3.41	-4.22
Maxwell	2.11	3.36	-4.23

The results are quite close even though the run was relatively short. A series of runs were made with $E_t^* = -3.54$, and $N_f = 2000$ for different lengths:

Equilibration	Production	$\langle T^* \rangle$	$\langle P^* \rangle$	$\langle U^* \rangle$	η_{xy}
20,000 steps	50,000 steps	1.10	0.572	-5.225	0.21
10,000 steps	100,000 steps	1.12	0.634	-5.213	0.16
50,000 steps	500,000 steps	1.10	0.568	-5.226	0.144
100,000 steps	1,000,000 steps	1.10	0.568	-5.226	0.150

These results exemplify several things. First, even though the second run was longer than the first, the equilibration phase was apparently not long enough and the values are off. There is little change between runs 1, 3, and 4 except for the viscosity. This seems to indicate that a run with 20,000 equilibrium steps and 100,000 production steps would probably be sufficient if the viscosity were not needed. As mentioned in Chapter 4, accurate viscosity calculations require very long simulations. The fact that the values for runs 3 and 4 were within 5% is very encouraging . The viscosity formulation discussed is not valid for the non-equilibrium channel flows and so the viscosity calculation will not be performed from here on. It has served its purpose in promoting confidence in the program.

The density profile for a channel with no flow is presented in Figure 22. This is generated by dividing the channel into bins and summing the number of particles in each bin every ten time steps. At the end of the simulation, the total number of particles in each bin is divided by the total number of particles, equal to N_f multiplied by the total number of production time steps divided by ten.

The density profile shows that near the wall the particles accumulate into layers. This compares very well with the previous results shown in Chapter 2. For the few bins very close to the wall, there are no particles.

The simulation velocity profiles were generated by using the same bins as for the density profile and summing the velocities of the particles in each bin. At the end of the simulation, an average velocity for each bin is calculated using the total velocity and the total number of particles for that bin. The average velocity for each bin along the channel is then plotted to produce the velocity profile.

For the no flow case, the velocity profile shows a zero average value as expected in Figure 23. However, in one bin right near the wall there is a significant non-zero average velocity. On comparison with the density profile, however, it is seen that this bin contains very few particles in comparison with the other bins. This suggests that a particle requires a large velocity to move into this region and that the direction of this velocity is biased. It may even indicate a subtle circulation region.

CHANNEL FLOW

Plane Couette and plane Poiseuille flow both admit analytic solutions under the no-slip condition. For the plane Couette flow the velocity profile is linear as in Figure 24. The plane Poiseuille flow has a parabolic velocity profile Figure 25 [52]. The governing values in these figures are the wall velocity for plane Couette

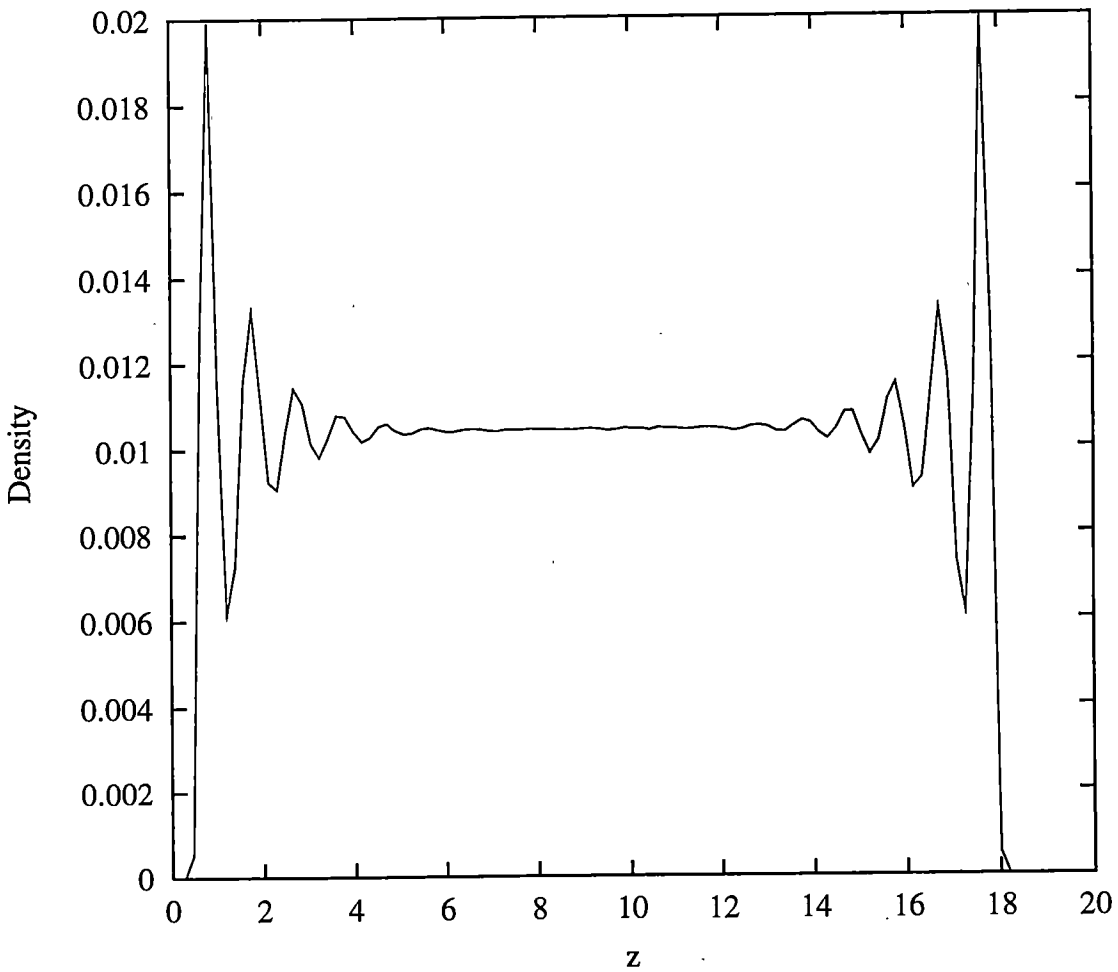

Figure 22. Density profile for the no flow case.

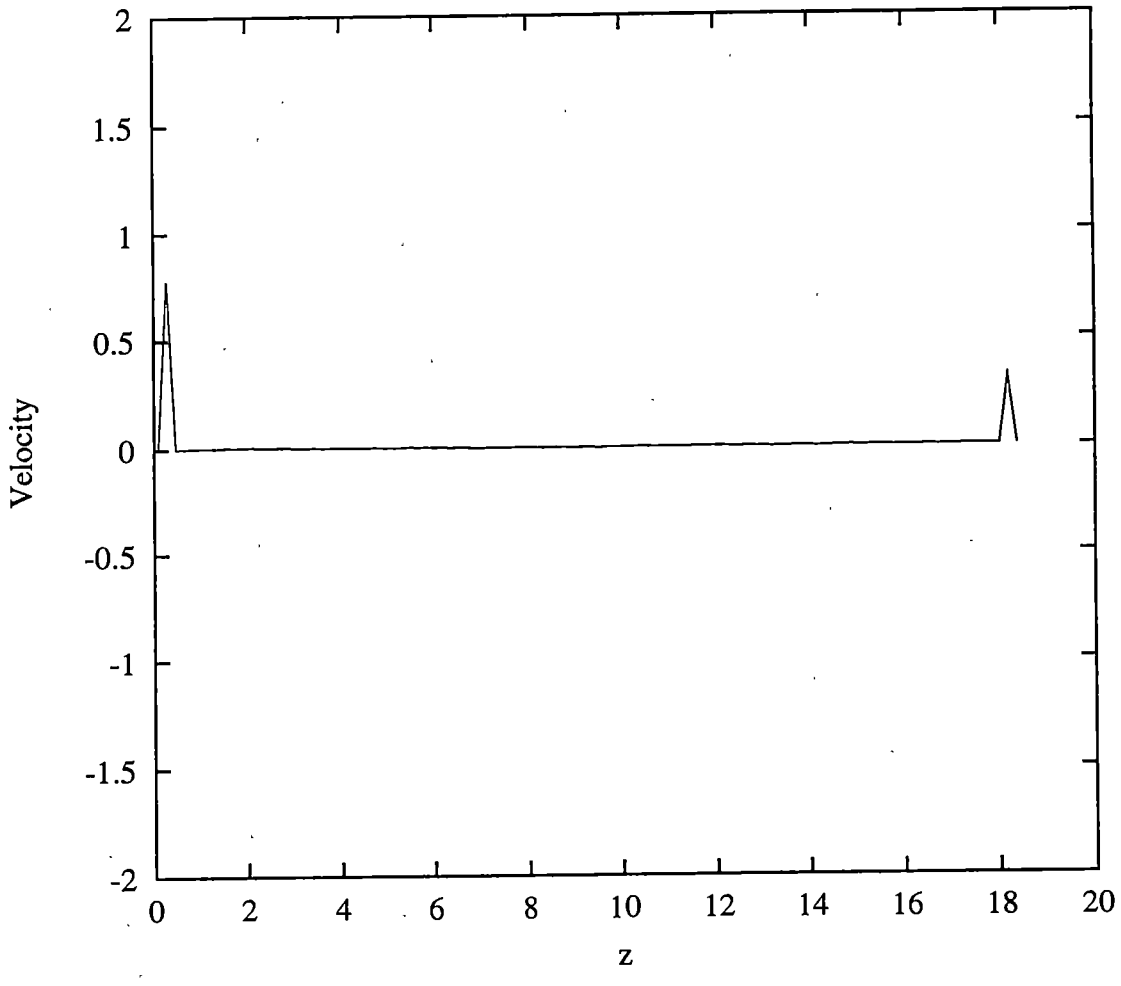

Figure 23. Velocity profile for the no flow case.

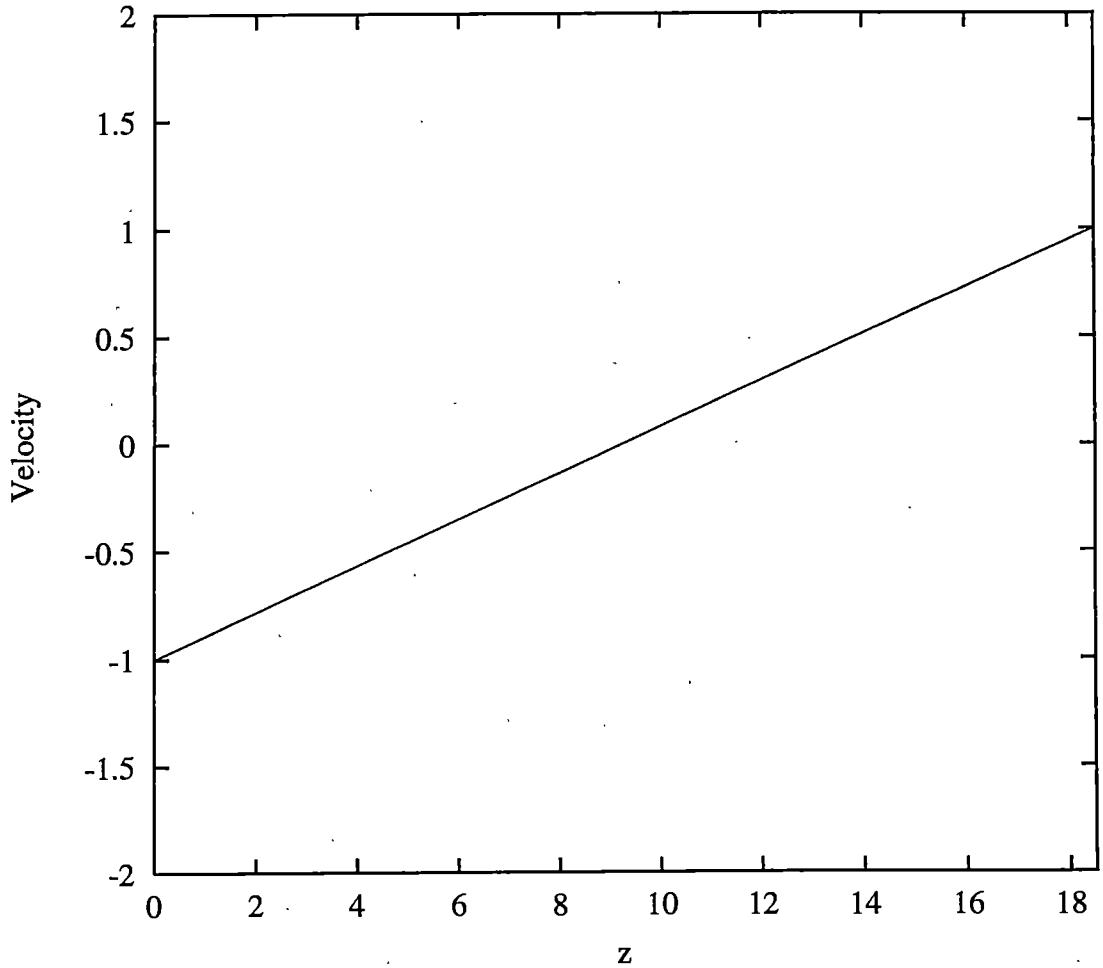

Figure 24. Analytic plane Couette velocity profile.

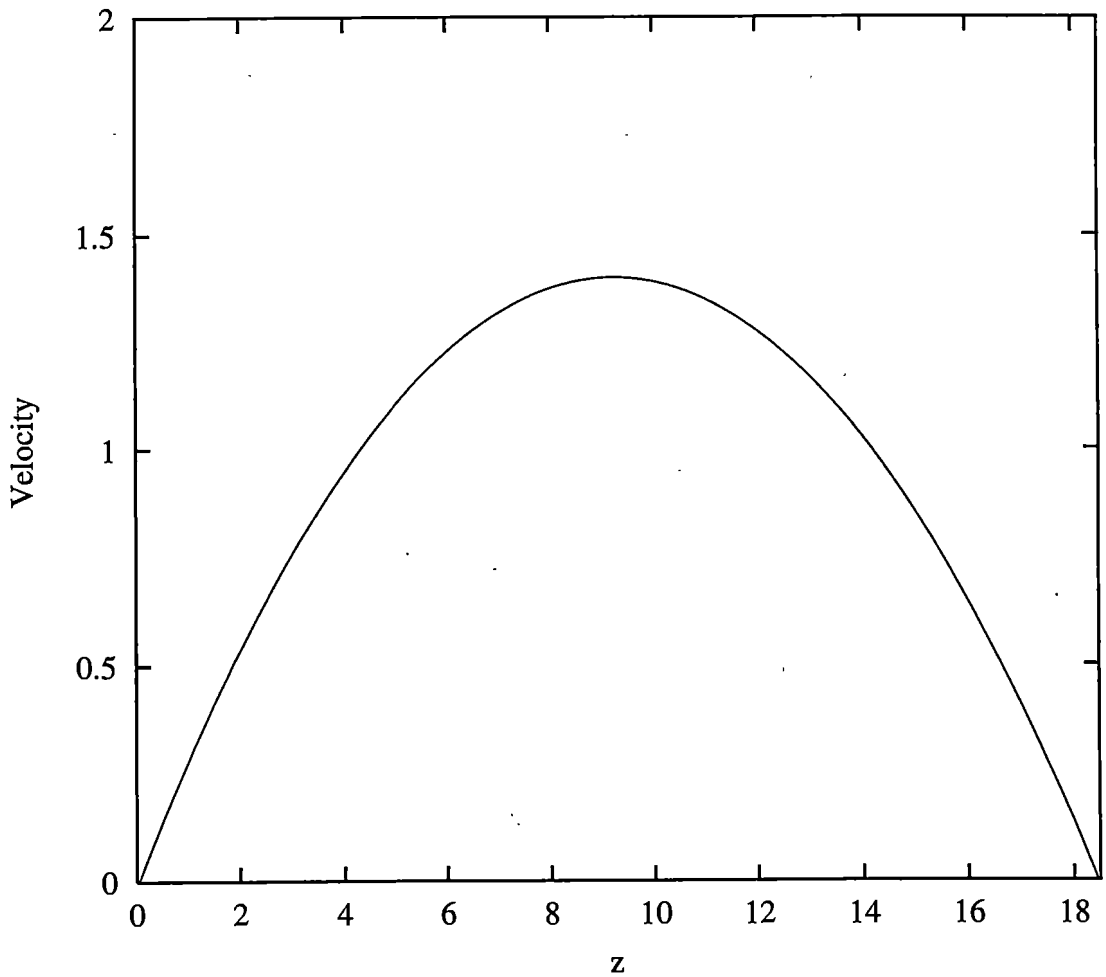

Figure 25. Analytic plane Poiseuille velocity profile.

flow and the pressure gradient for the plane Poiseuille flow. The results of the simulations will be presented in non-dimensional form and so the governing values have also been non-dimensionalized in the preceding figures. Using the parameters for Argon, $\sigma = 3.4 \times 10^{-10}$ m, $\epsilon = 1.66 \times 10^{-21}$ J/atom, $m_r = 6.69 \times 10^{-26}$ kg and $t_r = 2.16 \times 10^{-12}$ s, the dimensionalized wall velocity is 157 m/s and the pressure gradient is 6.21×10^{15} Pa/m. These values are very high and reflect the substantial driving force required to induce significant motion in a channel of sub-micron dimensions.

Velocity and density profiles for various plane Couette flows are shown. The simulation in Figures 26 and 27 is for 500 particles, while Figures 28 and 29 show a 2000 particle run. In Figures 30 and 31 the velocity of the bottom wall was set to zero. Due to the gap at the wall, this last simulation does not represent half of the previous simulation very wall as was anticipated.

One feature common to many of the plane Couette results is the discrepancy between the wall velocity (-1.0, 1.0) and the velocity of the fluid near the wall. This is a demonstration of the fact that the no-slip condition does not necessarily hold at molecular scales. Previous studies have shown what is evident here, that the degree of slip depends on various factors including the configuration, density and interaction strength at the walls. Figures 32 and 33 are for a 2000 particle run with a higher bin resolution to investigate the wall anomalies in depth.

Slip at the walls can also be seen in the plane Poiseuille results, Figures 34 and 35. This is manifested as a nonzero velocity at the wall and does affect the maximum velocity attained in the center of the fluid. For both types of flow, anomalies at the wall can be seen. These are very similar to the spikes seen for the no flow case and are again found in bins with a relatively small number of particles.

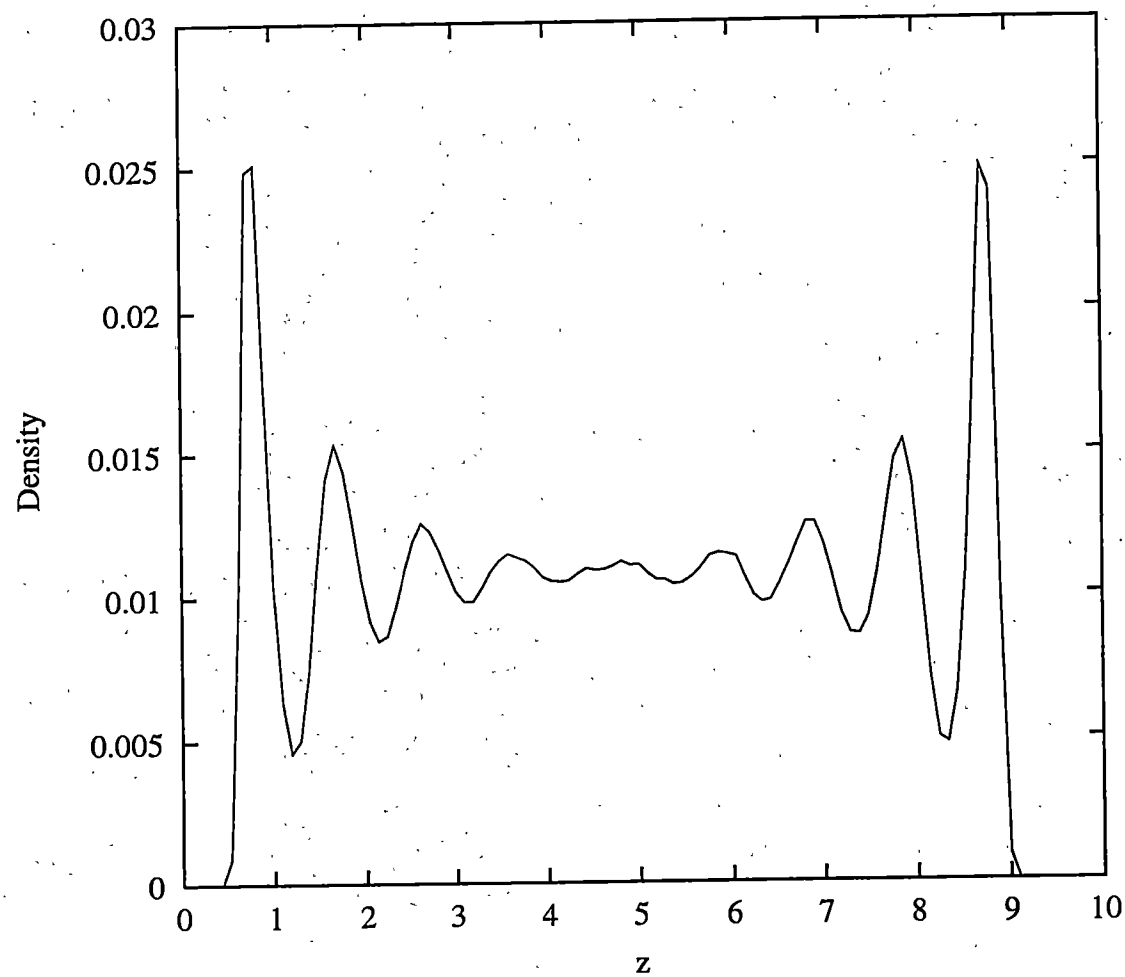

Figure 26. Density profile for the 500 particle plane Couette flow.

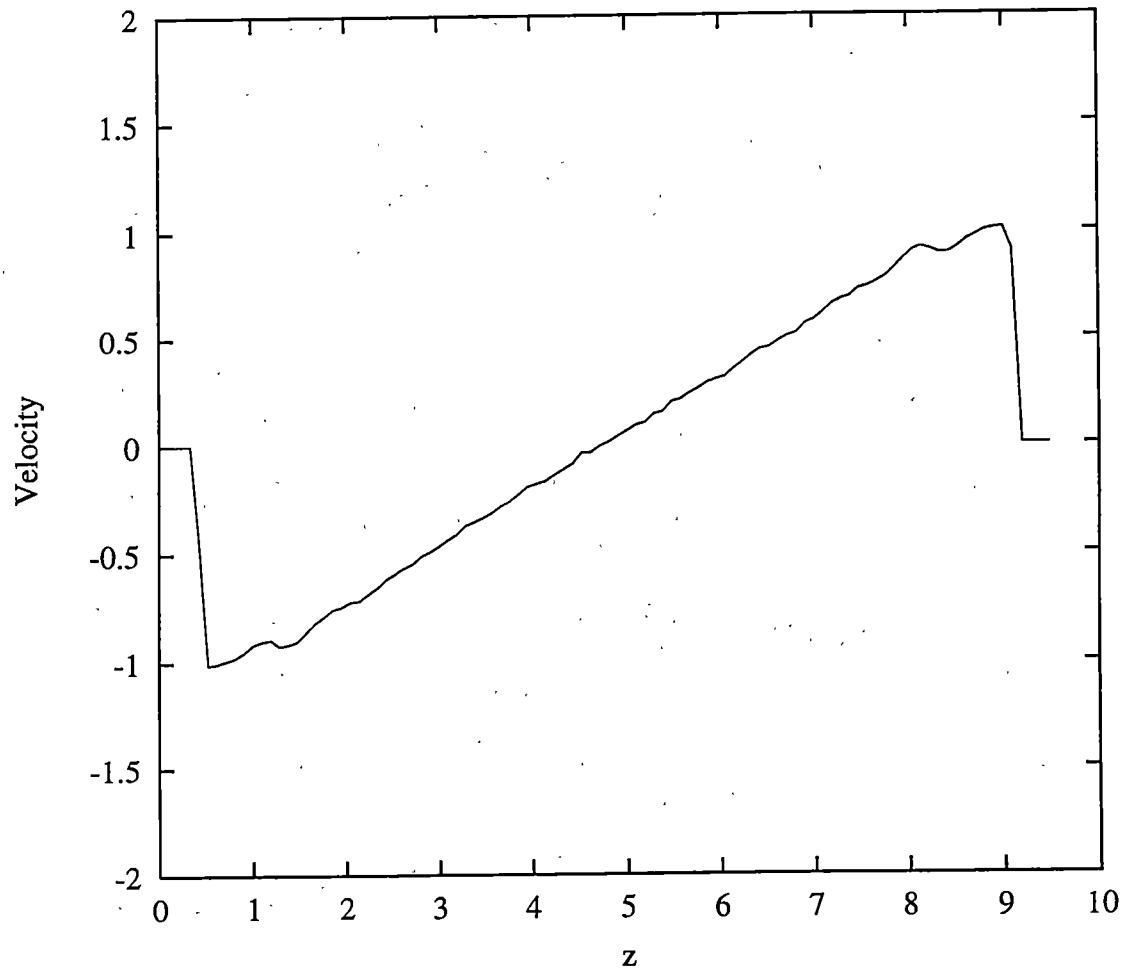

Figure 27. Velocity profile for the 500 particle plane Couette flow.

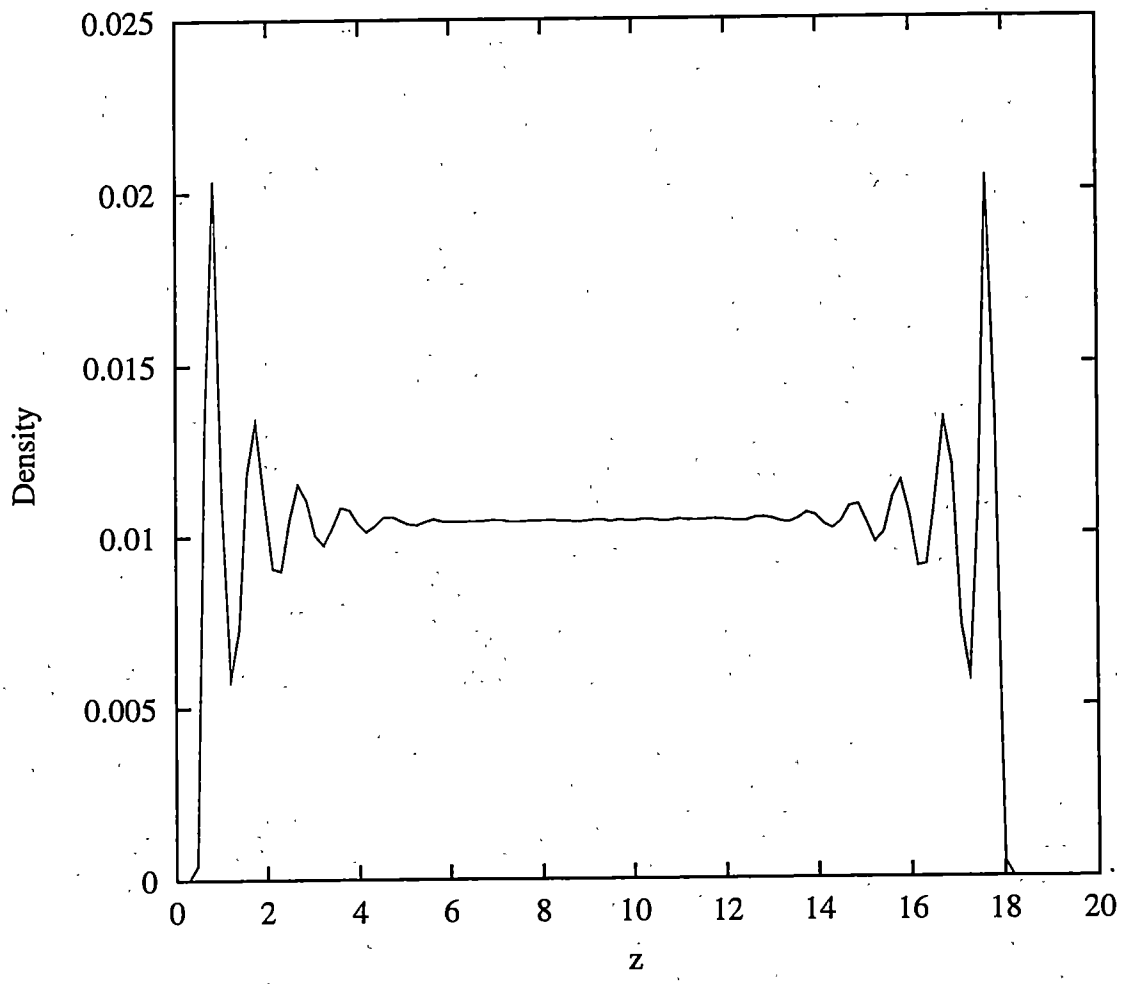

Figure 28. Density profile for the 2000 particle plane Couette flow.

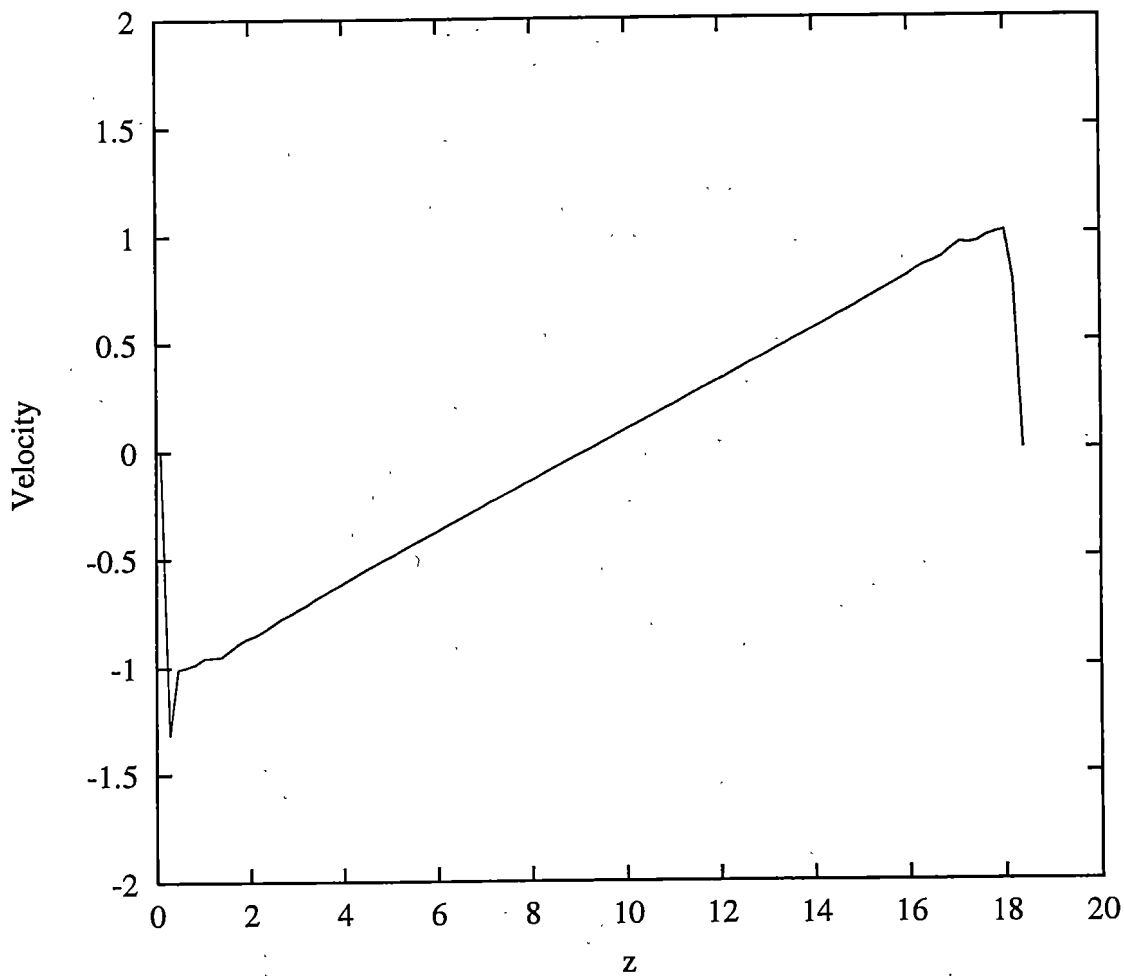

Figure 29. Velocity profile for the 2000 particle plane Couette flow.

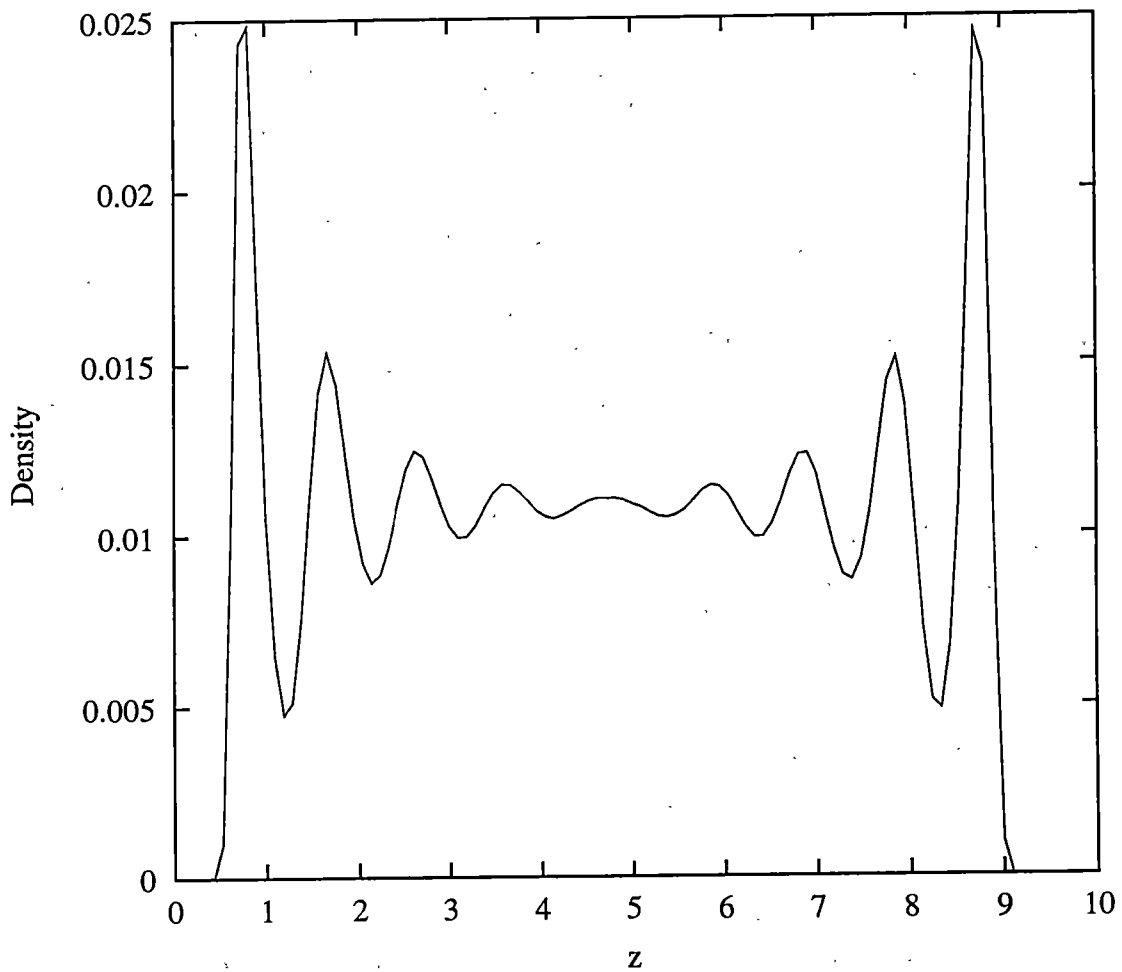

Figure 30. Density profile for the 1000 particle plane Couette flow with stationary bottom wall.

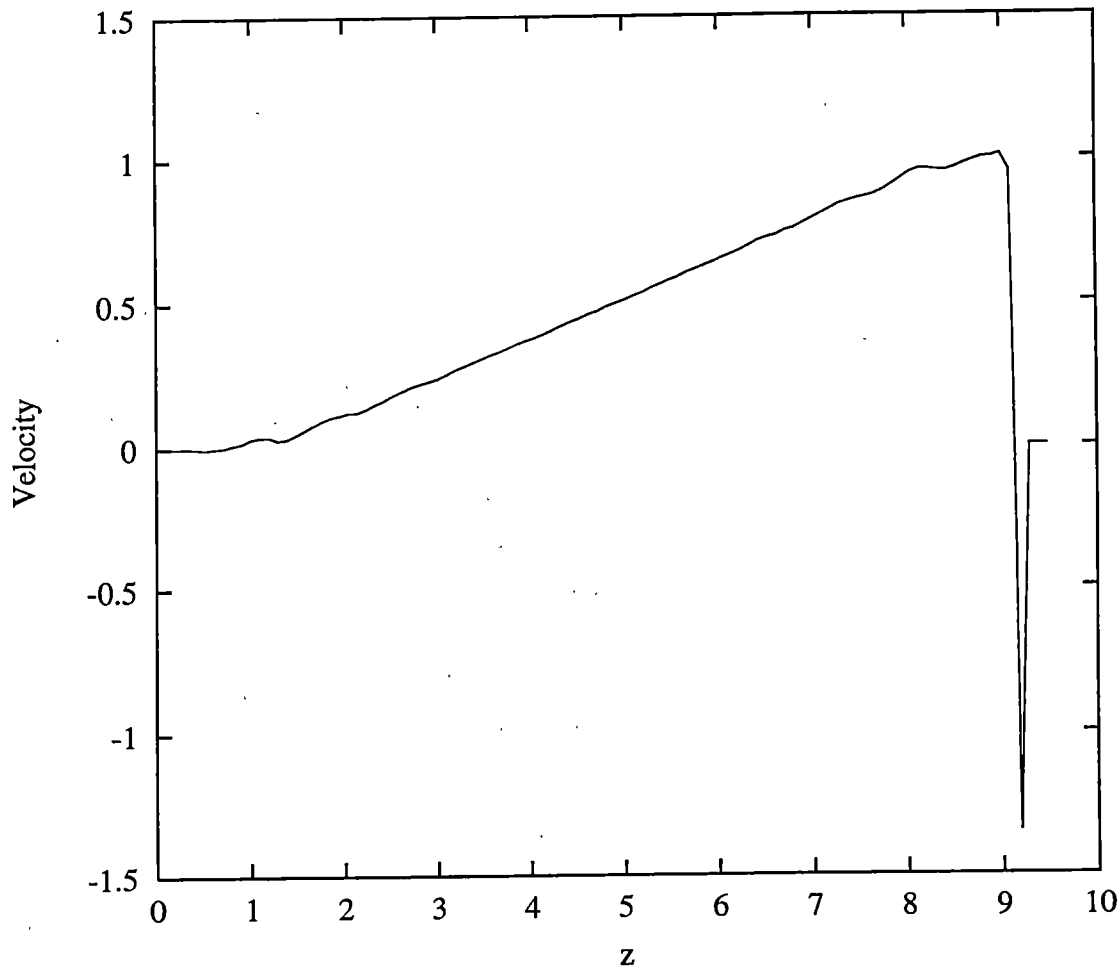

Figure 31. Velocity profile for the 1000 particle plane Couette flow with stationary bottom wall.

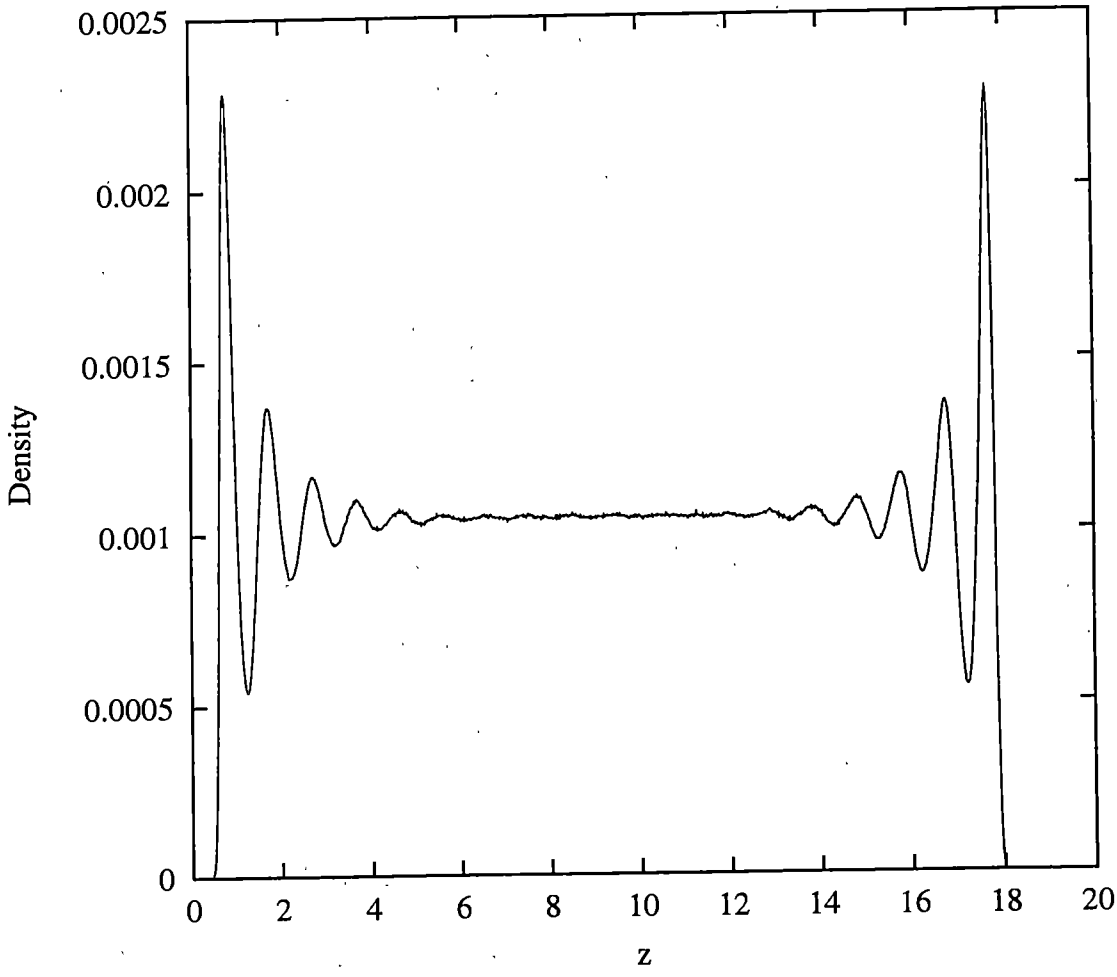

Figure 32. High resolution density profile for the 2000 particle plane Couette flow.

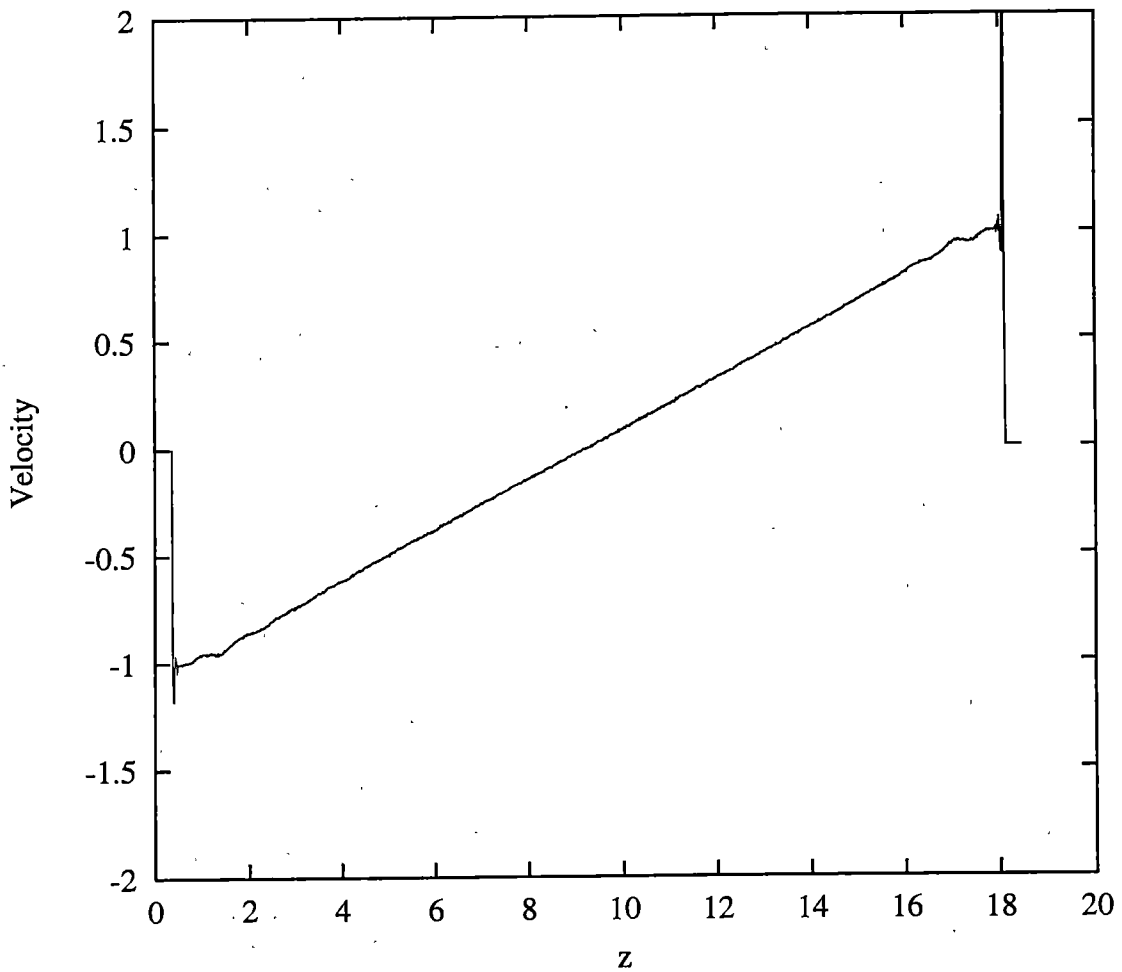

Figure 33. High resolution velocity profile for the 2000 particle plane Couette flow.

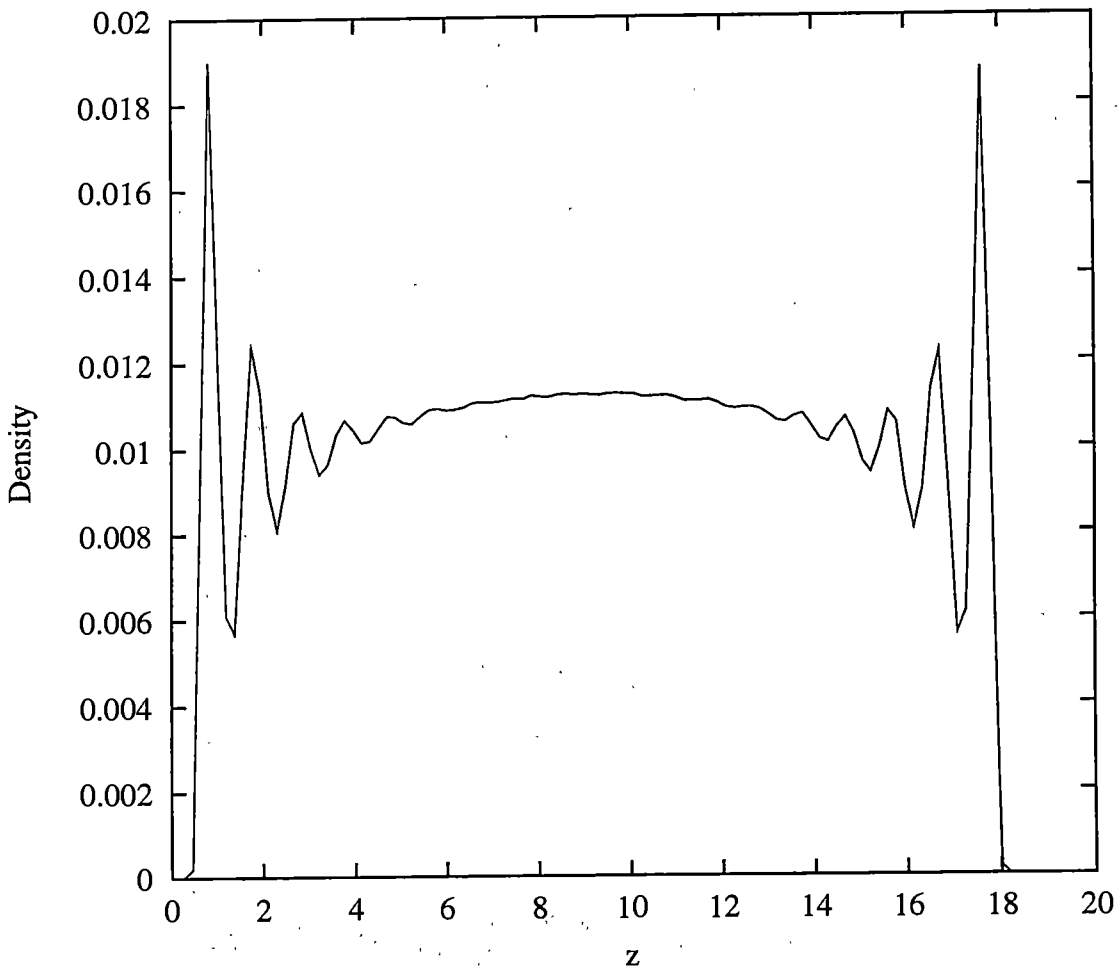

Figure 34. Density profile for the 2000 particle plane Poiseuille flow.

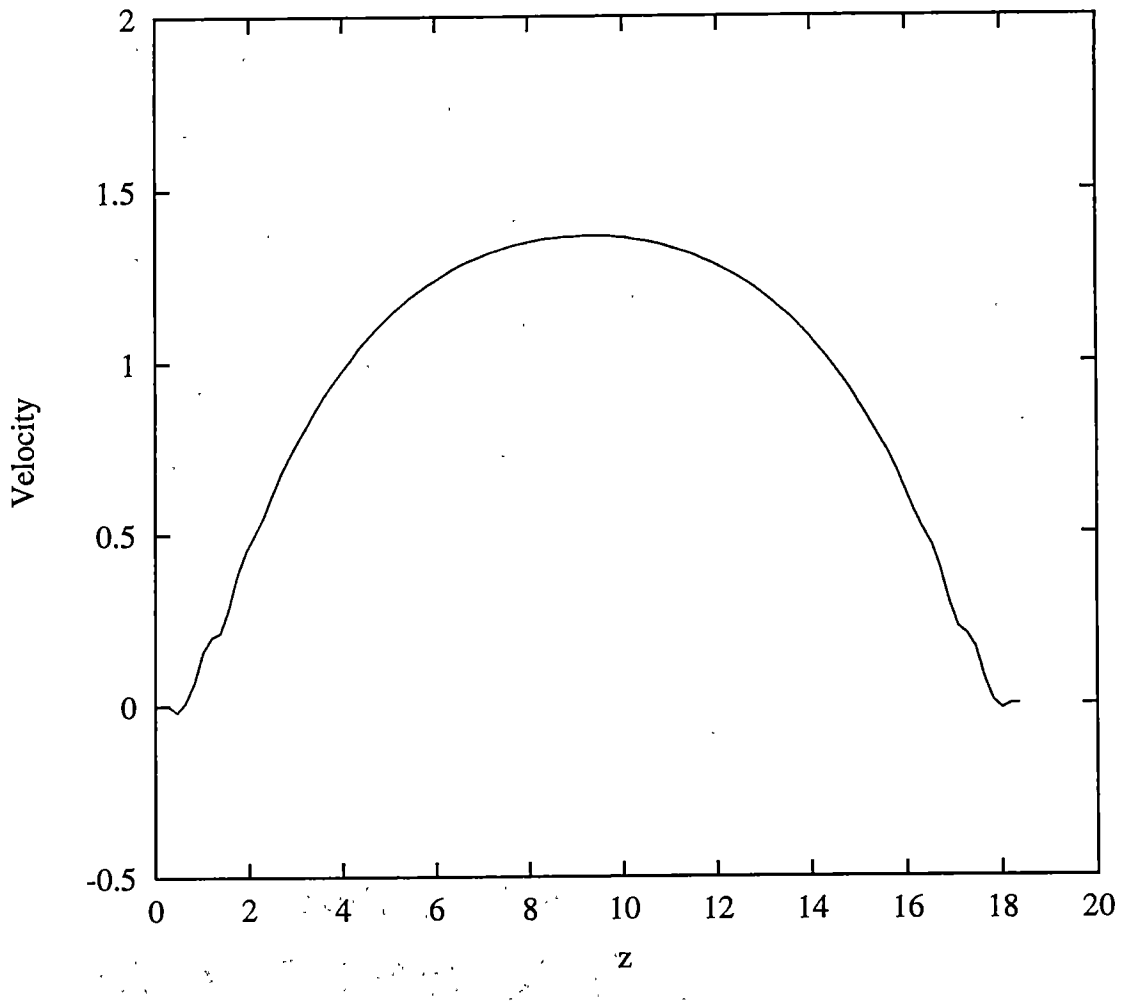

Figure 35. Velocity profile for the 2000 particle plane Poiseuille flow.

Despite the slip, the velocity profiles are very similar to the analytic profiles. At this point confidence has been gained in the implementation of the channel flow. The slip was investigated in greater detail after the molecules were simulated.

MOLECULES

Molecules were added to the code following the development in Chapter 5. The molecules used in the simulations in this section consist of two sites separated by 0.5. In addition to the density and velocity plots for the molecular simulations, angular distribution plots will be provided. Again the channel width is divided into bins. Each bin contains an array of 181 elements. In each element is stored the sum of the particles in that bin with an angular orientation of a given integral angle measured in degrees as in equation (5-21). This accumulation is performed every ten time steps. As with the density profiles, the final values are normalized by the total number of particles counted and are displayed using plots in the range $-90° \leq \theta \leq 90°$.

The angular orientation plot is anticipated to be the location where the effect of the shear on the molecular orientation will manifest itself. Shear is defined according to the following:

$$\tau^*_{xz} = \frac{dv^*_x}{dz^*} \tag{6-1}$$

where τ^*_{xz} is the shear that is under investigation, and $\frac{dv^*_x}{dz^*}$ is the velocity gradient. For no flow, Figures 36 and 37, the velocity is constant and so the shear should be zero. There should not, therefore, be any indication of orientational preference. This is reflected in Figure 38 where the number of particles at a given angle is very close to the average orientation across the width of the channel. An exception is

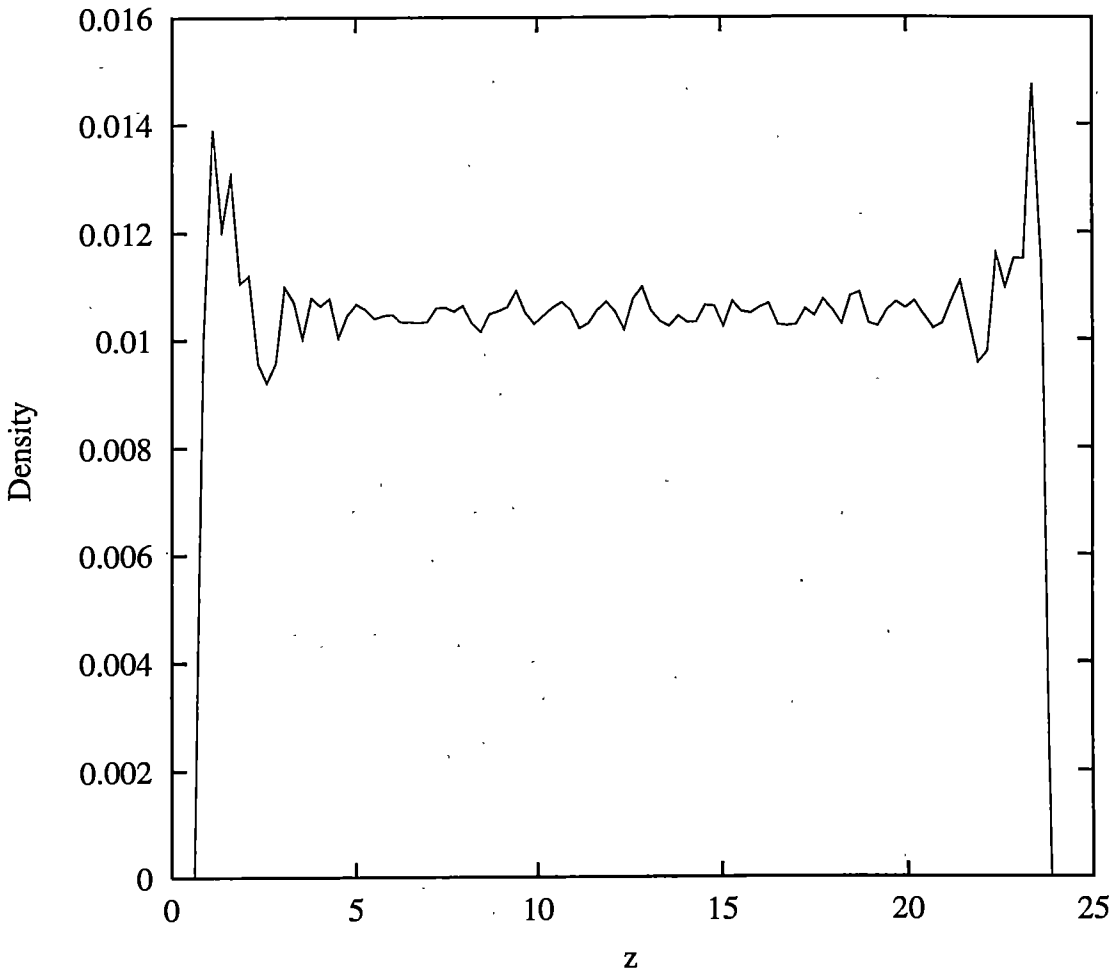

Figure 36. Density profile for the 2000 molecule no flow case.

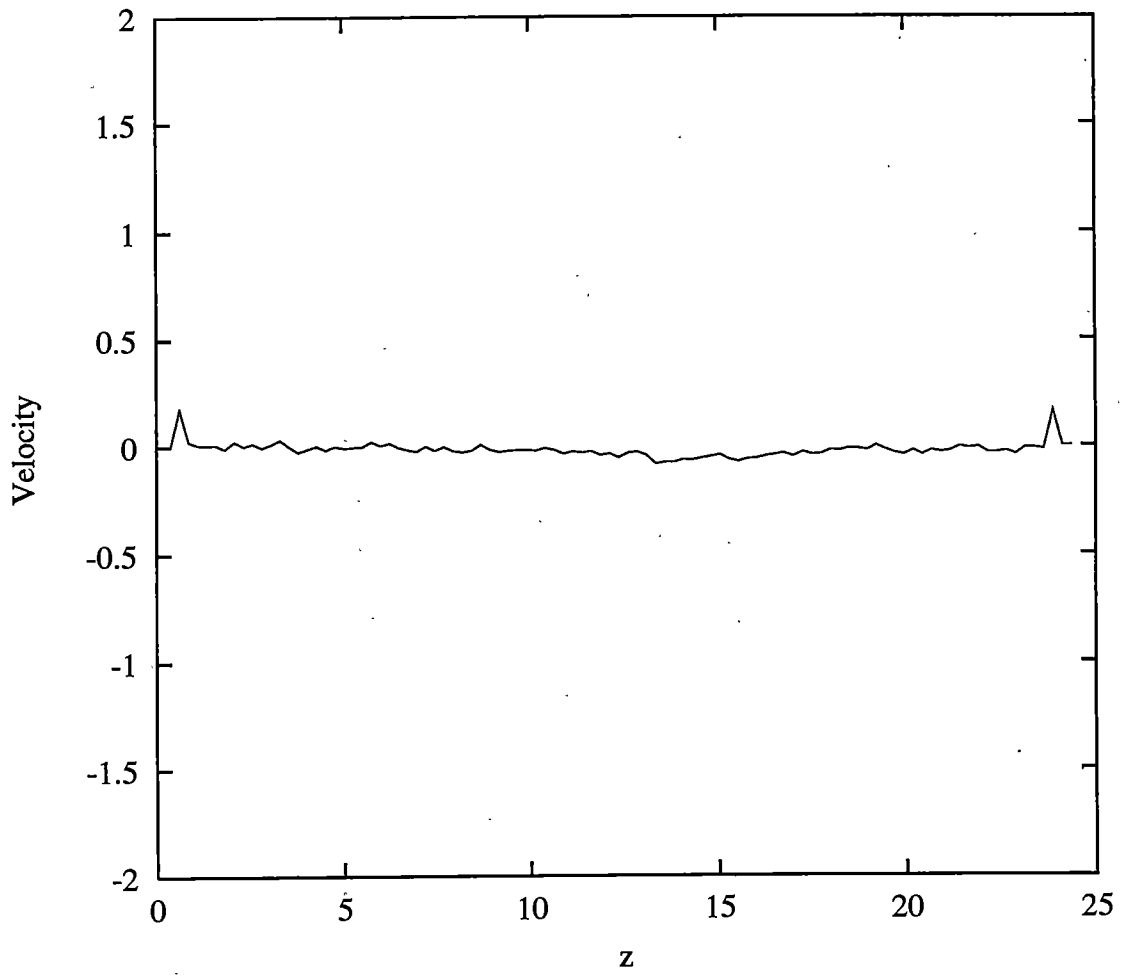

Figure 37. Velocity profile for the 2000 molecule no flow case.

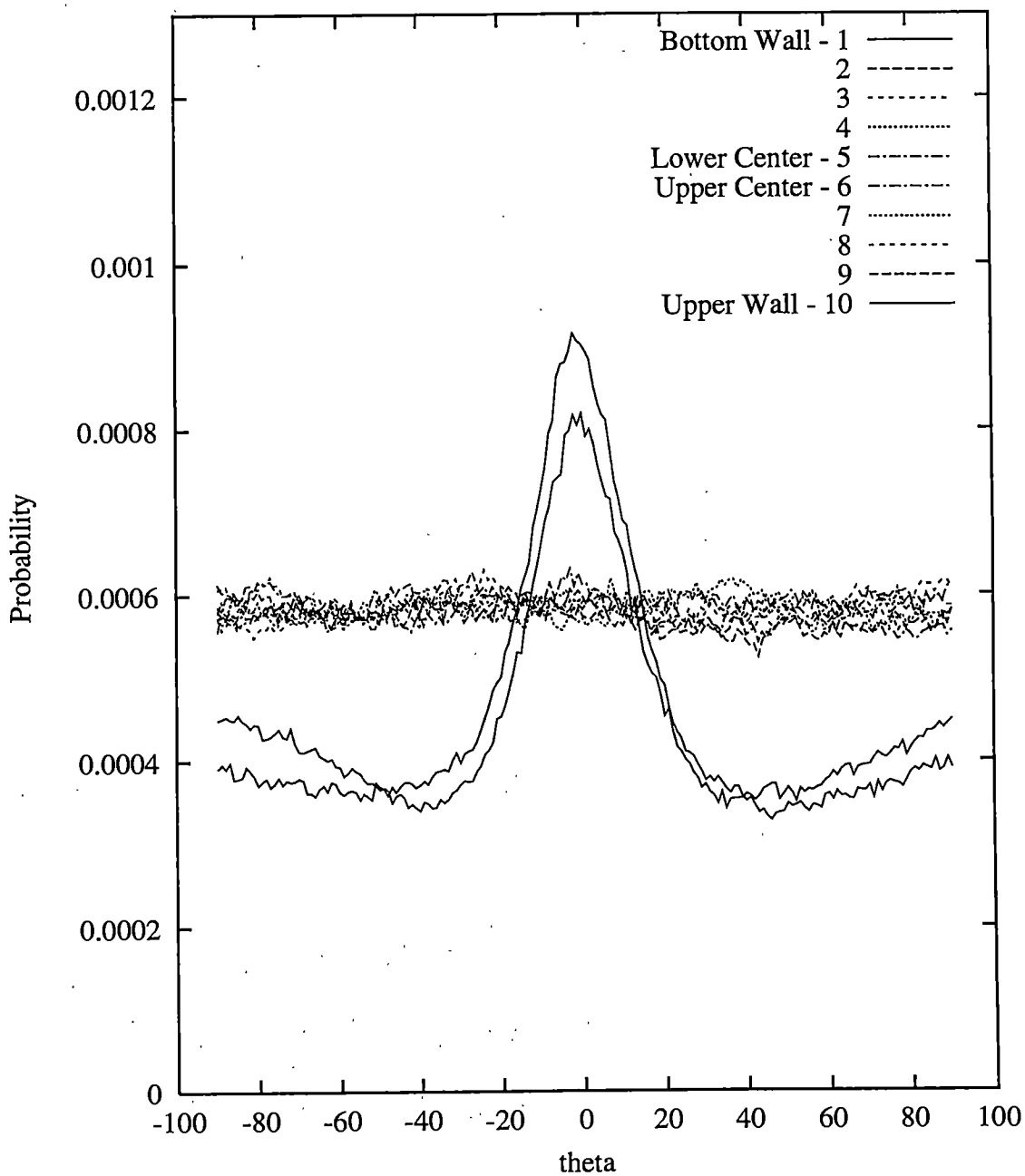

Figure 38. Angular distribution for the 2000 molecule no flow case.

seen near the wall where the molecules tend to align about $\theta = 0°$. This will be seen as well in the other flows and will be discussed later.

Figures 39-41 present the molecular plane Couette flow. As seen in Figure 40, the velocity varies linearly across the channel. This leads to a constant shear. As seen in Figure 41, again with the exception of the bins closest to the wall, the molecules exhibit a preferential orientation. This preference is the same across the channel. The shear in the flow is causing the molecules to align themselves on average about $\theta = 45°$.

The plane Poiseuille flow has a parabolic velocity profile, Figures 42-44. The shear therefore varies linearly across the channel with no shear at the center line and the highest shear at the walls. Figure 44 shows that the molecular orientation does indeed follow this pattern. The most probable angle is again $\theta = 45°$, however, the strength of the preference diminishes as the bins get closer to the center of the flow.

The molecular orientation results are consistent with the proposition that the shear affects the alignment of the molecule. There still remains the anomaly at the wall. Further simulations were performed with differing wall densities. There are 5 FCC lattice units for the fluid in the y-direction. The wall densities will be expressed in y-axis lattice units for comparison. For Figures 45 and 46 the density was 10, for Figures 47 and 48 it was 8, for Figures 39-41 already shown it was 7, and for Figures 49 and 50 it was 6. A value of 5 for the wall density allowed fluid particles to escape through the wall. A value of 7 was chosen as the optimum density for the bulk of the molecular simulations.

These figures suggest that decreasing the wall density decreased the slip, that is to say, the fluid velocity more nearly matched the wall velocity. Decreasing the wall density also reduced the strength of the preference of the molecules near the

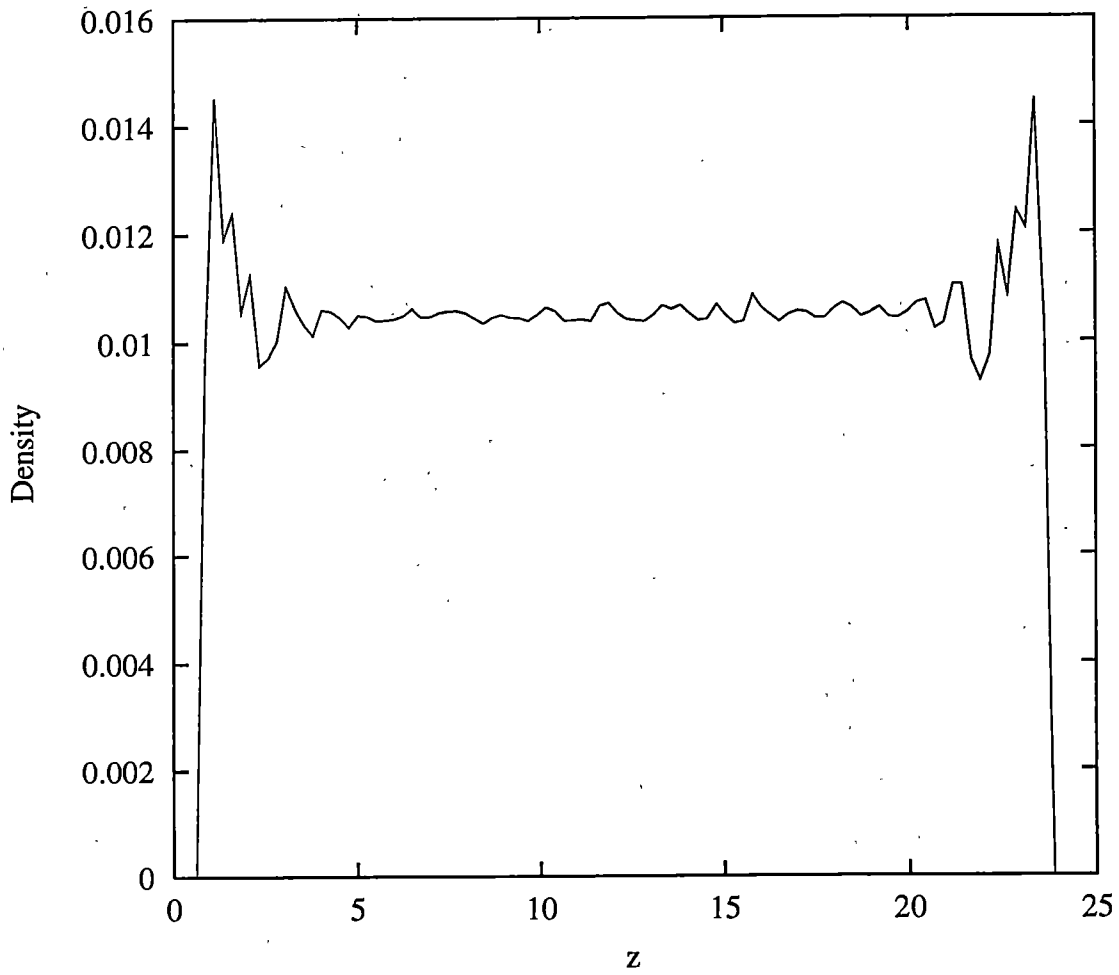

Figure 39. Density profile for the 2000 molecule plane Couette flow.

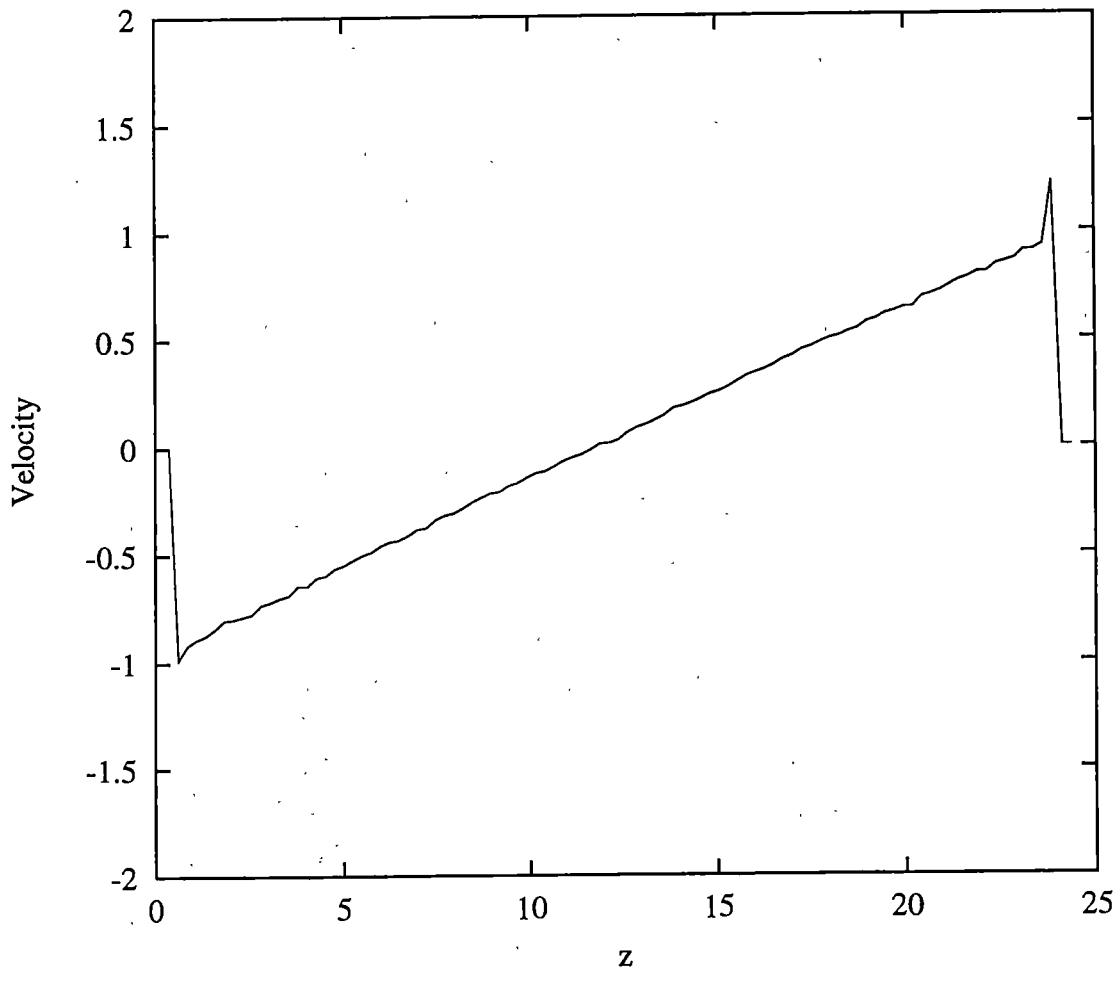

Figure 40. Velocity profile for the 2000 molecule plane Couette flow.

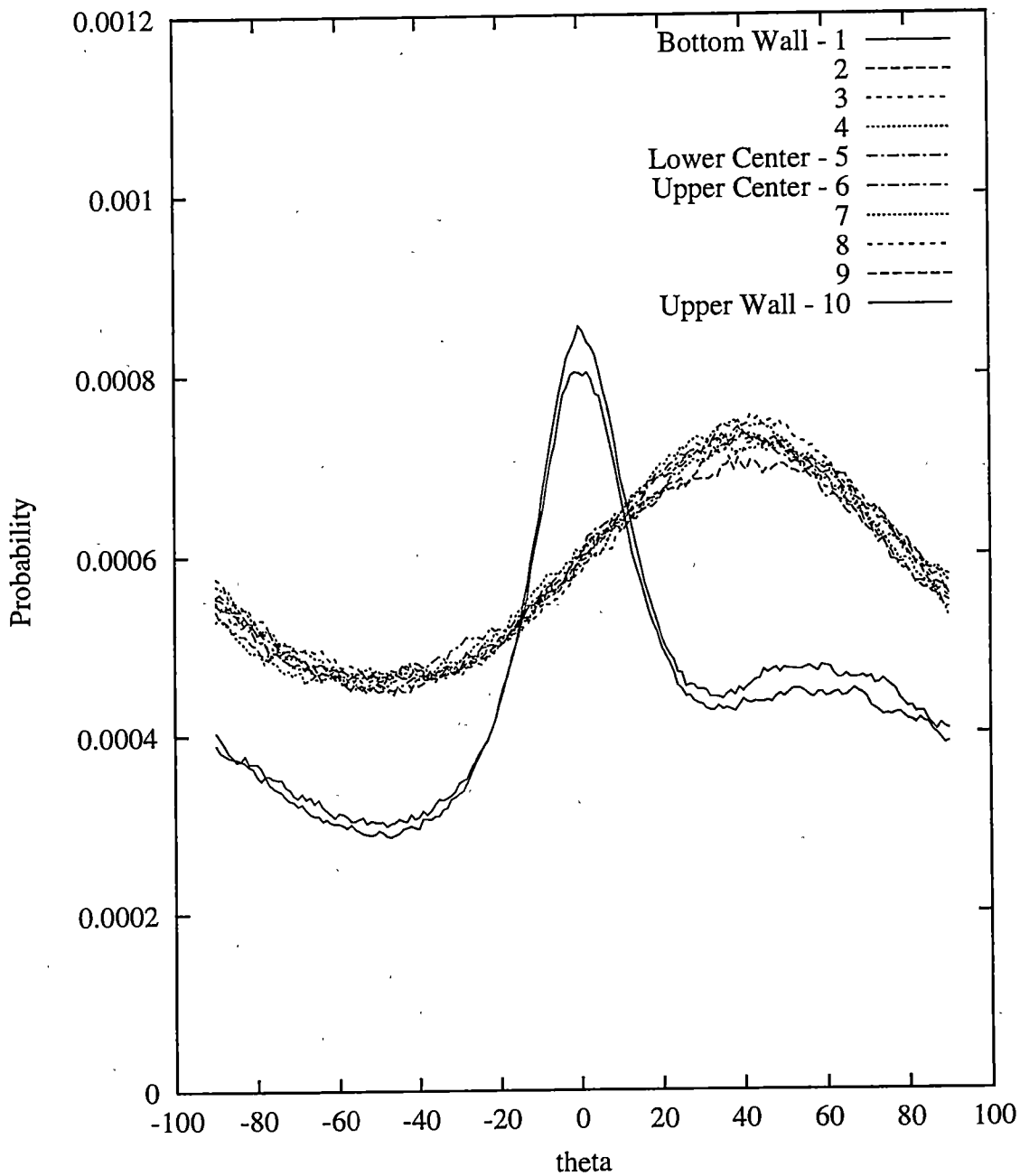

Figure 41. Angular distribution for the 2000 molecule plane Couette flow.

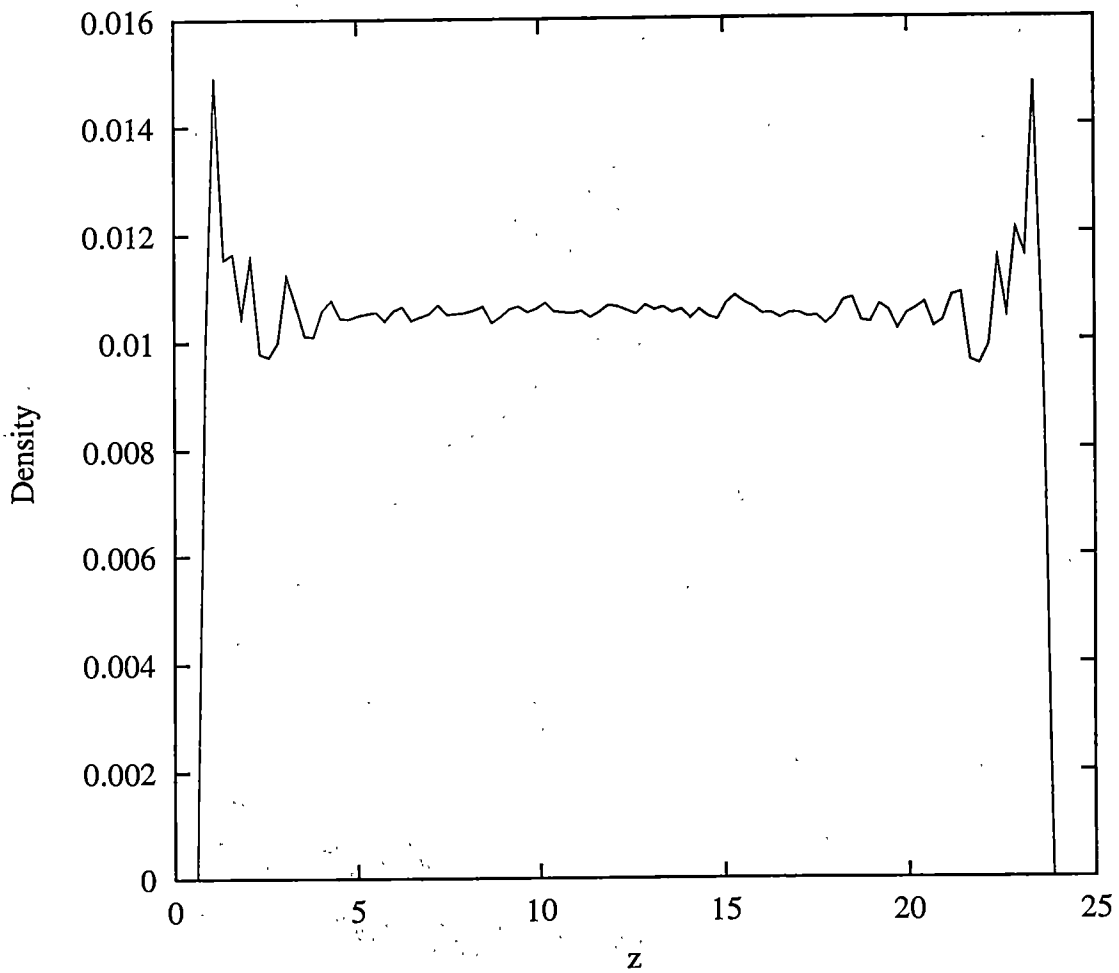

Figure 42. Density profile for the 2000 molecule plane Poiseuille flow.

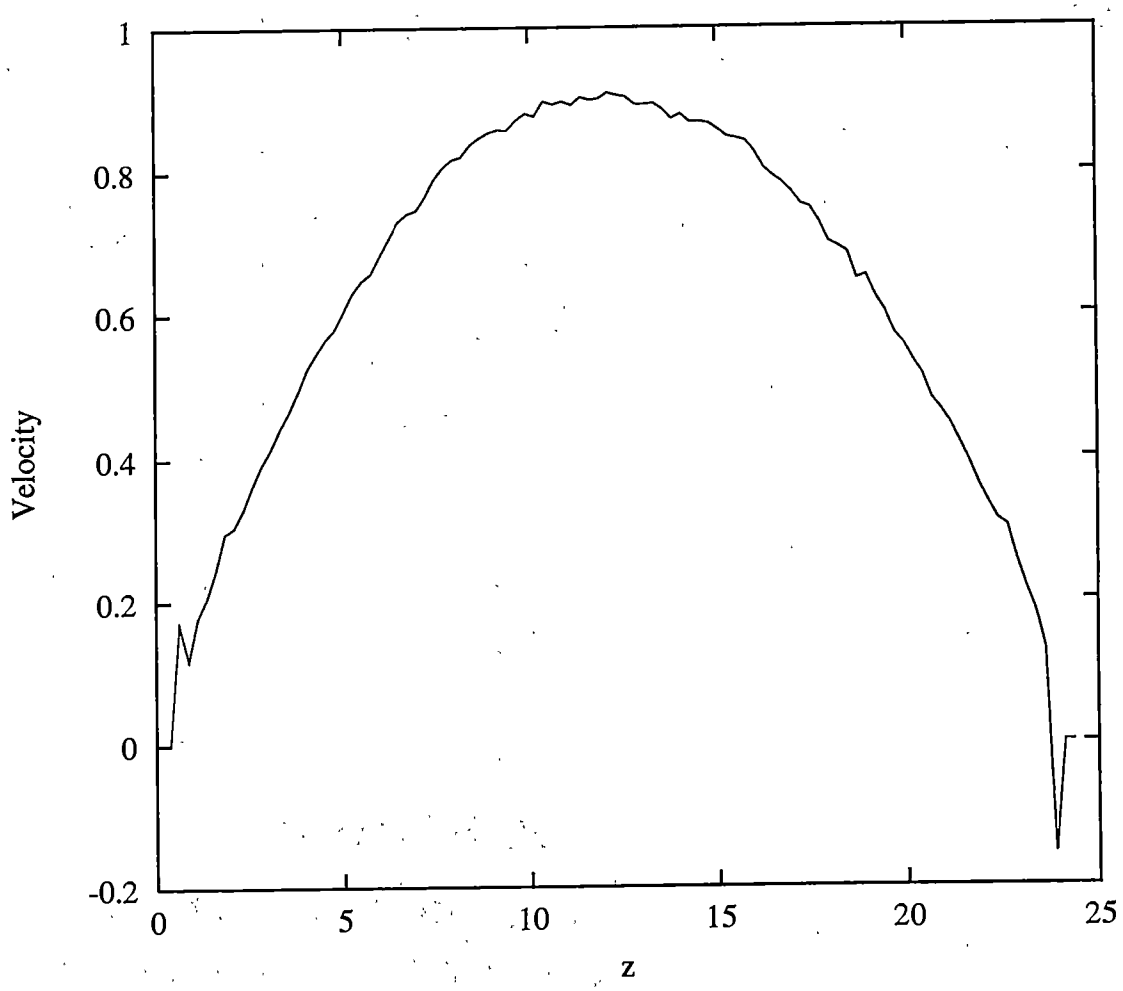

Figure 43. Velocity profile for the 2000 molecule plane Poiseuille flow.

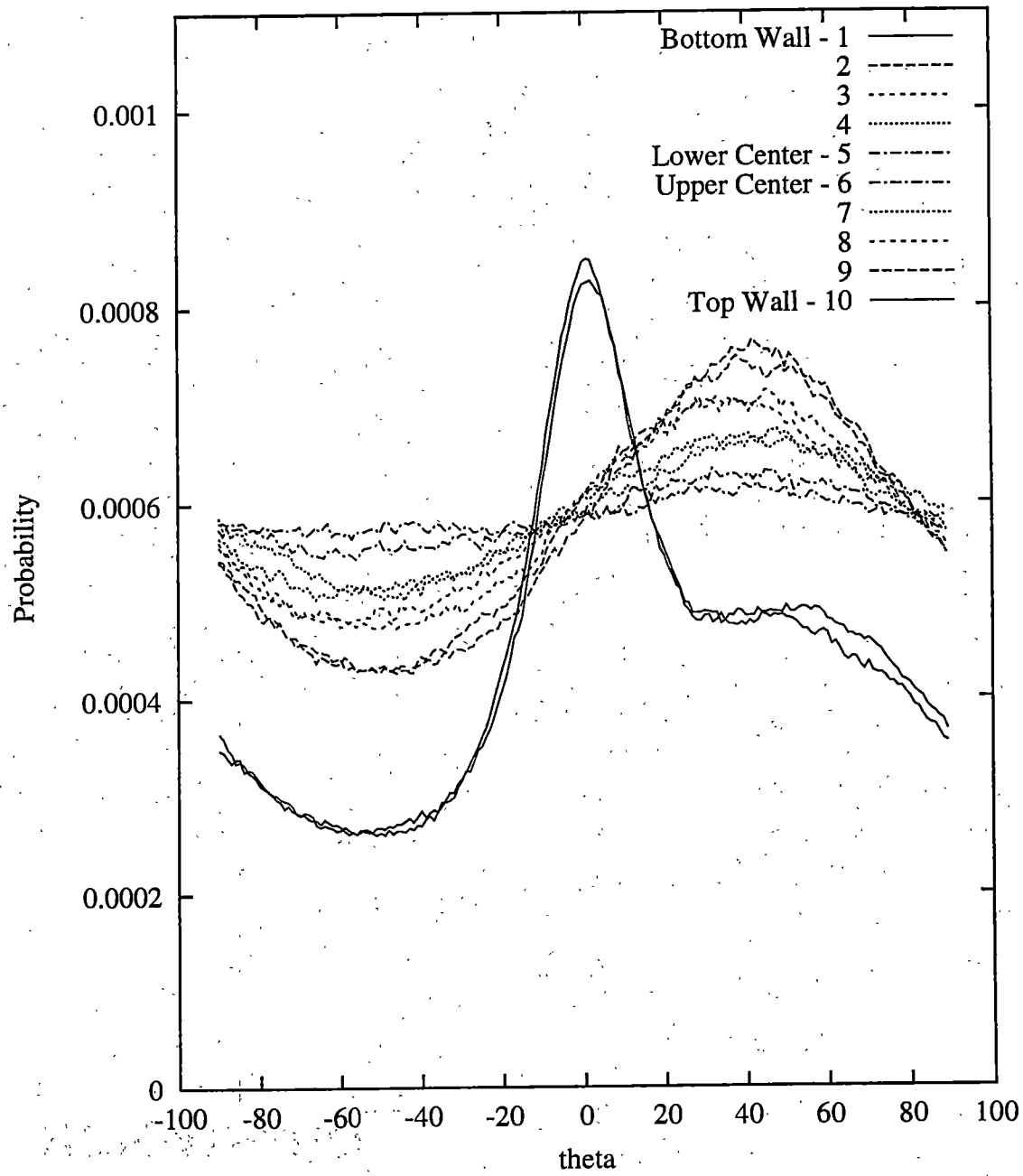

Figure 44. Angular distribution for the 2000 molecule plane Poiseuille flow.

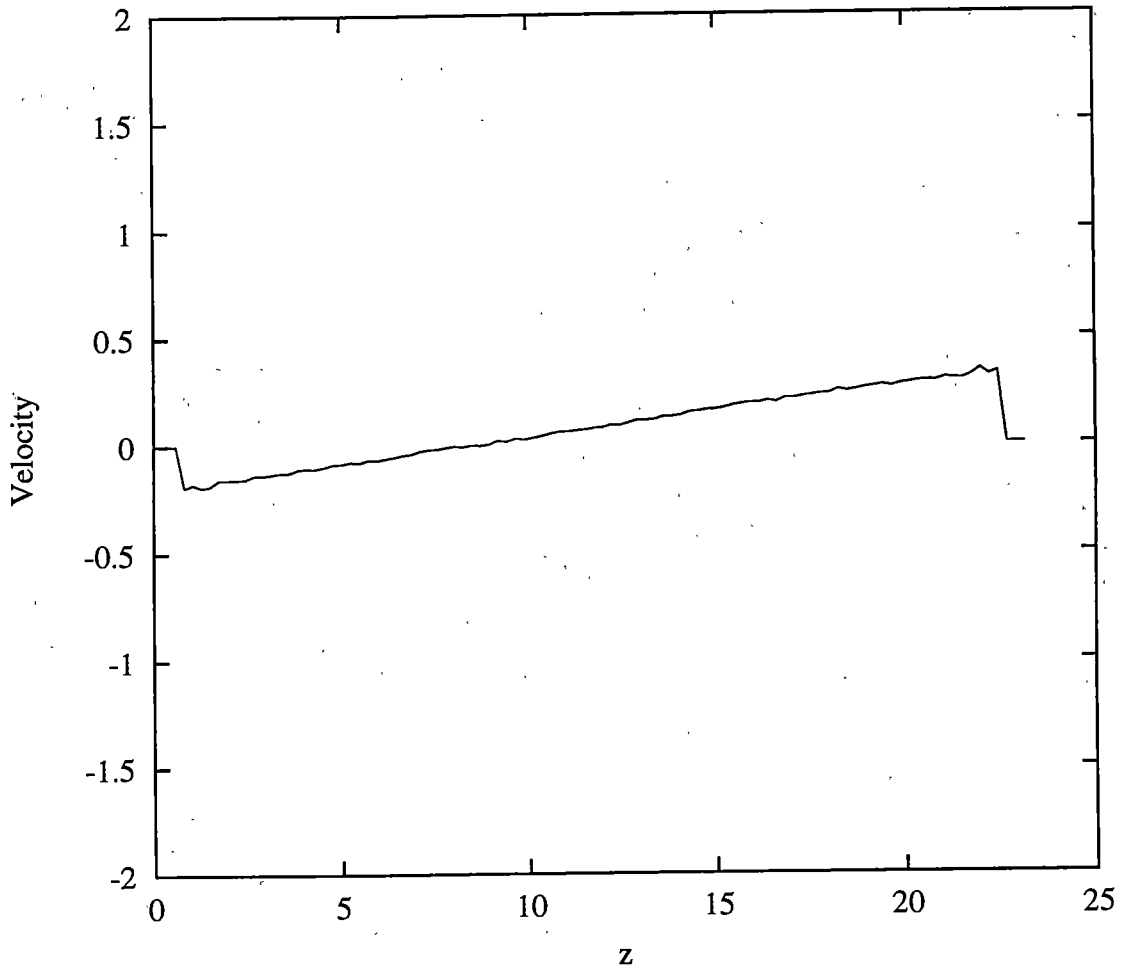

Figure 45. Velocity profile for the 2000 molecule plane Couette flow with wall density 10.

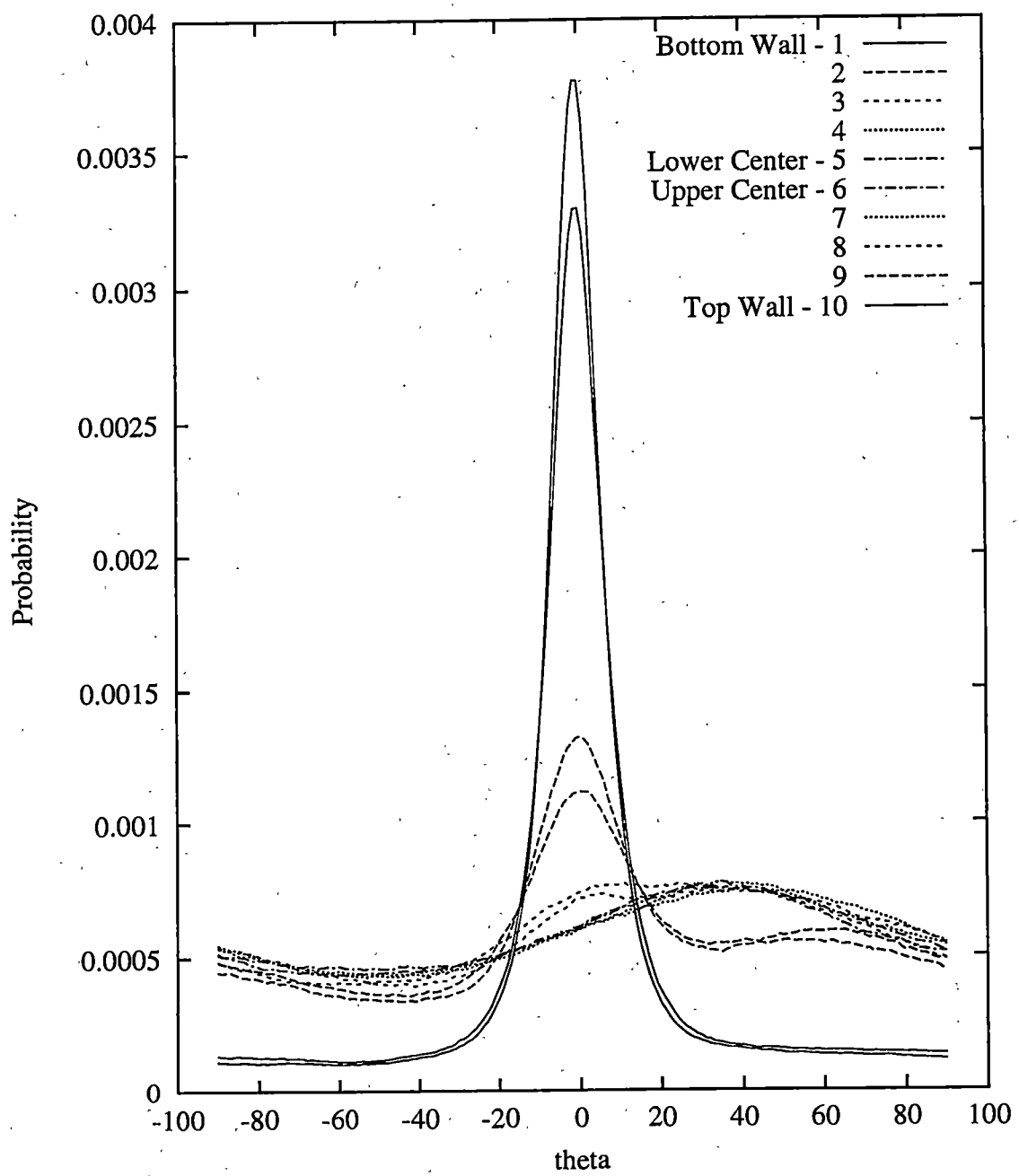

Figure 46. Angular distribution for the 2000 molecule plane Couette flow with wall density 10.

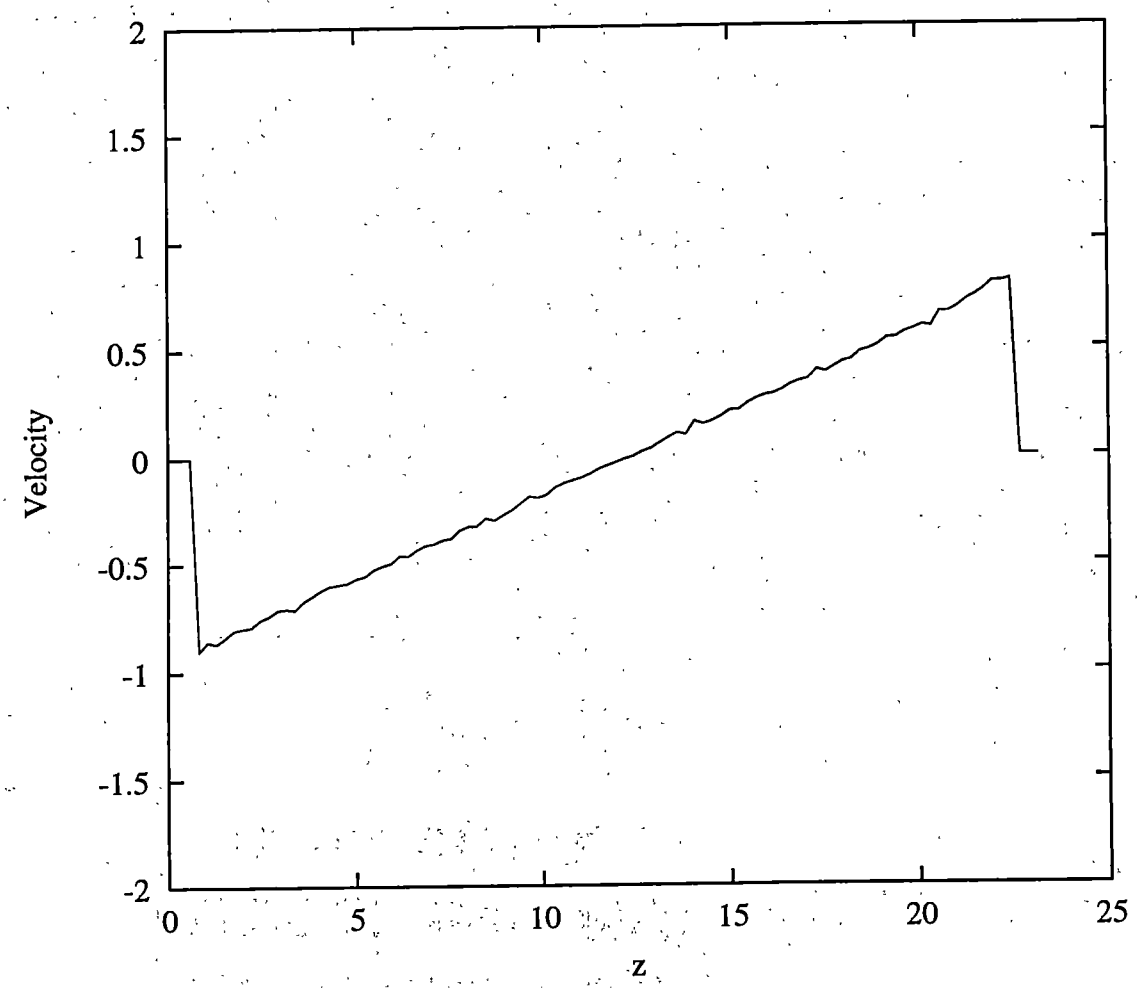

Figure 47. Velocity profile for the 2000 molecule plane Couette flow with wall density 8.

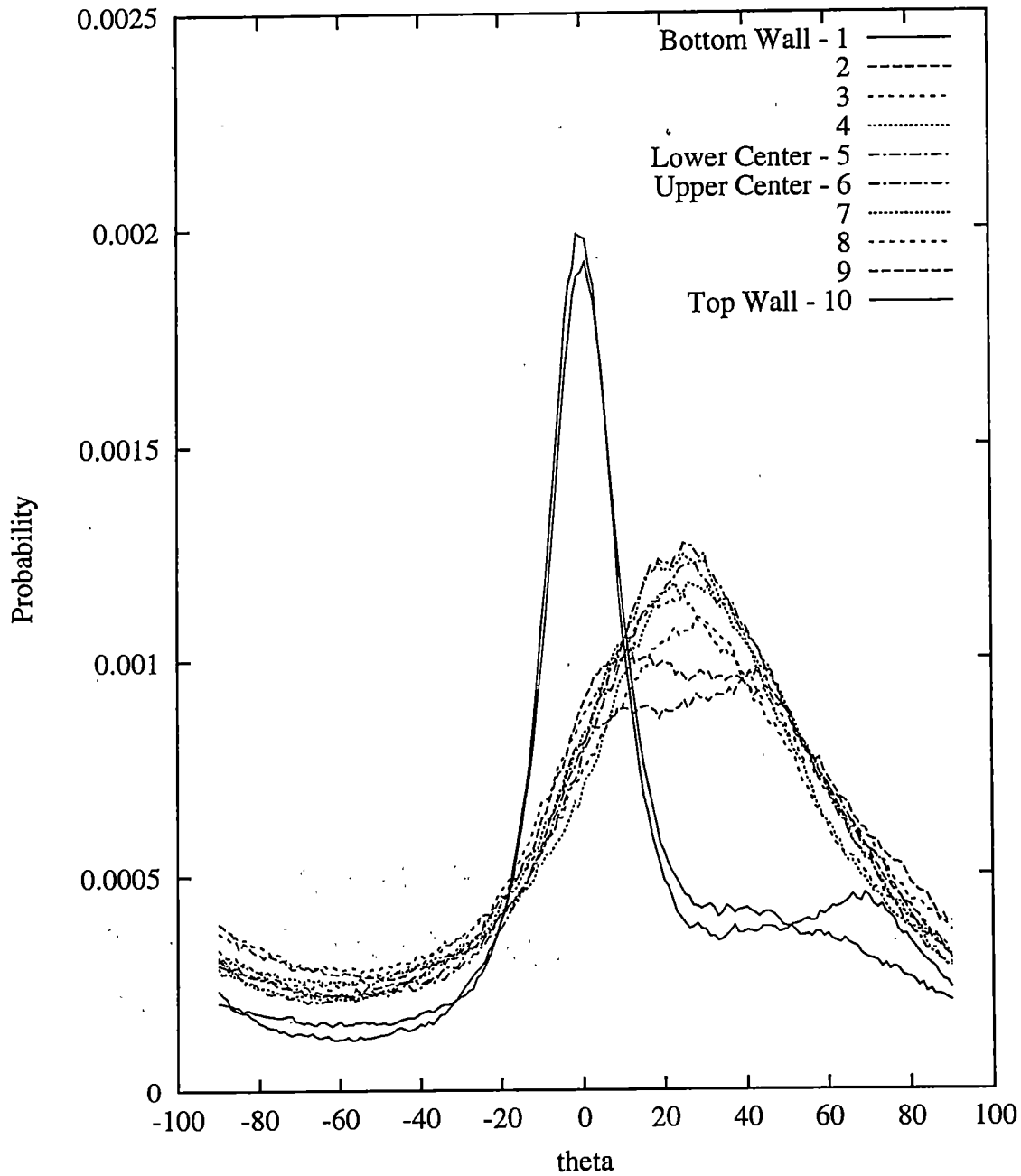

Figure 48. Angular distribution for the 2000 molecule plane Couette flow with wall density 8.

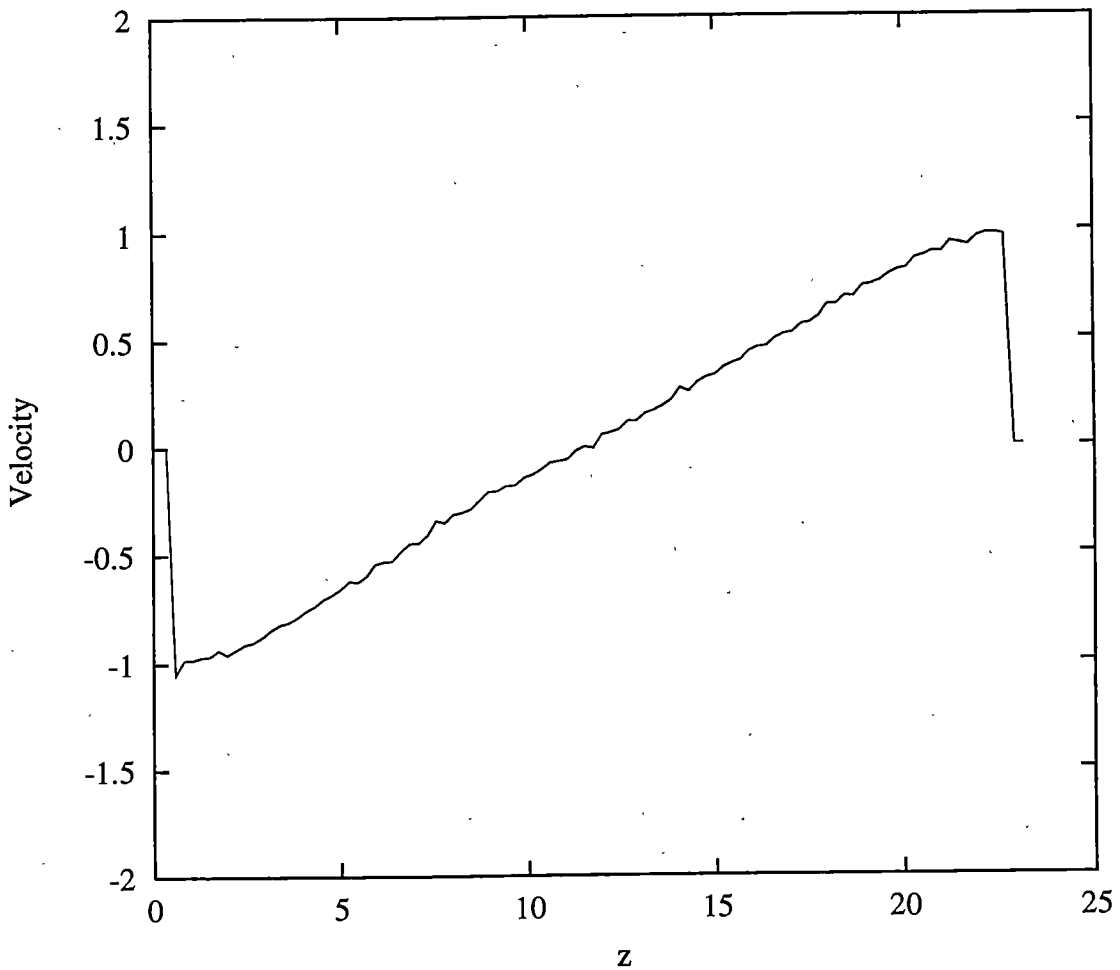

Figure 49. Velocity profile for the 2000 molecule plane Couette flow with wall density 6.

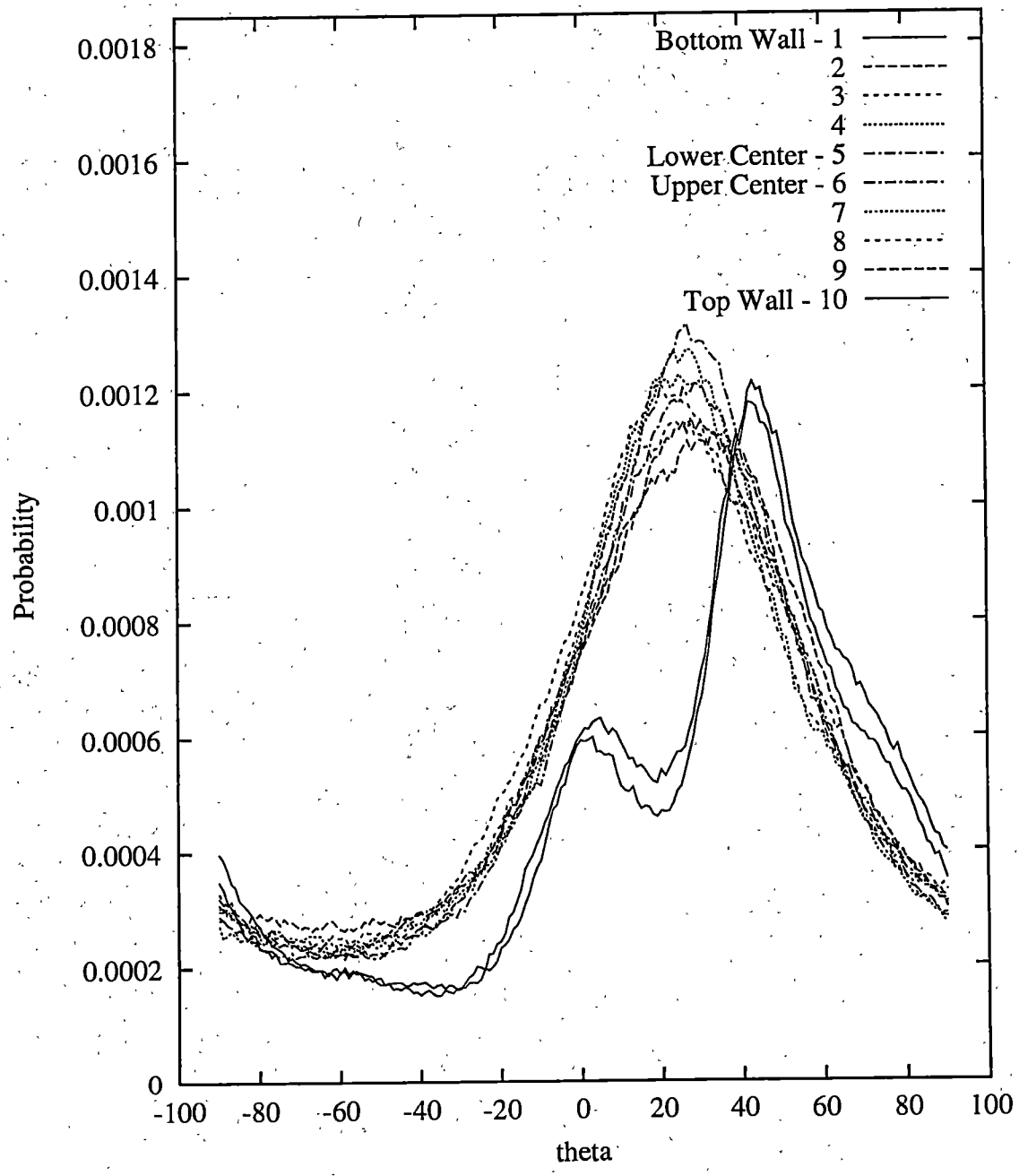

Figure 50. Angular distribution for the 2000 molecule plane Couette flow with wall density 6.

wall to align about $\theta = 0°$. In fact, for the lowest density, Figure 50, two peaks are seen, the familiar $\theta = 0°$, and $\theta = 45°$ which is common to the rest of the fluid. Apparently, the more nearly the wall approximates a flat, smooth, surface, the more slip is encountered and the stronger the preference for $\theta = 0°$.

It is conjectured here that this bias is due in part to purely geometrical effects. When the choice of bin is made for a given molecule, it is based on the center of mass of that molecule. If the center of mass of a given molecule is very close to the wall, it's range of motion is restricted by the wall. Once the bin under examination is more than half the length of the molecule away, this bias should disappear.

MONOMER SOLUTION

In order to approximate the physical situation more closely, a solution of two different types of particles was examined. The solute molecules were the rod-like molecules discussed in the preceding section. The solvent particles were the monatomic spheres used previously.

Figures 51-53 are for a one to one mixture of atoms to molecules. In Figures 54-56 there are 4 times as many atoms as molecules, and in Figures 57-59 there are 4 times as many molecules as atoms. These figures show that the orientational bias for different concentrations of molecules. As the molecules concentration decreases, the strength of the orientational preference diminishes.

The width-wise resolution of the bins which monitor the angular orientation was increased to study the wall effect in more detail. Previously there were 10 bins. Figure 60 shows the first five non-empty bins closest to the wall for a simulation with 200 bins. It seems clear that the orientations available to a molecule depend directly on its distance from the wall.

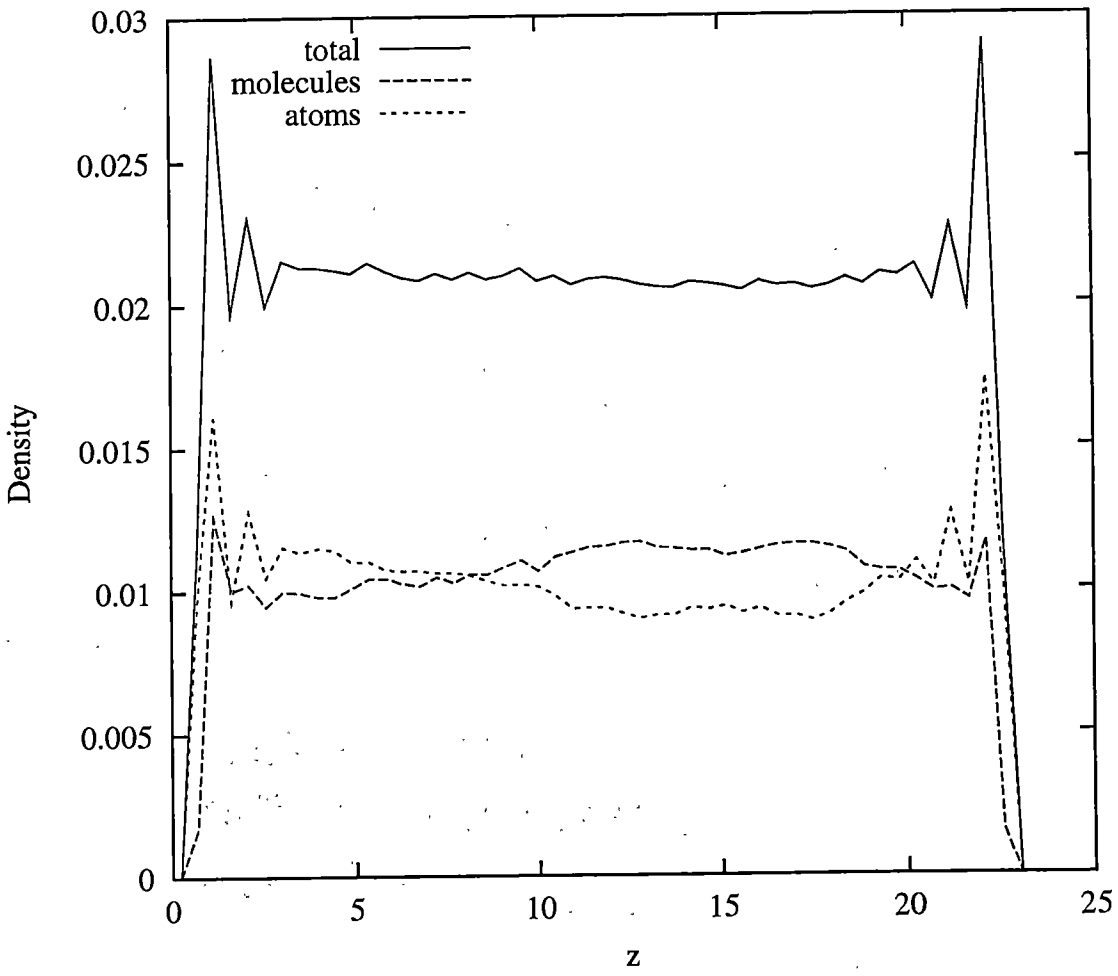

Figure 51. Density profile for the 1:1 monomer solution in plane Couette flow.

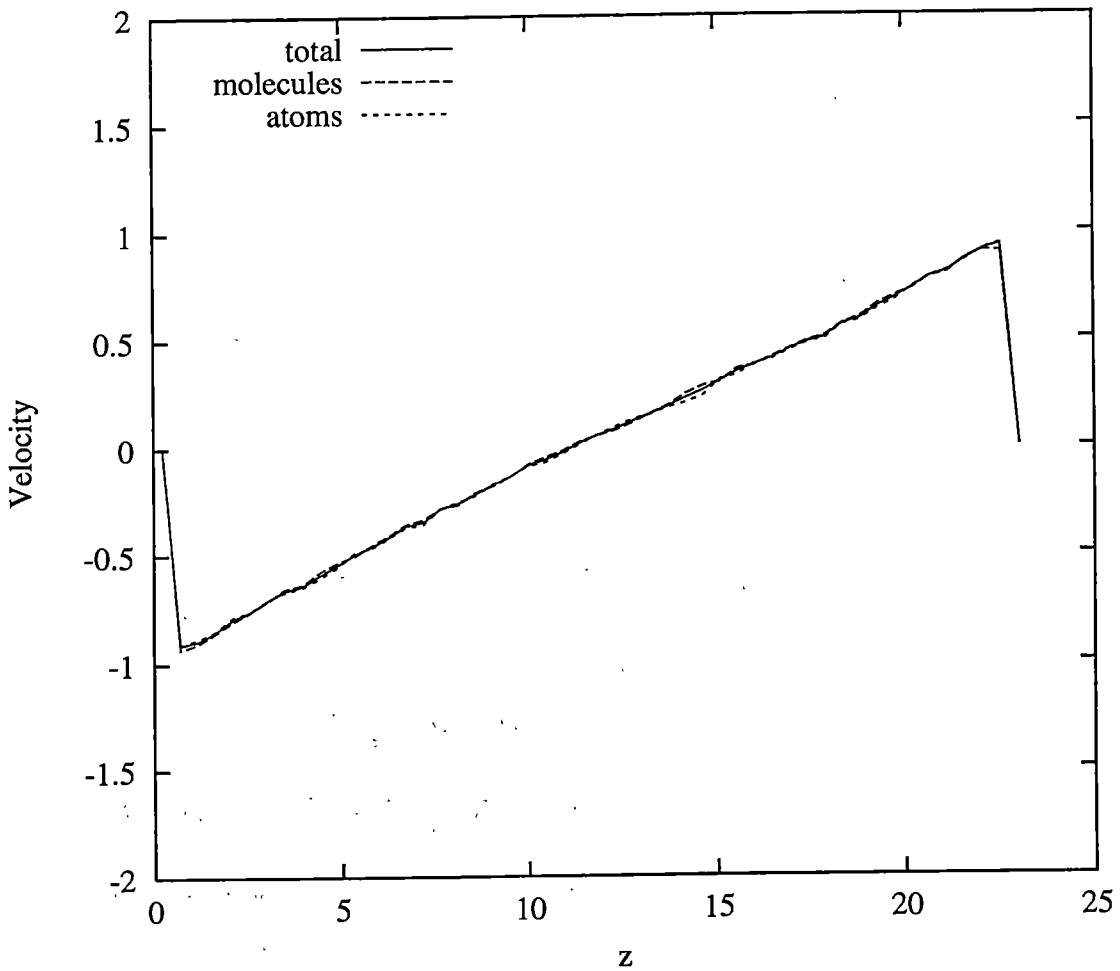

Figure 52. Velocity profile for the 1:1 monomer solution in plane Couette flow.

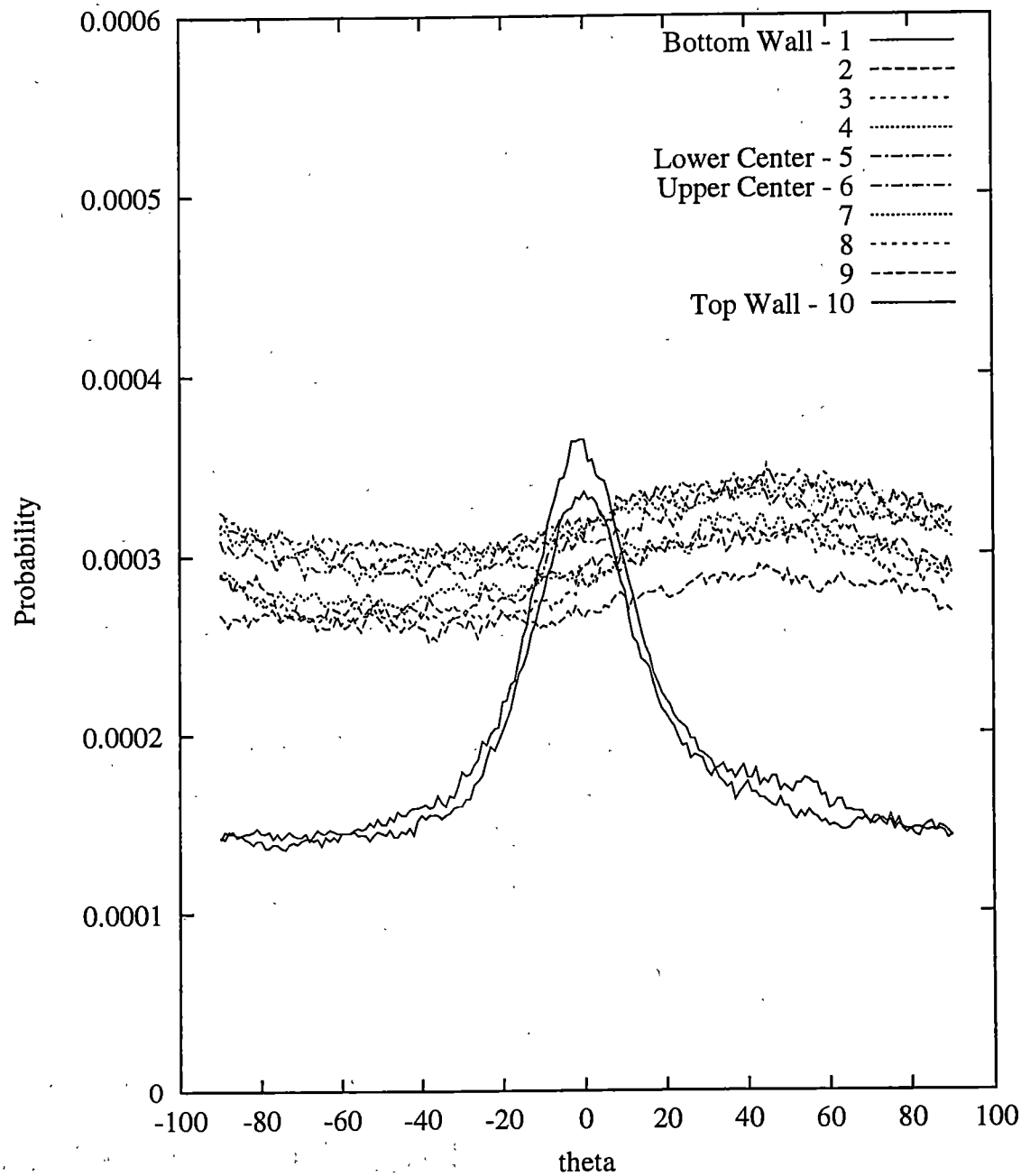

Figure 53. Angular distribution for the 1:1 monomer solution in plane Couette flow.

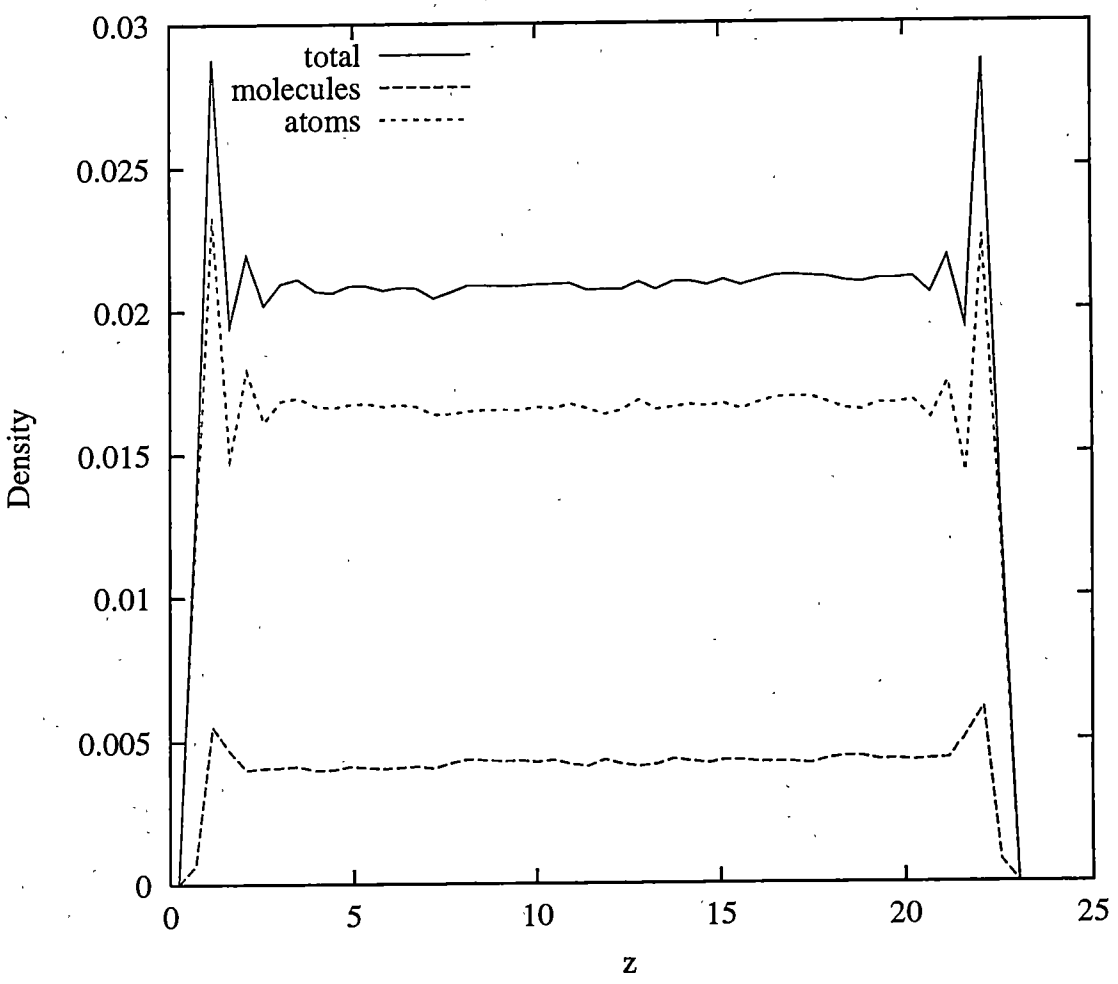

Figure 54. Density profile for the 1:4 monomer solution in plane Couette flow.

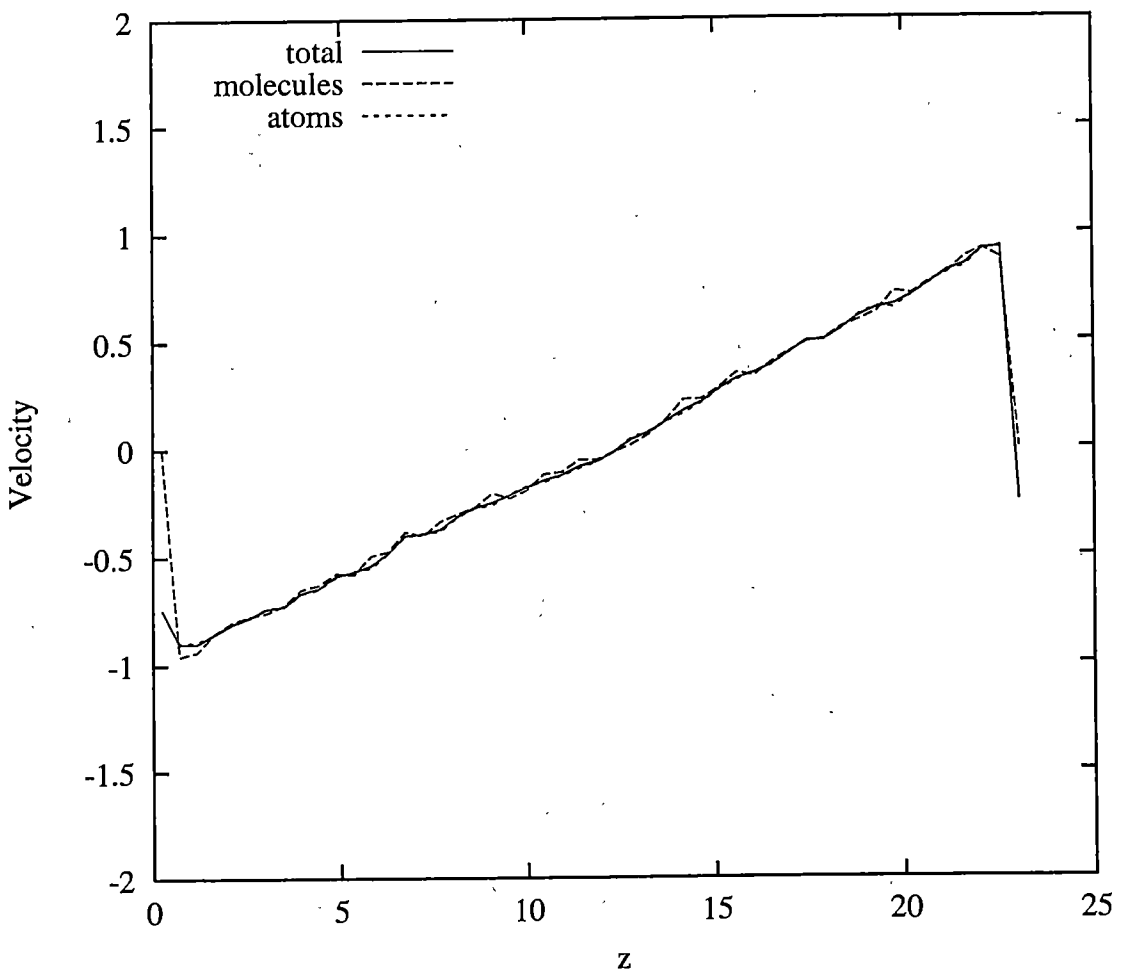

Figure 55. Velocity profile for the 1:4 monomer solution in plane Couette flow.

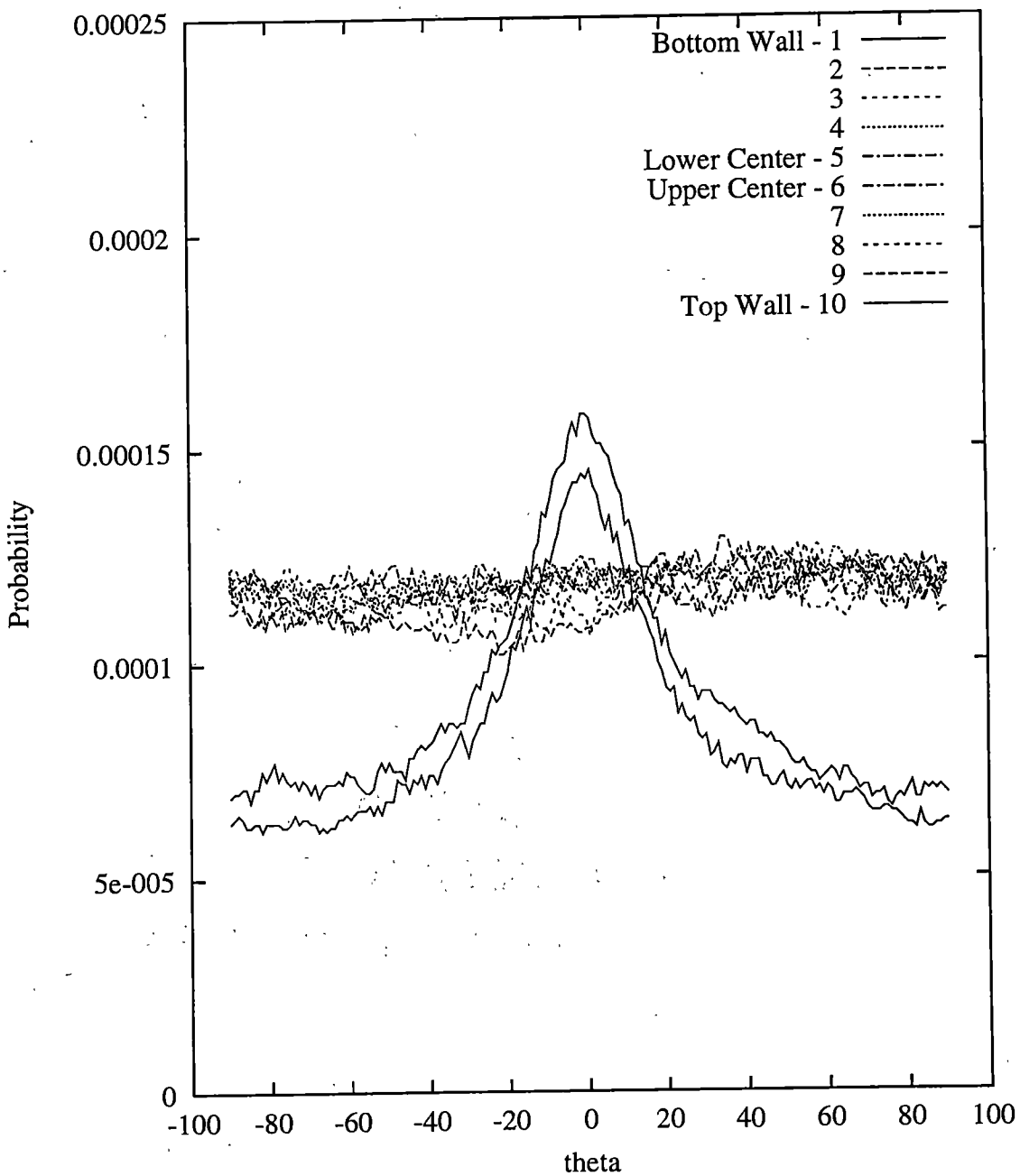

Figure 56. Angular distribution for the 1:4 monomer solution in plane Couette flow.

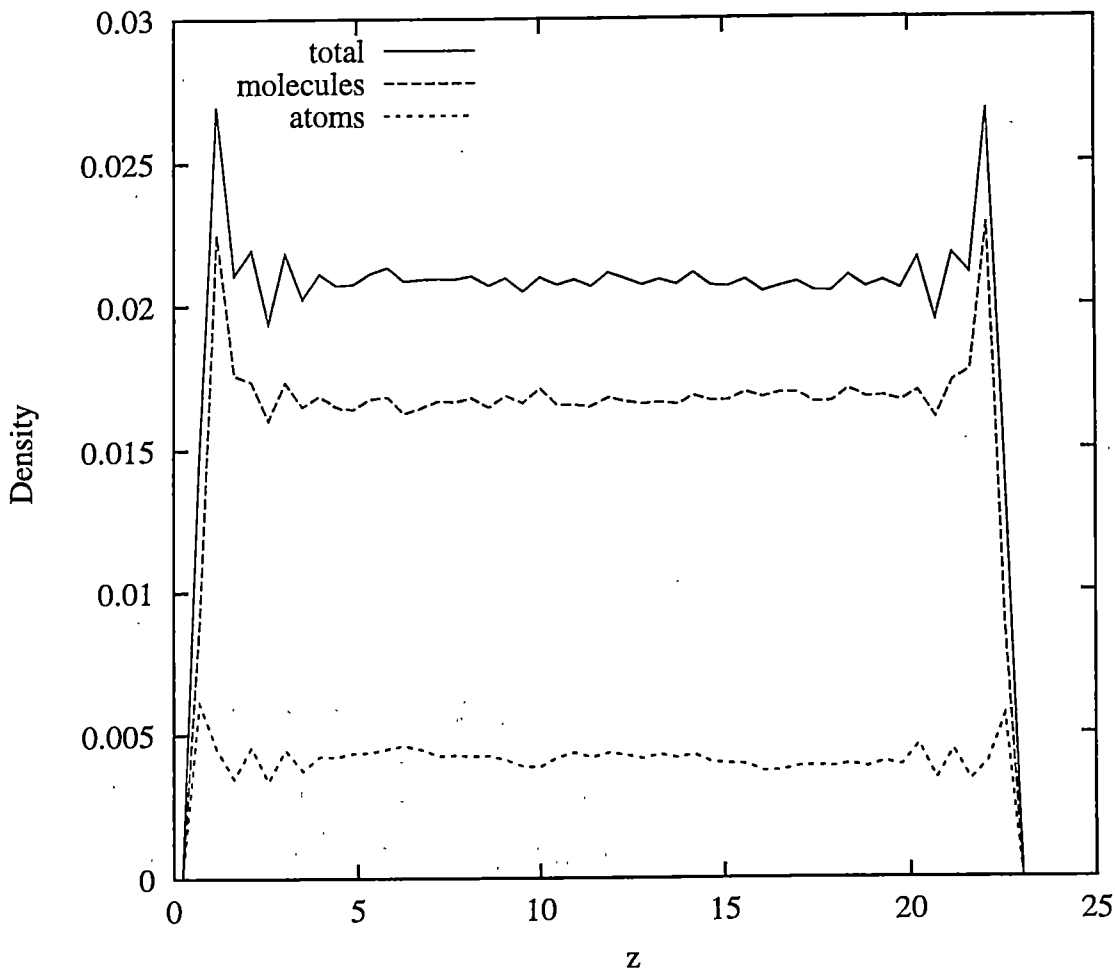

Figure 57. Density profile for the 4:1 monomer solution in plane Couette flow.

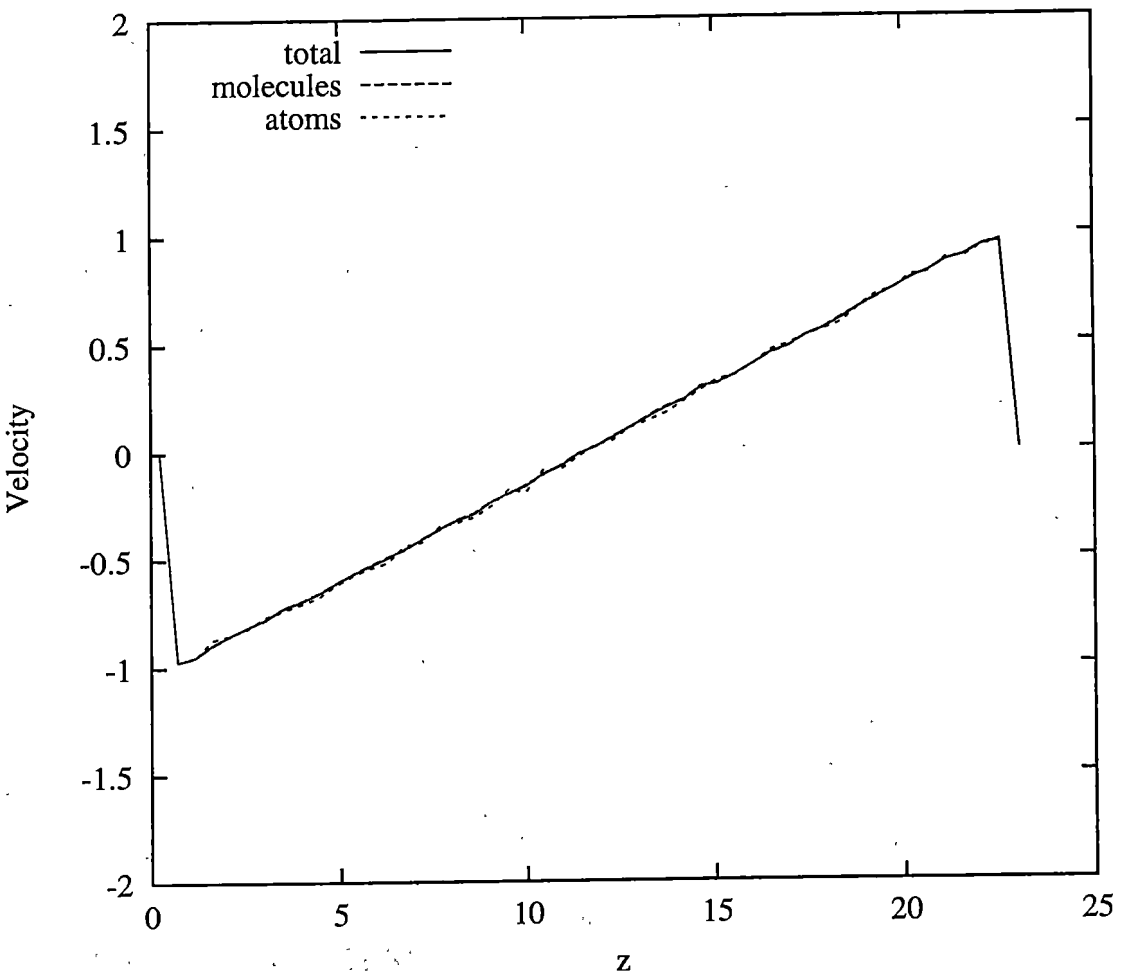

Figure 58. Velocity profile for the 4:1 monomer solution in plane Couette flow.

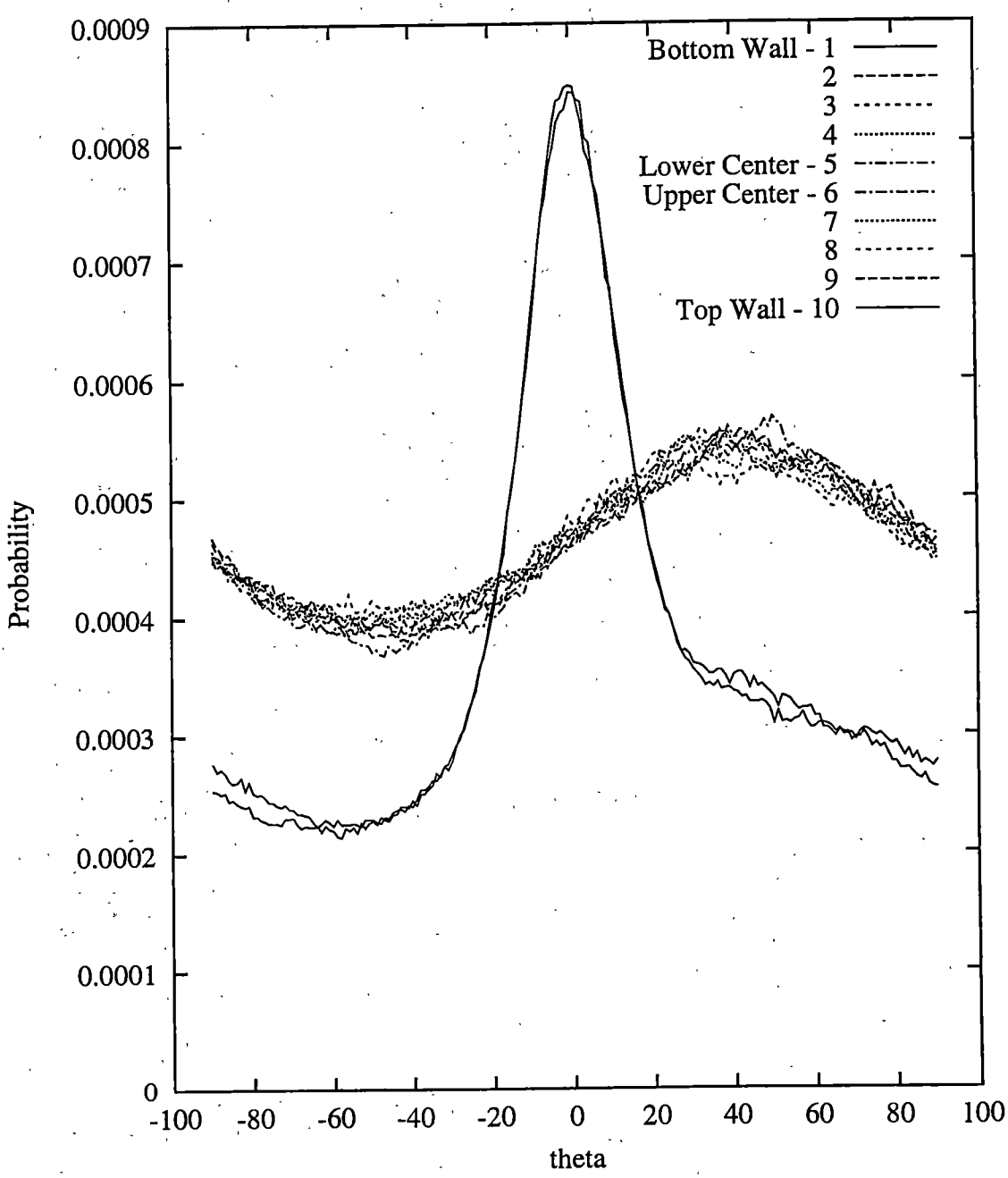

Figure 59. Angular distribution for the 4:1 monomer solution in plane Couette flow.

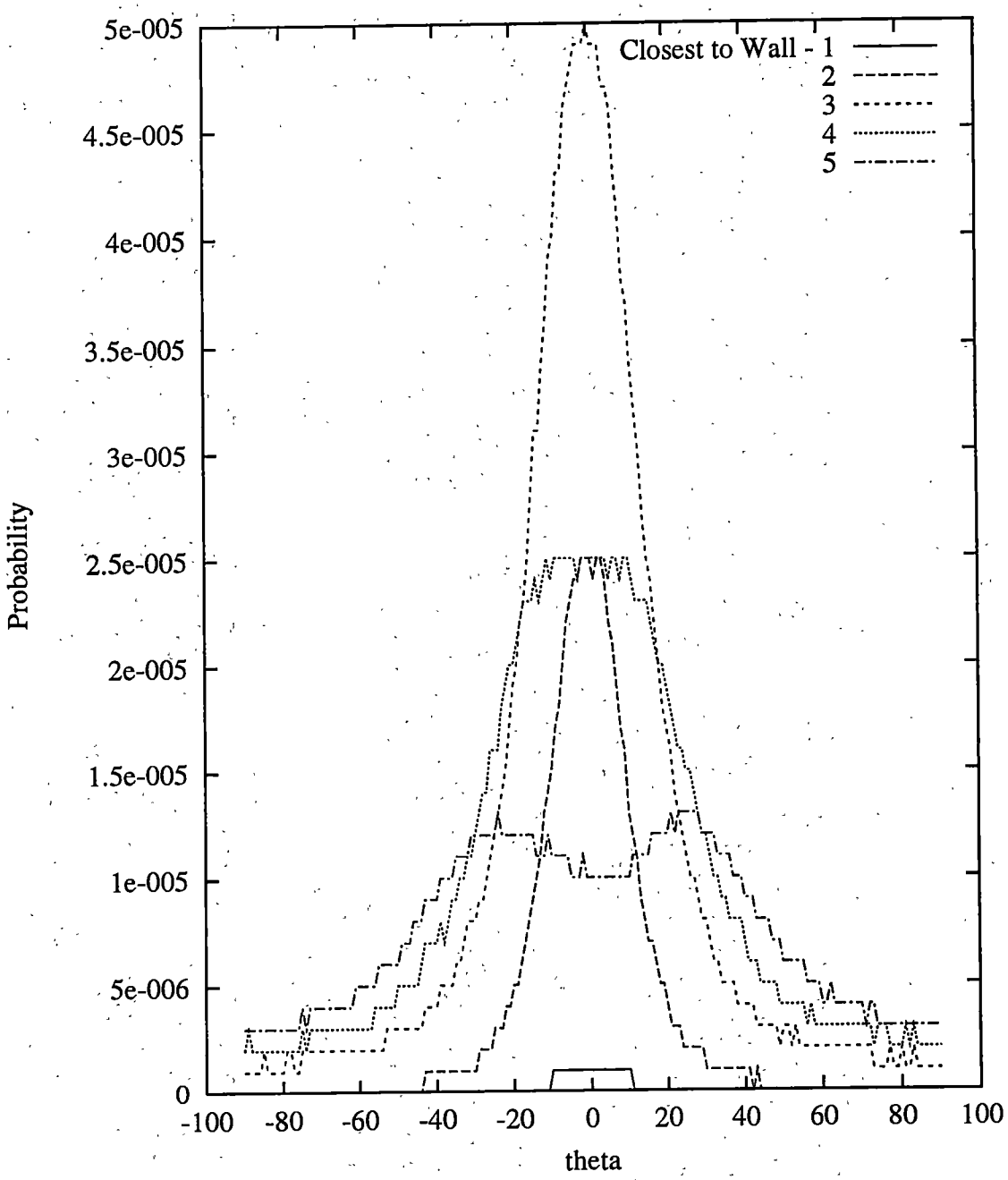

Figure 60. High resolution angular distribution for the 1:4 monomer solution in plane Couette flow.

Finally, the results of the plane Poiseuille flow with 4 atoms per molecule are shown at the higher bin resolution in Figures 61-63. Even though the lower concentration shows less orientational bias in general, the wall effect is still quite pronounced.

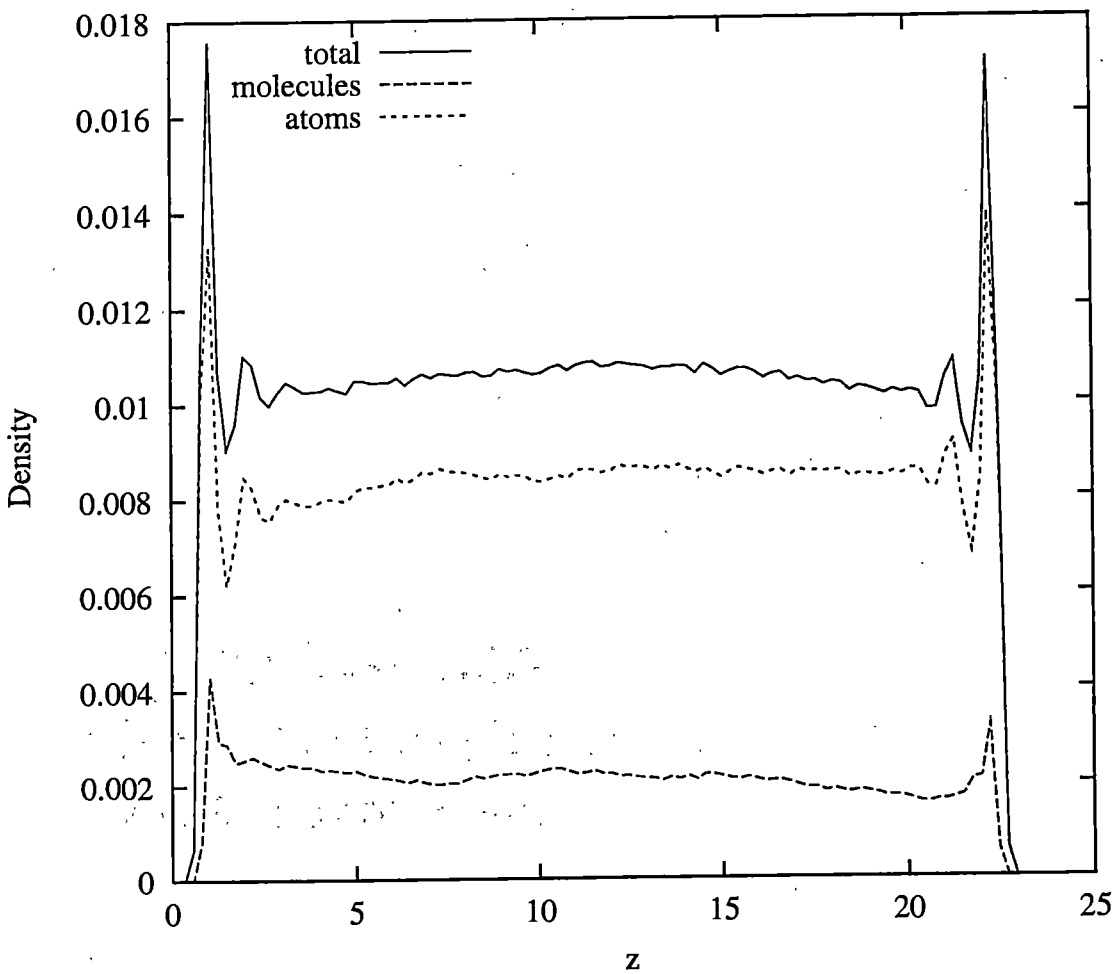

Figure 61. Density profile for the 1:4 monomer solution in plane Poiseuille flow.

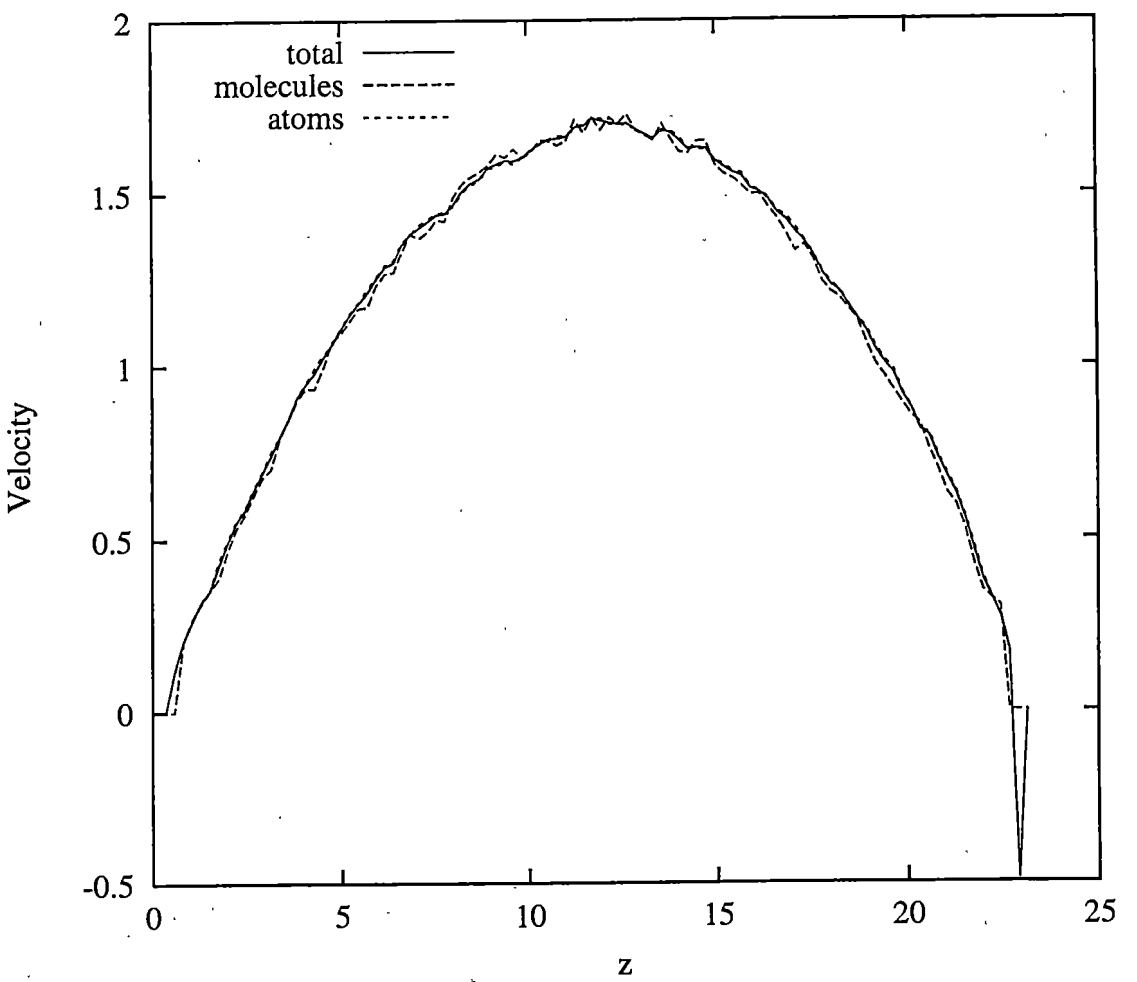

Figure 62. Velocity profile for the 1:4 monomer solution in plane Poiseuille flow.

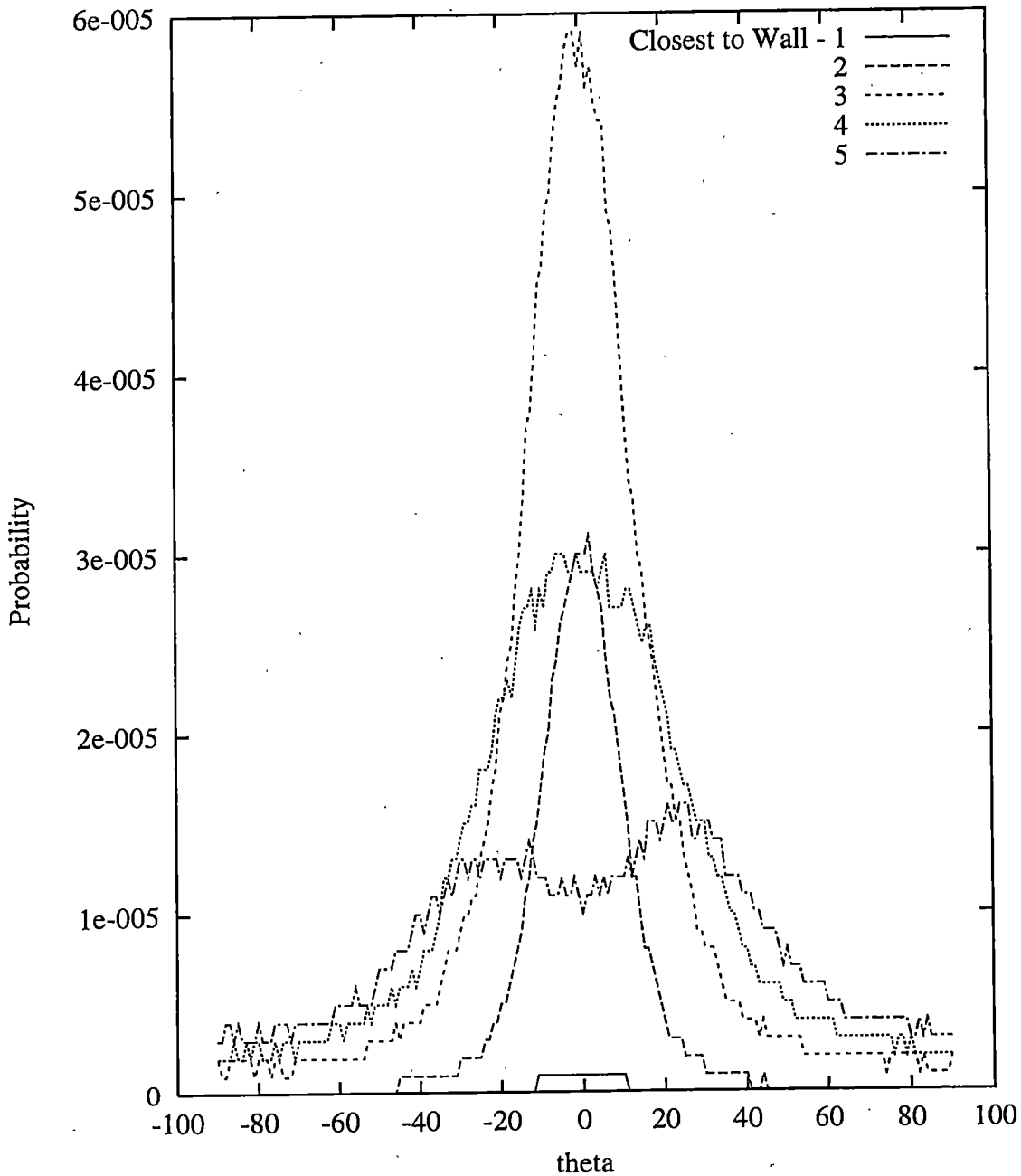

Figure 63. Angular distribution for the 1:4 monomer solution in plane Poiseuille flow.

CHAPTER 7: CONCLUSIONS AND FUTURE WORK

Using three flows of differing shear it has been shown that the molecular orientation of rod-like molecules is indeed affected by the shear. How these results can be extended to the physical model is not entirely clear, however.

It was shown that a lower concentration of molecules in a solution decreases the orientational preference of the molecules. In the physical solution the concentrations will be much lower than those used in the simulation. The flows used in the models were also much faster than will be experienced in the physical phenomenon. Both of these factors suggest that the shear effect would be reduced.

These influences are balanced, however, by other approximations that were made. The physical polymers are much longer than the molecules used in the simulations. There may also be ionic charges on both the fluid and the wall molecules. The effect of these forces may possibly overshadow the results seen so far.

Finally, the most important region of influence is near the wall. This is where the alignment of the molecules will affect how they attach to the wall. It was shown that other factors may completely dominate the effects of shear in this region. The results indicate that the density of the wall is an important factor. When the structure and constitution of the wall are taken into account the physical proximity to the wall may overwhelm the effects of the shear.

This study has been a preliminary investigation and the program was developed in such a way as to facilitate closer approximations of the physical model. Future work would include the following:

- Further investigation into the alignment phenomenon at the wall. An explanation has been conjectured in this study, but more work is required to fully

understand the phenomenon. A theoretical analysis of the problem would also be much more satisfying.

- More accurate representations of the molecules including such factors as their size, configuration, and possible ionic charges. More sophisticated models for the solution molecules, such as TIP4P for water [28], would enhance the accuracy of the simulation.

- More accurate representation of the wall molecules. A crystalline structure appropriate to the proper molecules should be employed. The wall molecules should also be permitted to respond appropriately to the fluid by modeling the typical vibrations in the crystal. This would also facilitate the use of the wall as the thermostat mechanism. In most physical situations the wall is considered to be the means of removing the energy generated in the flow if constant temperature is to be maintained.

- A mechanism which would provide for the attachment of the molecules to the wall. This would provide direct insight into the question at hand. This would also open new avenues of investigation, an example of which could be the change in growth kinetics when a mono-layer of molecules has attached to the wall.

The preceding suggestions already demand an increase in computational resources. In addition to these needs, the simulation could be expanded in both space and time. This would reduce the need for such a high velocity flow. It may also provide insight into phenomena which require more time or space to develop.

REFERENCES

[1] Frazier, D. O., Penn, B. G., Smith, D. D., Witherow, W. K., Paley, M. S., and Abdeldayem, H. A., "Microgravity Processing and Photonic Application of Organic and Polymeric Materials", *Photonic Polymer Systems: Fundamentals, Methods and Applications*, Marcel-Dekker Inc., New York, (1997) 693-735.

[2] Hui, D., Kim, J.-S., Kim, Y.-T., An, I., and Paley, M. S., "Monitoring Photodeposition of Polydiacetylene Films from Monomer Solution Using In Situ Real-Time Spectroscopic Ellipsometry", *Communication* (1999).

[3] Koplik, J., "Molecular Dynamics of Fluid Flow", *Research Trends in Fluid Dynamics*, AIP Press (1996) 118-128.

[4] Goldstein, H., *Classical Mechanics* Addison-Wesley, Reading Massachusetts (1981).

[5] Gombosi, T. I., *Gaskinetic Theory* Cambridge University Press, Cambridge, England (1994).

[6] Alder, B. J., and Wainwright, T. E., "Studies in Molecular Dynamics. I. General Method", *Journal of Chemical Physics* **31** (1959) 459-466.

[7] Alder, B. J., and Wainwright, T. E., "Studies in Molecular Dynamics. II. Behavior of a Small Number of Elastic Spheres", *Journal of Chemical Physics* **33** (1960) 1439-1451.

[8] Alder, B. J., "Studies in Molecular Dynamics. III. A Mixture of Hard Spheres", *Journal of Chemical Physics* **40** (1963) 2724-2730.

[9] Hoover, W. G., and Alder, B. J., "Studies in Molecular Dynamics. IV. The Pressure, Collision Rate, and Their Number Dependence for Hard Disks", *Journal of Chemical Physics* **46** (1967) 686-691.

[10] Alder, B. J., Hoover, W. G., and Young, D. A., "Studies in Molecular Dynamics. V. High-Density Equation of State and Entropy for Hard Disks and Spheres", *Journal of Chemical Physics* **49** (1968) 3688-3696.

[11] Einwohner, T. J., and Alder, B. J., "Molecular Dynamics. VI. Free-Path Distributions and Collision Rates for Hard-Sphere and Square-Well Molecules", *Journal of Chemical Physics* **49** (1968) 1458-1473.

[12] Alder, B. J., and Hecht, C. E., "Studies in Molecular Dynamics. VII. Hard-Sphere Distribution Functions and an Augmented van der Waals Theory", *Journal of Chemical Physics* **50** (1969) 2032-2037.

[13] Alder, A. J., Gass, D. M., and Wainwright, T. E., "Studies in Molecular Dynamics. VIII. The Transport Coefficients for a Hard-Sphere Fluid", *Journal of Chemical Physics* **53** (1970) 3813-3826.

[14] Bennett C. H., and Alder B. J., "Studies in Molecular Dynamics. IX. Vacancies in Hard Sphere Crystals", *Journal of Chemical Physics* **54** (1971) 4796-4808.

[15] Alder, B. J., Young, D. A., and Mark, M. A., "Studies in Molecular Dynamics. X. Corrections to the Augmented van der Waals Theory for the Square Well Fluid", *Journal of Chemical Physics* **56** (1972) 3013-3029.

[16] Herman, P. T., and Alder, B. J., "Studies in Molecular Dynamics. XI. Correlation Functions of a Hard-Sphere Test Particle", *Journal of Chemical Physics* **56** (1972) 987-991.

[17] Alder, B. J., Strauss, H. L., and Weis, J. J., "Studies in molecular dynamics. XII. Band shape of the depolarized light scattered from atomic fluids", *Journal of Chemical Physics* **59** (1973) 1002-1012.

[18] Young, D. A., and Alder, B. J., "Studies in molecular dynamics. XIII. Singlet and pair distribution functions for hard-disk and hard-sphere solids", *Journal of Chemical Physics* **60** (1974) 1254-1267.

[19] Alder, B. J., Alley, W. E., and Dymond, J. H., "Studies in molecular dynamics. XIV. Mass and size dependence of the binary diffusion coefficient", *Journal of Chemical Physics* **61** (1974) 1415-1420.

[20] Alley, W. E., and Alder, B. J., "Studies in molecular dynamics. XV. High temperature description of the transport coefficients", *Journal of Chemical Physics* **63** (1975) 3764-3768.

[21] Alley, W. E., and Alder, B. J., "Studies in molecular dynamics. XVI. Fluctuation driven resonance", *Journal of Chemical Physics* **66** (1977) 2631-2637.

[22] Young, D. A., and Alder, B. J., "Studies in molecular dynamics. XVII. Phase diagrams for 'step' potentials in two and three dimensions", *Journal of Chemical Physics* **70** (1979) 473-481.

[23] Young, D. A., and Alder, B. J., "Studies in molecular dynamics. XVIII. The square-well phase diagram", *Journal of Chemical Physics* **73** (1980) 2430-2434.

[24] Hansen, J. P., and McDonald, I. R., *Theory of Simple Liquids* Academic Press, San Diego, California (1986).

[25] Hockney, R. W., *Computer Simulation Using Particles* Institute of Physics Publishing, Philadelphia, Pennsylvania (1988).

[26] Allen, M. P., and Tildesley, D. J., *Computer Simulation of Liquids* Oxford University Press, New York, New York (1987).

[27] Haile, J. M., *Molecular Dynamics Simulation: Elementary Methods* John Wiley & Sons, New York, New York (1992).

[28] Rapaport, D. C., *The Art of Molecular Dynamics Simulation* Cambridge University Press, New York, New York (1997).

[29] Evans, D. J., "Computer 'experiment' for nonlinear thermodynamics of Couette flow", *Journal of Chemical Physics* **78** (1983) 3297-3302.

[30] Padilla, P., and Toxvaerd, S., "Simulating shear flow", *Journal of Chemical Physics* **104** (1996) 5956-5963.

[31] Morriss, G. P., and Evans, D. J., "Application of transient correlation functions to shear flow far from equilibrium", *Physical Review A* **35** (1987) 792-797.

[32] Robbins, M. O., and Thompson, P. A., "Molecular Dynamics Simulations of Contact Line Motion", *Materials Research Society Symposium Proceedings* **177** (1990) 411-422.

[33] Thompson, P. A., and Robbins, M. O., "Simulations of Contact-Line Motion: Slip and the Dynamics Contact Angle", *Physical Review Letters* **63** (1989) 766-769.

[34] Koplik J., Banavar, J. R., and Willemsen, J. F., "Molecular dynamics of fluid flow at solid surfaces", *Physics of Fluids A* **1** (1989) 781-794.

[35] Heinbuch, U., and Fischer, J., "Liquid flow in pores: Slip, no-slip, or multilayer sticking", *Physical Review A* **40** (1989) 1144-1146.

[36] Koplik, J., Banavar, J. R., and Willemsen, J. F., "Molecular Dynamics of Poiseuille Flow and Moving Contact Lines", *Physical Review Letters* **60** (1988) 1282-1285.

[37] Thompson, P. A., and Robbins, M. O., "Shear flow near solids: Epitaxial order and flow boundary conditions", *Physical Review A* **41** (1990) 6830-6837.

[38] Bitsanis, I., Magda, J. J., Tirrell, M., and Davis, H. T., "Molecular dynamics of flow in micropores", *Journal of Chemical Physics* **87** (1987) 1733-1750.

[39] Khare, R., de Pable, J., and Yethiraj, A., "Molecular simulation and continuum mechanics study of simple fluids in non-isothermal planar couette flows", *Journal of Chemical Physics* **107** (1997) 2589-2596.

[40] Magda J. J., Tirrell, M., and Davis, H. T., "Molecular dynamics of narrow, liquid-filled pores", *Journal of Chemical Physics* **83** (1985) 1888-1901.

[41] Travis, K. P., Todd, B. D., and Evans, D. J., "Poiseuille flow of molecular fluids", *Physica A* **240** (1997) 315-327.

[42] Hirshfeld, D., and Rapaport, D. C., "Molecular Dynamics Simulation of Taylor-Couette Vortex Formulation", *Physical Review Letters* **80** (1998) 5337-5340.

[43] Rapaport, D. C., "Molecular-Dynamics Study of Rayleigh-Benard Convection", *Physical Review Letters* **60** (1988) 2480-2483.

[44] Haile, J. M., and Gupta, S., "Extensions of the molecular dynamics simulation method. II. Isothermal systems", *Journal of Chemical Physics* **79** (1983) 3067-3076.

[45] Nose, S., "A unified formulation of the constant temperature molecular dynamics methods", *Journal of Chemical Physics* **81** (1984) 511-519.

[46] Travis, K. P., and Evans, D. J., "Molecular spin in a fluid undergoing Poiseuille flow", *Physical Review E* **55** (1997) 1566-1572.

[47] Radyzner, Y., and Rapaport, D. C., "Orientational effects in the channel flow of flexible and rigid molecules", *Physical Review E* **57** (1998) 5687-5693.

[48] Verlet, L., "Computer 'Experiments' on Classical Fluids. I. Thermodynamical Properties of Lennard-Jones Molecules", *Physical Review* **159** (1967) 98-103.

[49] Gear, C. W., *Numerical Initial Value Problems in Ordinary Differential Equations* Prentice-Hall, Englewood Cliffs, NJ (1971).

[50] Matubayasi, V., and Nakahara, M., "Reversible molecular dynamics for rigid bodies and hybrid Monte Carlo", *Journal of Chemical Physics* **110** (1999) 3291-3301.

[51] Beeman, D., "Some Multistep Methods for Use in Molecular Dynamics Calculations", *Journal of Computational Physics* **20** (1976) 130-139.

[52] Panton, R. L., *Incompressible Flow* John Wiley & Sons, New York, New York (1984).

VITA

Daniel Maxwell was born in Salt Lake City, Utah on December 6, 1971 to Larry Maxwell and Michelle Wassmer Maxwell. He had a fine education at the hands of the public school system there and continued his education at the University of Utah. His college career was postponed for two years to serve a mission for the Church of Jesus Christ of Latter Day Saints in and around Barcelona, Spain. He returned to school and recieved his Bachelor's Degree (Magna Cum Laude) in Mechanical Engineering in June of 1995. During his college career he was priviledged to be associated with the Upward Bound program where he learned that the human factor should never be lost amidst all the cold equations of engineering.

His interest in space and Heavenly Providence brought him to UTSI near Tullahoma, TN during the summer of 1995. There he found a wonderful academic environment and, in nearby Winchester, the most amazing girl he had ever met. He married Holly Joy Argo on May 25, 1996 in the Atlanta Temple and received his Master of Science Degree in Mechanical Engineering a year later. During the course of his PhD program he established many wonderful relationships, gained a wealth of knowledge, and participated in the birth of his two sons, Hyram and Isaac. He currently plans to practice engineering in the private sector and raise his family.